

ORBIT-DEPENDENT SPECTRAL TRENDS FOR THE NEAR-EARTH ASTEROID
POPULATION

by

Ronald Adrey Fevig

A Dissertation Submitted to the Faculty of the
DEPARTMENT OF PLANETARY SCIENCES

In Partial Fulfillment of the Requirements

For the Degree of

DOCTOR OF PHILOSOPHY

In the Graduate College

THE UNIVERSITY OF ARIZONA

2006

THE UNIVERSITY OF ARIZONA
GRADUATE COLLEGE

As members of the Dissertation Committee, we certify that we have read the dissertation prepared by Ronald Fevig entitled "Orbit-Dependent Spectral Trends for the Near-Earth Asteroid Population" and recommend that it be accepted as fulfilling the dissertation requirement for the Degree of Doctor of Philosophy

Uwe Fink Date: November 16, 2006

Dante Lauretta Date: November 16, 2006

Robert Brown Date: November 16, 2006

Timothy Swindle Date: November 16, 2006

Tom Gehrels Date: November 16, 2006

Final approval and acceptance of this dissertation is contingent upon the candidate's submission of the final copies of the dissertation to the Graduate College.

I hereby certify that I have read this dissertation prepared under my direction and recommend that it be accepted as fulfilling the dissertation requirement.

Dissertation Director: Uwe Fink Date: November 16, 2006

STATEMENT BY AUTHOR

This dissertation has been submitted in partial fulfillment of requirements for an advanced degree at the University of Arizona and is deposited in the University Library to be made available to borrowers under rules of the Library.

Brief quotations from this dissertation are allowable without special permission, provided that accurate acknowledgment of source is made. Requests for permission for extended quotation from or reproduction of this manuscript in whole or in part may be granted by the head of the major department or the Dean of the Graduate College when in his or her judgment the proposed use of the material is in the interests of scholarship. In all other instances, however, permission must be obtained from the author.

SIGNED: _____

Ronald Adrey Fevig

ACKNOWLEDGEMENTS

I thank my advisor, Dr. Uwe Fink, for patiently guiding me through the work associated with this dissertation.

I thank NASA for funding this research through NASA Grants NAG 53937, NAG5-12858 and NASA Training Grant NGT 550243.

I thank Michael Hicks and Jim Scotti for many helpful conversations about near-Earth asteroids.

I thank the faculty and staff of the Department of Planetary Sciences for providing an excellent research environment.

I thank John Downs and Fred Floan for fostering my early educational development.

I thank all of my family and friends who have supported and encouraged my endeavors.

I thank my wife, Beth, for her patience and understanding while I pursued this degree.

I thank my two daughters, Abigail and Nora. Their lessons have taught me volumes about life.

TABLE OF CONTENTS

LIST OF FIGURES	6
LIST OF TABLES	8
ABSTRACT	9
1 INTRODUCTION	11
2 OBSERVATIONS AND DATA REDUCTIONS	18
2.1 Instrumentation	18
2.2 Observations	21
2.3 Data reduction	23
3 SPECTRA AND THEIR CLASSIFICATION	40
3.1 Method of classification	41
3.2 Spectra	50
3.3 The Bus classification method and Principal Component Analysis	56
4 ANALYSIS OF OUR SPECTRAL DATA	59
4.1 The continuum of spectral types between OC-like and S-type NEAs	60
4.2 Size-dependent trends	60
4.3 Orbit-dependent trends	63
4.4 Summary	73
5 OC-LIKE AND S-TYPE NEAS IN BINZEL ET AL. (2004a)	75
5.1 Combining Binzel's and our data into one data set using 40 NEAs observed in common by the two groups	76
5.2 Tabular form of asteroid classification comparison and statistical check	84
5.3 Classifying OC-like and S-type NEAs in Binzel et al. (2004a) using Principal Component Analysis by Bus (1999) of Gaffey (1976) meteorite data	89
5.4 The achondrite ambiguity	95
6 EXTINCT COMETS AMONG THE NEAR-EARTH ASTEROIDS	98
6.1 Trends in orbital inclination for Extinct Comet Candidates in our NEA dataset and Binzel et al.'s (2004a)	99
6.2 Extinct Comets within the NEA population	106
6.3 Conclusion	112
6.4 Summary	117
7 SUMMARY AND FUTURE WORK	119
APPENDIX A: NEA SPECTRA FROM OUR SURVEY	121
APPENDIX B: NOTES ON TAXONOMIC CLASSIFICATION	130
REFERENCES	138

LIST OF FIGURES

2.1	CCD image showing object and sky windows	27
2.2	Spatial profile.....	29
2.3	Processing a CCD image	30
2.4	Preliminary spectrum.....	32
2.5	Ratioed spectra.....	34
2.6	Examples of high SNR spectra	36
2.7	Examples of low SNR spectra	37
3.1	Illustration of our spectral parameters	42
3.2	NEA classification method	45
3.3	Examples of OC-like, S-type and meteorite spectra.....	48
3.4	OC-like and R-type spectra grouped according to spectral parameters.....	52
3.5	S-type and BOC-like spectra grouped according to spectral parameters	53
3.6	Spectra of objects which do not exhibit a 1- μ m absorption.....	54
4.1	Slope vs. size and band depth vs. size for our NEAs.....	62
4.2	Eccentricity vs. semi-major axis for S-type and OC-like NEAs (1).....	64
4.3	Aphelion distance vs. perihelion distance for S-type and OC-like NEAs (1)	65
5.1	Principal Component plot of NEAs observed by both us and Binzel et al. (2004a)	77
5.2	Classification of OC-like and S-type NEAs in Binzel et al.'s (2004a) data	78
5.3	Eccentricity vs. semi-major axis for S-type and OC-like NEAs (2).....	80
5.4	Aphelion distance vs. perihelion distance for S-type and OC-like NEAs (2)	82
5.5	Principal Component plot of Gaffey (1976) meteorite data	90
5.6	Classification of NEAs in Binzel et al. (2004a) using meteorite data	92
5.7	Eccentricity vs. semi-major axis for S-type and OC-like NEAs (3).....	93
5.8	Aphelion distance vs. perihelion distance for S-type and OC-like NEAs (3)	94
5.9	Ordinary chondrites and achondrites separated by Third Principal Component	96
6.1	Inclination distribution for our NEAs that have a 1- μ m absorption	101
6.2	Inclination distribution for our NEAs that do not have a 1- μ m absorption	102
6.3	Classification of Binzel et al. (2004a) NEAs that do not have a 1- μ m absorption...103	
6.4	Inclination distribution for Binzel et al. (2004a) NEAs with $PC2' > 0.15$	104
6.5	Inclination distribution for Binzel et al. (2004a) NEAs with $PC2' < 0.15$	105
6.6	$PC2'$ vs. Slope for Binzel et al.'s (2004a) $T < 3$ NEAs	108
6.7	$PC2'$ vs. Slope for irons and enstatite chondrite meteorites along with Binzel et al.'s (2004a) NEAs	109
6.8	Inclination distribution for comets with periods greater than 200 years	113
6.9	Inclination distribution for comets with periods between 20 and 200 years	114
6.10	Inclination distribution for comets with periods between 10 and 20 years	115
6.11	Inclination distribution for comets with periods less than 10 years.....	116

LIST OF FIGURES - Continued

B.1 Principal Component Analysis of our NEAs	132
--	-----

LIST OF TABLES

2.1 Circumstances for Our Catalina Observatory Observations	24
2.2 Supplemental Classification Information	38
3.1 Physical Parameters for Our Observed NEAs of Table 2.1	51
5.1 Statistical Results from the Binzel et al. (2004a) Data	83
5.2 Comparison of Our Classifications with those of Binzel et al.'s (2004a)	85
5.3 Comparison of NEA Statistics for Our Classifications with those of Binzel et al.'s (2004a)	87
6.1 Estimate of NEA Compositional Abundances from Meteorite Fall and Find Data	111

ABSTRACT

Results of visible to near-infrared spectrophotometric observations of 55 near-Earth asteroids (NEAs) are reported. The observing techniques, instrumentation, and method of data analysis are described. A new asteroid classification method that directly compares these NEA spectra with spectral features of meteorites is presented. Two major siliceous groups (having discernible “1- μm ” absorptions) result from this method, OC-likes which match the spectra of ordinary chondrites and S-types. The dataset shows a preponderance of spectra consistent with ordinary chondrites (23 NEAs), as well as S-types (19), 2 with spectra consistent with black ordinary chondrites, 2 R-types, and 9 that show no 1- μm absorption.

The spectral characteristics of the siliceous S-type and OC-like asteroids blend together, providing evidence that S-type asteroids are simply ordinary chondrites whose surface has been modified by weathering. This helps resolve the long standing question of the lack of main belt asteroids having spectra matching ordinary chondrite meteorites. Main belt asteroids have on average much older surfaces while NEAs that exhibit OC-like spectra have younger surfaces.

It was found that fresh objects having spectra consistent with ordinary chondrites (1) occupy mostly highly eccentric Apollo orbits which encounter a strong collisional environment in the asteroid main-belt, (2) may have been recently injected into high eccentricity orbits, or (3) have suffered tidal disruption. S-type NEAs reside primarily in

orbits that do not cross the asteroid main-belt. This orbit dependent trend is verified by using the larger NEA dataset of Binzel et al. (2004a).

Nine NEAs from this survey exhibiting no 1- μm absorption can be associated with extinct comets, iron meteorites or enstatite meteorites. It is shown that most of these NEAs must be extinct comets, implying a considerably larger fraction of comets among the NEA population than previously thought. A correlation of these objects with low inclination orbits is found.

This study finds that the NEA population is divided roughly as follows: ~40% fresh ordinary chondrites, ~35% S-types, ~20% extinct comet candidates, and ~5% in minor classes. This work may guide NEA mitigation planning should such an emergency arise.

CHAPTER 1

INTRODUCTION

Near-Earth Asteroids (NEAs) are asteroids whose perihelia are less than 1.3 AU. They are divided into three groups according to the relation of their orbital parameters to Earth's semimajor axis (1 AU), aphelion (1.017 AU) and perihelion (0.983 AU). Amors have perihelia between 1.017 and 1.3 AU. Apollos have semimajor axes greater than 1 AU and perihelia less than 1.017 AU. Atens have semimajor axes less than 1 AU and aphelia greater than 0.983 AU. Apollos and Atens are sometimes called Earth-Crossing Asteroids, even though the orbits of the Earth and these types of NEAs don't usually intersect. In 1898, Gustav Witt discovered the first NEA, the Amor-class asteroid (433) Eros. Some time passed before the first Earth-Crossing (Apollo-class) asteroid was discovered by Karl Reinmuth, (1862) Apollo in 1932. Not only did this object cross Earth's orbit, but it crossed the orbit of Venus, also. The next major discovery occurred in 1976 when Eleanor Helin found an asteroid whose orbital period is shorter than Earth's, the Aten-class asteroid (2062) Aten. Her team also discovered the first NEA to be positively linked to a comet that had subsequently become dormant, (4015) Wilson-Harrington (see Chapter 6 for a discussion of these objects). All of these initial discoveries were made using photographic plates that were inspected for moving objects by eye. The NEA discovery rate increased dramatically with the introduction of Charge Coupled Device (CCD) detectors, in place of photographic plates, and computerized detection techniques, in place of detection by human eyes. Spacewatch, lead by Tom

Gehrels and Robert McMillan, was the first asteroid detection group to employ such instrumentation in the early 1980's and all contemporary NEA search programs are based on this approach. As of 2006 September 26, a total of 4170 NEAs had been discovered. These NEA discoveries are distributed as follows: 1789 Amors, 2039 Apollos, and 342 Atens.

NEA physical studies began shortly after the discovery of (433) Eros and focused on determinations of its size and pole orientation (Watson, 1937). In order to address questions of composition, though, spectra of asteroids were required. The first attempts to acquire spectrophotometric data involved filter photometry. During the 1970's and early 1980's, a large number of main-belt asteroids were observed with an eight color filter set which spanned the wavelength range from ~ 3000 to ~ 11000 Å. Tholen (1984) classified these objects according to their spectrophotometric measurements, devising a purely descriptive taxonomy of 14 classes based on roughly 12 commonly observed spectral shapes and asteroid albedo information. It served as the basis for contemporary, more complex asteroid classification methods. It was done without any attempt to correlate these various "classes" with physical properties of the asteroids. In addition to the large number of main-belt asteroids classified, 17 NEAs were classified as a result of this survey. Since NEAs are intrinsically dim and difficult to observe, filter photometry continues to be an important method for acquiring initial spectrophotometric measurements for NEAs (McFadden et al., 1989; Rabinowitz, 1998; Whiteley, 2001; Dandy et al., 2003).

CCD detectors have not only brought about a revolution in the discovery of asteroids, as noted above, but also in characterizing their composition through their use in spectrographs. By coupling high quantum-efficiency CCD detectors with long-slit spectrographs, spectral images of faint NEAs can be acquired relatively quickly and the subsequent calibration of those images can be accomplished in an efficient manner. The first spectroscopic CCD observation of an astronomical object, Pluto, was carried out by Fink et al. (1980) using a specially built long slit spectrograph matched to available CCDs. This instrument was later used to take the first CCD spectra of asteroids (Vilas and Smith, 1985). The techniques developed for CCD spectroscopic reductions on this instrument have laid the groundwork for techniques developed for other such instruments. A goal for these spectroscopic surveys has been to identify asteroid parent bodies for the different classes of meteorites in terrestrial samples.

A long-standing problem in meteoritics and asteroid research had been the origin of the ordinary chondrite (OC) class of meteorites. Approximately 80% of all meteorite falls are ordinary chondrites so researchers expected to find an abundance of asteroids that exhibit the spectral signature of this type of meteorite. Until CCD observations of NEAs as described below were carried out this was not the case. While there are no main-belt asteroids known to have the spectral signature of ordinary chondrites among the numerous observations reported in Tholen (1984), the single object ((1862) Apollo) that received a Tholen Q-type classification was later linked (McFadden et al., 1985) to the ordinary chondrite class of meteorites.

Many arguments have been put forth to explain the lack of objects with ordinary chondrite-like (OC-like) spectra in the asteroid main-belt (Bell et al., 1989; Gaffey et al., 1989). There is now a general consensus that there are actually a large number of asteroids of ordinary chondrite composition but their surfaces have been spectrally modified to mask the spectral signature of ordinary chondrites -- the "space-weathering" hypothesis (Hapke, 2001; Clark et al., 2002; and Chapman, 2004). The analysis of NEA spectra in Chapters 3 and 4 of this dissertation strongly corroborates the space weathering hypothesis and shows that among the NEA population there essentially is a continuum ranging from excellent matches to ordinary chondrites to completely weathered asteroids.

Presumably, asteroids and comets are the primary source for meteorites. Since NEAs and meteoroids must both cross the orbit of the Earth, one would expect them to be closely related in composition, either due to meteoroids spawning off NEAs or because the two would likely follow similar orbital evolutionary paths from source regions in the asteroid main-belt to the inner solar system. The number of NEA spectra available increased substantially in the 1990's (Hicks, Grundy, Fink, Mottola and Neukum, 1995; Binzel et al., 1996a,b, Fink, Hicks, Collins and Grundy, 1996; Hicks, Fink and Grundy, 1998). The NEA spectral survey described in this dissertation began in 1994 with spectroscopic observations of the NEA (1620) Geographos (Hicks, Grundy, Fink, Mottola and Neukum, 1995). These observations were taken in support of the Clementine mission to Geographos which unfortunately was not successful. From 1994 to 1996 this work expanded to 14 NEAs (Fink, Hicks, Collins and Grundy, 1996; Hicks, Fink and Grundy, 1998) of which the majority showed an unusually deep absorption

longward of $\sim 7500 \text{ \AA}$ (henceforth referred to as the “1.0- μm absorption”) matching the spectra of ordinary chondrites. A similar conclusion was reached by Binzel et al. (1996a,b) who identified six near-Earth asteroids (out of a total of 50) as having spectral properties consistent with ordinary chondrites.

The most prolific spectroscopic survey of asteroids has been the Small Main-Belt Asteroid Spectroscopic Survey (SMASS) lead by Richard Binzel (Xu et al., 1995; Bus and Binzel, 2002a,b). Since 1991 this team has acquired spectra of a large number of NEAs in addition to over 1300 main-belt asteroids. The results pertaining to NEAs have been published in Binzel et al. (1996a, 2001a,b, and 2004a,b,c). Their most recent NEA paper (Binzel et al., 2004a) is a compendium of their previously reported and recent NEA observations, numbering 310 objects, and provides a wealth of spectral information about this population of asteroids.

The spectroscopic survey described in this dissertation resulted from a NEA spectroscopic observing program (Hicks, Fink and Grundy, 1998; Fevig and Fink, 2006) that was combined with a long-term spectroscopic survey program of comets (Fink and DiSanti, 1990; Fink and Hicks, 1996; Fink, Hicks, Fevig and Collins, 1998; Fink, Hicks and Fevig, 1999). Approximately half of the time at the telescope was devoted to each program. In order to study the problem of the origin of ordinary chondrite meteorites and characterize the distribution of spectral types among the NEAs, a total of 55 NEA spectra were acquired. Fourteen were presented in Hicks, Fink and Grundy (1998). The 41 additional NEA spectra were accepted for publication in *Icarus* (Fevig and Fink, 2006). Preliminary results were also presented at the 33rd and 35th Division for Planetary

Sciences meetings (Fevig and Fink, 2001; Fevig and Fink, 2003). This expanded survey was initiated in order to:

1. Confirm the earlier result that there is a preponderance of NEAs with the spectral signature of ordinary chondrites.
2. Corroborate Binzel et al.'s (1996a) and Hicks, Fink and Grundy's (1998) earlier results that there is a continuum of NEA spectral types between the S-types and those with spectra consistent with ordinary chondrites.
3. Acquire a sufficiently large random sample of NEA spectra to allow statistically significant correlations with orbital parameters and size.

This dissertation is organized as follows. Chapter 2 describes acquisition of the data beginning with observations at the telescope, the instrumentation used including the CCD spectrograph and guider box, and the data reduction techniques used to go from raw CCD spectral images to processed NEA spectra. Chapter 3 presents the resulting spectra and the method of classifying these spectra. This classification method does not employ the commonly used Principle Component Analysis (Tholen, 1984; Bus, 1999), which may at times obscure the compositional interpretation of asteroids, but instead classifies NEAs of siliceous composition in a manner that facilitates their correlation with meteorites. Chapter 4 presents the analysis of the spectral data and the subsequent conclusions. In addition to finding a large number of NEAs that have spectra consistent with ordinary chondrite meteorites, an orbital trend among these type of NEAs and S-type NEAs is reported. In Chapter 5 these same orbital trends are found to persist in the larger NEA spectral dataset of Binzel et al. (2004a). A significant prerequisite to that

analysis involved classifying this larger dataset in a manner consistent with the classification method described in Chapter 3. In Chapter 6 this larger dataset is used to investigate an additional orbital trend which points to a cometary origin for certain types of NEAs. This trend was noted in the combined spectral data of Hicks, Fink and Grundy (1998) and Fevig and Fink (2006), but it was necessary to utilize the Binzel et al. (2004a) data set to confirm this observation.

CHAPTER 2

OBSERVATIONS AND DATA REDUCTIONS

This chapter describes the instrumentation and observing techniques used to acquire spectra of NEAs and the method of data analysis employed to reduce these spectra. A description of the telescope, spectrograph, guider box and camera used to acquire spectral data is contained in Section 2.1. The method of observing asteroids and calibration stars at the telescope with this instrumentation is outlined in Section 2.2. The process of producing relative reflectance spectra from raw spectral images is described in detail in Section 2.3.

2.1 - Instrumentation

NEA observations were done at the University of Arizona Observatory Catalina Site 61-inch telescope located near Tucson. Since observing time on this medium-sized telescope is reasonably available, and it tracks well on fast-moving objects, it is well-suited for a spectroscopic survey of NEAs. Furthermore, observing conditions at this site are good, with typical seeing of 1"-2". This Cassegrain telescope was used in its f/13.5 configuration, which gives a nominal plate scale of 10"/mm.

All NEA spectra were acquired with the high efficiency LPL CCD Spectrograph which was specifically designed for this telescope in its f/13.5 configuration. This spectrograph was the first to use a Charge Coupled Device (CCD) for its detector and made initial observations of methane in Pluto's atmosphere (Fink et al., 1980; Buie,

1984). This spectrograph utilizes a transmission grating and, in order to attain a high efficiency, a minimal number of optical components. Its end-to-end efficiency (telescope + dichroic beamsplitter + spectrograph + CCD camera) is approximately 15%, very high compared to most spectroscopic astronomical systems. Its limiting magnitude at the 61-inch telescope for point sources is $V_{\text{mag}} \approx 18$ for a signal to noise ratio of approximately 20 and integration times on the order of several hours. (For an example see Figure 2.7.)

The focal plane of the telescope coincides with the surface of the slit of the spectrograph. The light beam passes through the slit whose length is 18 mm long. The slit width can be varied between 0 and 2 mm. Given the dimensions of its slit and the plate scale of the telescope, the field of view of the spectrograph is 180" by up to 20", depending on the chosen slit width. A shutter located behind the slit is used to control the length of an exposure. The light beam then passes through a Schott RG 530 cut-off filter which passes light longward of 5300 Å. It is used to eliminate overlapping orders in the spectral image. This yields an effective wavelength range for this instrument of approximately 5300 Å to 10,000 Å. After the cut-off filter the beam passes through a collimating lens. The collimated beam is then dispersed by a 300 line/mm grating, and then imaged on to the CCD using an f/1.4 lens. A microscope is mounted on the side of the spectrograph. Using a flip-mirror inside the spectrograph the observer can either position the mirror in the light beam to view an image of the slit with this microscope, allowing one to see if the target is centered, or rotate the mirror out of the beam, allowing the light to pass through the spectrograph.

A guider box mounts between the telescope and spectrograph. This interface contains the hardware necessary for precisely guiding on fast-moving NEAs. There are three mounting points on the guider box. On opposite sides, perpendicular to the axis of the telescope, are the mounting points for the guiding/imaging CCD camera and an eyepiece for visual observations. Along the axis of the telescope at the bottom of the guider box is the mounting point for the spectrograph. Three carriages are contained within the guider box. Two of these contain bending mirrors, one for direct imaging of objects and the other for visual observations. The third carriage has a dichroic beamsplitter which sends the blue part of the image to the guiding camera while passing the visible and red light above $\sim 5000 \text{ \AA}$ to the spectrograph. This carriage is normally configured so that the incoming beam encounters the dichroic beamsplitter, allowing one to simultaneously guide on the blue light and acquire spectra at wavelengths longward of 5000 \AA . Occasionally objects are imaged directly using the guiding camera, in which case one of the bending mirrors is in the beam. The other bending mirror for visual observations through an eyepiece is rarely used. A shutter is in front of the guiding camera and the associated control electronics are mounted on the side of the guider box. There is also a filter slide in front of the guiding camera so that in direct imaging mode filter photometry of objects can be done.

High quantum efficiency CCD cameras are used for both imaging spectra and guiding on targets. An 800 by 800 pixel Texas Instrument CCD chip with 15 \mu m pixels was used for nearly all of the data collection. The spectral image scale in the spatial dimension, perpendicular to the spectrum, is $1.5''/\text{pixel}$ for this camera. Along the

spectral dimension the average dispersion is $7.21 \text{ \AA}/\text{pixel}$. The spectral images do not fill the entire area of the CCD detector. Given the spatial and spectral scale of the image it sufficed to read out an 800 by 180 pixel sub-array of the CCD detector that contained the object's signal and the night sky.

It should be noted that a retrofit of the LPL CCD spectrograph was completed in 2004 in which a new high-efficiency holographic grating was added and the optics were re-aligned. Also, a 2048 by 2048 CCD camera was used for spectral imaging. Only the observations of 2004 LC₂ were taken with this configuration.

2.2 - Observations

Observations of comets and asteroids were combined at the telescope, with approximately half of the time devoted to observing each type of object. All targetable NEAs were observed during these observing runs. Target selection was accomplished with the help of David Tholen's observing software, SEARCH. This program computes the observing circumstances (i.e., Right Ascension, Declination, apparent magnitude, solar elongation) for NEA targets on a given night. Ephemerides were generated for each target and an observing plan for each observing run was made. To maximize the quality of the data an attempt was made to observe targets as they transited the meridian to minimize the airmass for each observation.

At the beginning of each observing night the telescope was pointed at and focused precisely on a bright star. The guiding system was then calibrated by visually centering this star in the spectrograph's slit while taking several images with the guiding camera.

The centroid of this star in each of these images was then determined, an average taken, and the mean value of the sub-pixel location recorded in the guiding software parameter file as the guidepoint. This guidepoint was then used by the guiding software throughout the night to maintain each target object's positioning to within 0.5"-1" of the center of the slit.

Since the typical seeing at the Catalina site is 1"-2" and the guiding accuracy is about 1", a slit width of 5" was used for NEAs. This gave a comfortable margin so that essentially all the light from the object was gathered yet night sky emissions with their concomitant noise were minimized. The spectral resolution for this slit width is about 15Å. Spectral resolution is not critical for asteroids since they tend to exhibit only broad spectral features. In order to attain a sufficiently high signal level for the object relative to the bias and sky levels, integration times were typically 10 to 20 minutes. A number of spectral images were taken for each object and their spectra added to increase the Signal to Noise Ratio (SNR) in the final spectrum.

Spectra of solar analog stars (i.e., stars whose colors closely match the Sun) were acquired at similar airmasses and, if possible, through the same part of the sky as the target asteroids. Spectra of standard stars for absolute calibration were also acquired. The solar analog stars were selected from the 13-color photometry of solar-type stars (Schuster, 1976) and are vital to the spectral reduction process. These solar analog stars are relatively bright ($5 < V_{\text{mag}} < 7$) so that short integration times on the order of seconds suffice. Usually between five to ten exposures of the solar analogs were taken to allow

discarding of spurious exposures and to accumulate sufficient counts so that the solar analog did not contribute any noise to the final ratios.

Table 2.1 summarizes the observations for the 41 NEAs observed since 1997. The table is sorted according to the order in which these objects were first observed. (Refer to Hicks, Fink and Grundy (1998) for the observational circumstances of the 14 NEAs observed before 1997.) Most objects were observed on multiple nights to verify the consistency of the data. The visual magnitude (V_{mag}), phase angle, solar elongation (s.e.), heliocentric distance (r), and geocentric distance (Δ) at the time of observation are shown. These quantities were computed by using orbital elements from the ASTORB database (<ftp://ftp.lowell.edu/pub/elgb/astorb.html>). The spectra for each night were summed and analyzed. The total integration time for each night is shown in the table. The last column in the table indicates the solar analog stars used for each object.

2.3 - Data reduction

Each CCD spectral image is a sub-array of 180 pixels along the spatial axis by 800 pixels along the spectral direction of the 800 by 800 pixel Texas Instrument, Inc. CCD chip. (For the observations on 2004 June 15 a 2048 by 2048 pixel CCD chip was used from which a 201 pixel by 2048 pixel sub-array for each spectral image was read out.) The data were reduced using UNIX and NAWK scripts and spectroscopic reduction software. This spectroscopic software package was called ARGOS.

The steps in the data reduction process are: 1. Remove column defects. 2. Determine the centerline of the object's signal. 3. Interpolate cosmic ray strikes. 4.

Table 2.1 - Circumstances for Our Catalina Observatory Observations

Object	Date of Observation (UT)	Vmag ^a	Phase Angle ^a	s.e. ^a	r ^a	Δ^a	Integration Time (min.)	Solar Analog Star(s)
(3103) Eger	1997 Jan 28	15.3	-16.1	156.4	1.420	0.461	60	BS695,BS4030
	1997 Feb 3	15.3	-10.8	163.9	1.450	0.477	80	BS2141,BS660
(1627) Ivar	1997 Feb 2	16.5	3.3	171.4	2.588	1.609	80	BS3626,BS2067
	1997 Feb 3	16.5	3.8	170.0	2.587	1.611	50	BS2141,BS660
(13651) 1997 BR	1997 Feb 2	17.2	-15.0	158.8	1.381	0.415	60	BS3626
	1997 Feb 4	17.2	-15.4	158.3	1.372	0.406	80	BS2141,BS4027
	1997 Feb 5	17.2	-15.7	157.9	1.367	0.402	80	BS2141
(3199) Nefertiti	1997 Feb 2	15.9	-22.0	143.9	1.551	0.642	80	BS3626
	1997 Feb 5	15.8	-19.8	147.6	1.563	0.638	80	BS2141,SAO100038
(3122) Florence	1997 Feb 3	16.3	-9.0	161.8	1.960	0.999	80	BS2141,BS660
	1997 Feb 4	16.3	-9.0	161.8	1.965	1.004	80	BS2141
(7482) 1994 PC1	1997 Feb 5	16.6	100.9	68.8	0.936	0.179	30	Did not reduce
	1997 Jun 3	17.8	-51.4	105.1	1.254	0.519	100	BS6458
	1997 Jun 4	17.7	-50.7	106.2	1.259	0.514	135	BS6458,BS5534
(35107) 1991 VH	1997 Mar 2	15.9	-18.2	155.9	1.300	0.330	70	BS2141
	1997 Mar 5	15.9	-18.7	155.1	1.300	0.331	90	BS2141,BS4277
(7822) 1991 CS	1997 Mar 2	15.8	-27.5	146.4	1.190	0.230	60	BS2141
	1997 Mar 4	15.9	-28.8	144.5	1.195	0.239	40	BS4277
	1997 Mar 5	16.0	-29.7	143.3	1.197	0.244	40	BS2141
(4954) Eric	1997 Mar 3	15.5	-11.6	153.9	2.179	1.245	80	BS2141,BS660
	1997 Mar 6	15.4	-9.8	157.9	2.194	1.242	80	BS2251,BS4027
(11066) Sigurd	1997 Mar 6	16.6	-5.4	170.0	1.843	0.858	80	BS2251,BS4027
(1685) Toro	1997 Mar 6	15.9	-23.2	138.6	1.664	0.785	40	BS1262,BS4328
	1997 Apr 2	15.7	11.8	158.8	1.774	0.805	60	BS2141,BS5183
(5587) 1990 SB	1997 Mar 7	17.0	10.9	153.0	2.395	1.468	100	BS3750,BS4027
(1036) Ganymed	1997 Mar 29	14.8	-4.3	163.8	3.701	2.732	80	BS4027,BS2141
	1998 May 1	12.4	-36.1	94.3	1.704	1.300	35	BS5183,BS5968
	1998 Jun 17	11.4	-45.5	96.0	1.417	0.887	26	BS7914
	1998 Jun 18	11.4	-45.7	95.9	1.412	0.882	18	BS7914
	1998 Jun 29	11.2	-48.3	94.3	1.357	0.826	15	BS7914
(3671) Dionysus	1997 Mar 29	17.4	-22.9	142.6	1.558	0.642	80	BS4027,BS2141
	1997 Apr 2	17.2	-22.8	143.8	1.528	0.603	40	BS5183,5968
	1997 Apr 29	16.2	29.6	139.4	1.329	0.391	60	BS5183
	1997 May 2	16.1	31.3	137.6	1.307	0.372	80	BS5968,BS7272
1997 GD32	1997 Apr 29	17.0	-54.2	123.4	1.037	0.052	40	BS3625,BS5183
	1997 May 1	17.2	-71.3	106.2	1.022	0.046	100	BS5968,BS6060
	1997 May 3	17.9	-90.7	86.7	1.007	0.046	120	BS5968,BS4486
(19356) 1997 GH3	1997 May 1	16.8	44.1	122.7	1.220	0.332	80	BS4529,BS5968,BS6060
	1997 May 3	16.9	43.2	123.3	1.231	0.344	120	BS5968,BS4486
(4341) Poseidon	1997 May 2	15.6	-41.0	124.0	1.274	0.398	60	BS5968,BS7272
	1997 May 31	16.2	14.0	157.9	1.577	0.591	70	BS5659,BS5868
	1997 Jun 1	16.2	14.0	157.8	1.587	0.601	40	BS5727,BS6441
	1997 Jun 2	16.3	14.0	157.6	1.597	0.612	67	BS5727,BS6441

^a Visual magnitude at the time of observation, phase angle, solar elongation, heliocentric distance and geocentric distance computed using orbital elements from Lowell Observatory's 'ASTORB' database and David Tholen's 'ephem' program.

Table 2.1 - Circumstances for Our Catalina Observatory Observations (Continued)

Object	Date of Observation (UT)	Vmag ^a	Phase Angle ^a	s.e. ^a	r ^a	Δ^a	Integration Time (min.)	Solar Analog Star(s)
(1943) Anteros	1997 May 31	16.3	-62.6	96.3	1.136	0.412	40	BS5659,BS5868
	1997 Jun 1	16.3	-62.2	96.7	1.138	0.412	80	BS5727,BS6441
	1997 Jun 2	16.3	-61.9	97.1	1.141	0.413	70	BS5727,BS6441
(7753) 1988 XB	1997 Jun 3	16.6	7.1	171.1	1.258	0.246	80	BS6458,BS5183
(85490) 1997 SE5	1997 Oct 30	15.7	41.3	118.4	1.324	0.522	60	BS2067
(4183) Cuno	1997 Oct 30	16.9	5.7	167.6	2.145	1.165	60	BS660,BS9107
	1997 Oct 31	16.8	5.8	167.4	2.138	1.158	80	BS1262
	1997 Nov 30	17.1	22.1	133.2	1.910	1.094	80	BS695
1997 US9	1998 Jun 29	14.1	43.4	123.7	1.231	0.331	70	BS5868
	1997 Nov 1	16.4	11.0	165.0	1.346	0.362	100	BS1262,BS3626
	1997 Nov 3	16.6	13.8	161.2	1.345	0.367	80	BS2007,BS2141
1997 UH9	1997 Nov 1	16.8	-10.1	167.5	1.223	0.235	60	BS1262,BS3626
	1997 Nov 3	16.6	-5.4	173.4	1.224	0.233	80	BS2007,BS2141
	1997 Nov 4	16.4	-3.1	176.1	1.224	0.233	100	BS1262,BS2251
(1980) Tezcatlipoca	1997 Nov 4	13.6	54.6	111.1	1.135	0.299	65	BS1262,BS2251
	1997 Nov 30	13.3	34.5	135.1	1.228	0.313	70	BS660
(10563) Izhdubar	1997 Nov 28	16.4	47.2	120.2	1.163	0.295	88	BS1747,BS1262
	1997 Nov 29	16.4	48.3	118.6	1.160	0.300	108	BS1532,BS2141
(5751) Zao	1997 Nov 28	16.1	-18.7	147.8	1.640	0.719	134	BS1747,BS1262
	1997 Nov 29	16.1	-18.8	147.7	1.635	0.714	120	BS1532,BS2141
(7977) 1977 QQ5	1997 Nov 29	16.7	-40.5	115.0	1.378	0.632	60	BS1532,BS483
	1997 Nov 30	16.7	-39.9	115.8	1.383	0.631	60	BS695
(5836) 1993 MF	1997 Dec 1	16.2	1.5	176.6	2.183	1.197	172	BS2067
(20236) 1998 BZ7	1998 Jan 31	16.5	-15.3	159.9	1.284	0.313	220	BS2007,BS3625
(433) Eros	1998 Jan 31	12.0	-56.3	91.4	1.185	0.634	54	BS1262
(6037) 1988 EG	1998 Mar 23	16.8	25.5	149.3	1.182	0.210	80	BS4277,BS3625
	1998 Mar 24	17.0	25.8	148.7	1.190	0.219	160	BS5868
	1998 Mar 25	17.1	26.2	148.0	1.198	0.229	140	BS4027,BS5534
(1862) Apollo	1998 Mar 23	17.1	-9.8	163.7	1.643	0.662	20	BS4277,BS3625
	1998 Mar 24	17.1	-9.1	165.0	1.636	0.652	140	BS7914,BS5868
	1998 Mar 25	17.0	-8.4	166.3	1.629	0.643	134	BS4027,BS3625
1998 HE3	1998 May 1	17.2	11.1	168.0	1.089	0.084	140	BS5183,BS5968
	1998 May 2	17.2	13.4	165.5	1.084	0.078	114	BS6538,BS5911
(20255) 1998 FX2	1998 May 2	16.3	-42.8	130.6	1.126	0.170	100	BS6538,BS5911
	1998 May 4	16.4	-42.7	130.5	1.131	0.177	80	BS5868,BS5968
1998 HT31	1998 May 4	15.8	-23.2	155.6	1.058	0.054	158	BS5868
(8201) 1994 AH2	1998 Jun 17	15.5	79.3	90.2	1.034	0.188	90	BS8041
	1998 Jun 18	15.4	76.3	93.3	1.044	0.189	77	BS5968,BS7914
	1998 Jun 19	15.4	73.2	96.4	1.055	0.191	50	BS7914,BS6538
(1866) Sisyphus	1998 Jun 18	15.0	27.5	129.6	1.694	0.855	50	BS5968
	1998 Jun 19	15.1	28.3	128.2	1.687	0.858	60	BS9107
(7358) 1995 YA3	1998 Jun 18	14.6	0.7	178.9	1.661	0.645	65	BS5868
	1998 Jun 19	14.7	1.5	177.6	1.654	0.638	70	BS9107,BS483
1998 MS2	1998 Jun 27	17.2	18.8	159.0	1.136	0.127	180	BS6847
	1998 Jun 28	17.3	20.4	157.0	1.140	0.133	80	BS5868,BS6060
1998 ME3	1998 Jun 29	16.9	32.4	142.7	1.148	0.160	150	BS8314
2004 LC2	2004 Jun 15	16.0	-55.7	119.6	1.069	0.100	65	SAO160671,BS6060

^a Visual magnitude at the time of observation, phase angle, solar elongation, heliocentric distance and geocentric distance computed using orbital elements from Lowell Observatory's 'ASTORB' database and David Tholen's 'ephem' program.

Construct preliminary spectra by summing the asteroid's counts within a 16.5" object window perpendicular to the spectrum and subtracting night sky emissions by two symmetrically placed windows on either side of the spectral window. This removes any linear sky gradient. 5. Register all spectra in wavelength by shifting them using the telluric O₂A absorption feature as a fiduciary marker. 6. Create summed spectra for each NEA and solar analog star. 7. Ratio NEA spectra by solar analog star spectra that are matched in airmass. 8. Wavelength calibrate spectra using a quadratic equation fitted to spectral lines from emission lamps. 9. Normalize spectra to unity at 7010 Å. 10. Bin spectra in the wavelength domain to increase the SNR. While some of the steps in this process can be performed in an automated fashion with little input from the user others are quite time consuming and require substantial user effort. The details of these reduction steps are elaborated on in the subsequent paragraphs of this section.

Figure 2.1 shows a typical raw CCD spectral image. This figure shows the 180 by 800 pixel sub-array that is read out from the 800 by 800 pixel CCD detector. The spectrum is dispersed along the horizontal axis (columns). Wavelength increases with increasing column values. In this figure the strong spectral signal from a star is evident as a horizontal line in the image. The spatial dimension, along the slit, corresponds to the vertical axis (rows) in this image. Depicted in this figure are typical object and sky windows for which the column-by-column spectrophotometry is performed.

As the first step in the reduction process, column defects are removed. These defects are at known locations on the chip and are removed by interpolation. A spatial profile along columns shows the row locations of the object's spectral centerline and, if

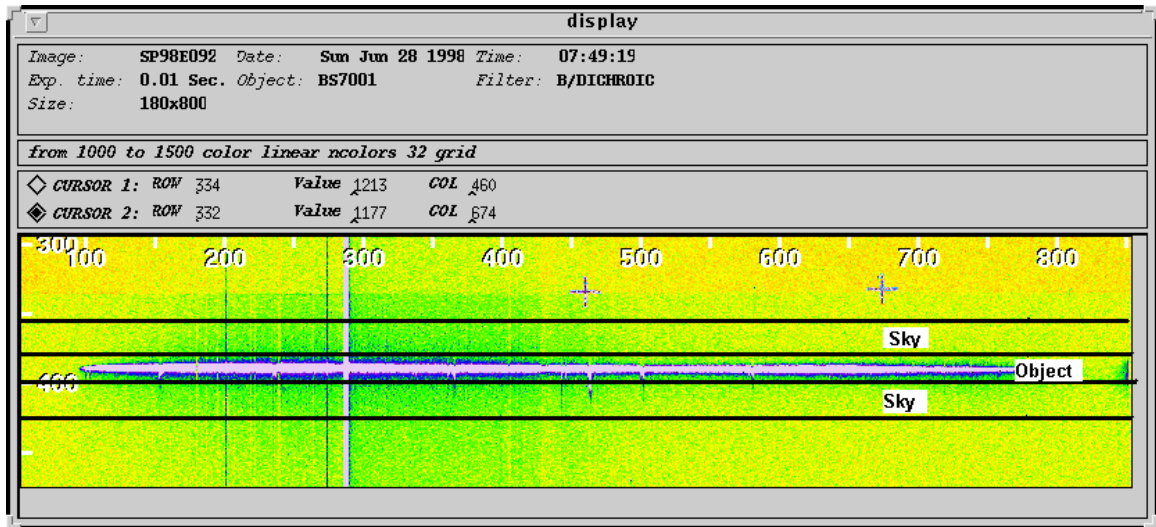


Figure 2.1. Diagram of a raw CCD image showing the object's signal, the object window, and the two adjacent sky windows. Since this is a short 0.01 second exposure of a standard star, no sky signal is accumulated.

present, field stars in the image. From the output of the routine that produces the spatial profile, another program determines the object's spectral centerline along with the row locations of suspected field stars. The original spectral images are inspected to verify the choice of centerline for each image and the presence of field stars. This information is used in subsequent reduction steps. A spatial profile for a spectral image of an NEA is shown in Figure 2.2. The peaks in this image correspond to the signal from this object and two field stars as indicated. Also shown are the object and sky windows.

After the centerline and the object window have been determined, cosmic ray patching may proceed. For each pixel in a given image, the ARGOS cosmic ray patching routine computes the mean of the adjacent pixels. It takes as one of its arguments a threshold factor above the ambient sky, thus identifying the cosmic ray strikes. By executing this routine iteratively with decreasing threshold factors cosmic rays are essentially eliminated. The automatic patch mode is used outside of the object window. Since special care must be taken within the object window to avoid patching real features, a manual patch mode is used in this region. This process of manually patching the object window is the most time-consuming step in the spectral reduction process, taking up to 15 minutes per image.

Figure 2.3 illustrates the effect of the first three steps of this reduction process on a spectral image of an asteroid, (1036) Ganymed. In the raw spectral image (top of figure), an asteroid's spectral signal and night sky emissions can be seen along with column defects and numerous cosmic ray strikes. In the second image from the top, column defects have been removed. In the second image from the bottom, cosmic rays

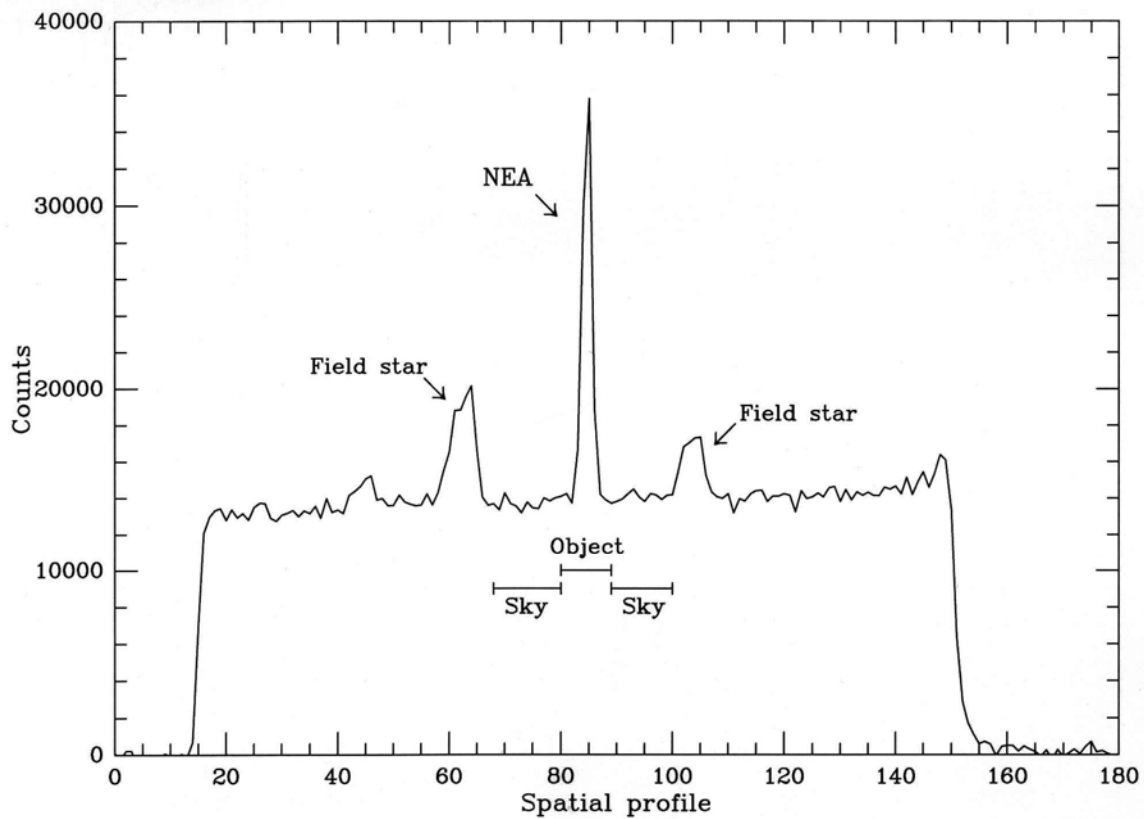


Figure 2.2. Spatial profile from a spectral image of an NEA. Shown here are the locations of the signal from the NEA and two field stars and the positions of the object and sky windows. The sky windows are chosen to avoid field stars.

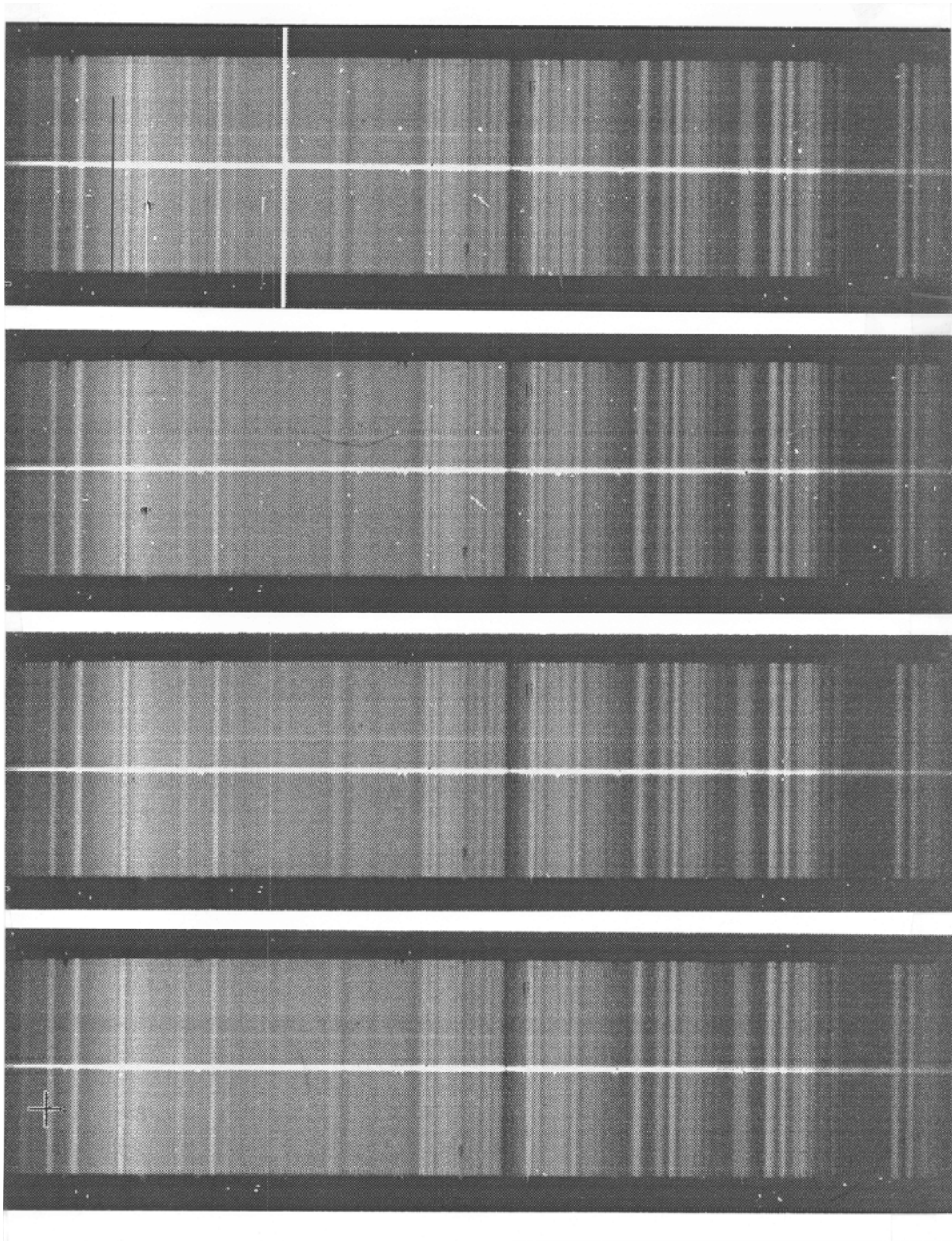


Figure 2.3. Evolution of a spectral image from the initial raw image (top) through column defect and iterative cosmic ray removal. The frame illustrated is a 20 minute exposure of the NEA (1036) Ganymed. Note the complexity of the night sky spectrum (lines extending along the whole slit length).

have been automatically removed outside of the object window with software. And finally, at the bottom, cosmic rays have been manually removed within the object window.

After the removal of image defects by the above processes, preliminary spectra are produced. The ARGOS 'spec' command takes as arguments the range of rows corresponding to the object and sky windows in a given image and calculates a fit to the sky regions. The row locations of field stars are noted and excluded from the sky window. The resultant fit to the sky is then subtracted column-by-column from the values in the object window, resulting in a file of object intensity (DN values) versus column number. Figure 2.4 shows a preliminary spectrum for a solar analog star. The overall curvature of this raw spectrum is partially representative of the response of the system. The prominent atmospheric O₂A absorption feature can be seen in the middle of this spectrum. For confirmation and consistency checks, two synthetic apertures are generally used for generating asteroid spectra; one with an object window 11 rows wide and another 21 rows wide.

Due to flexure of the telescope/instrument assembly at varying pointing angles throughout a night, the spectral features may shift between sets of images by a couple columns. A series of scripts allowed the user to locate the O₂A absorption feature in each spectrum and shift the spectra to a common wavelength position. The final spectrum for each object from that night was then produced by summing the individual spectra for that object.

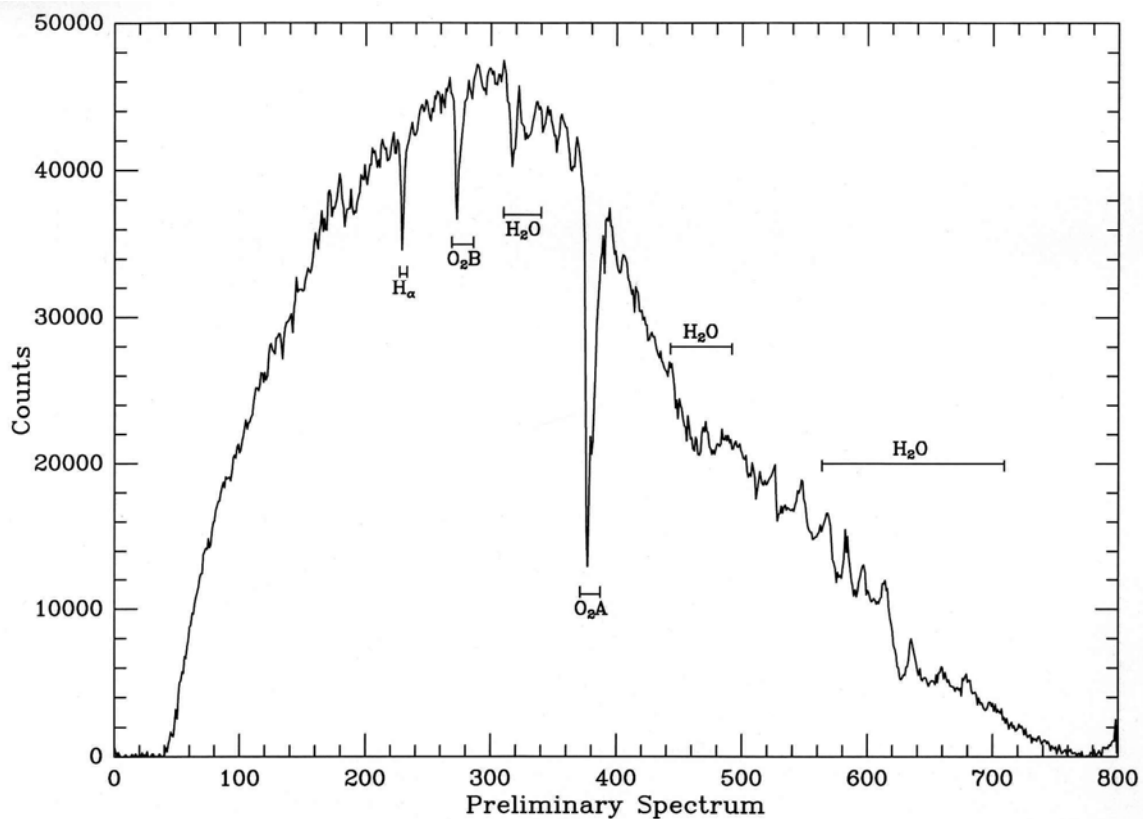


Figure 2.4. Preliminary spectrum of a solar analog star. Positions of telluric absorption bands and the solar H_{α} line are shown. The strong atmospheric O_2A absorption feature is used as a fiducial marker.

Once the final spectra have been produced, a consistency check of the individual spectra is performed. Each individual spectrum of an object is divided by its corresponding final (summed) spectrum. An example is shown in Figure 2.5. In this figure one can see that apart from regions of high noise at either end of the spectrum, the superimposed ratioed spectra for this object agree very well. Should any of the resultant ratios contain sharp spikes, indicative of residual cosmic ray strikes, or exhibit a strong slope, indicative of an object being too near the edge of the slit, the offending spectrum is either fixed or discarded from the sum used to produce the final spectrum for each object.

Final processing of each asteroid's spectrum involved ratioing its summed spectrum by a solar analog star's spectrum in order to derive the relative reflectance at each wavelength. Often an average of two solar analog stars was used to match the airmass of the asteroid observations very closely. A final consistency check of the resulting spectra was performed at this point by visually comparing the spectra produced with an aperture size of 11 rows against the corresponding spectra produced with an aperture size of 21 rows. The NEA spectra produced with the smaller aperture generally yield a higher signal-to-noise ratio than those produced with the larger synthetic aperture since less sky noise is introduced.

At the red end of the spectrum strong night sky emission is often 100 times stronger than the object's signal. This has two deleterious effects. First, minute changes in spectral alignment, pixel sensitivity, and other effects can cause the night sky to be imperfectly subtracted. Second, even with perfect subtraction the noise will be dominated by photon noise from the night sky rather than signal from the object.

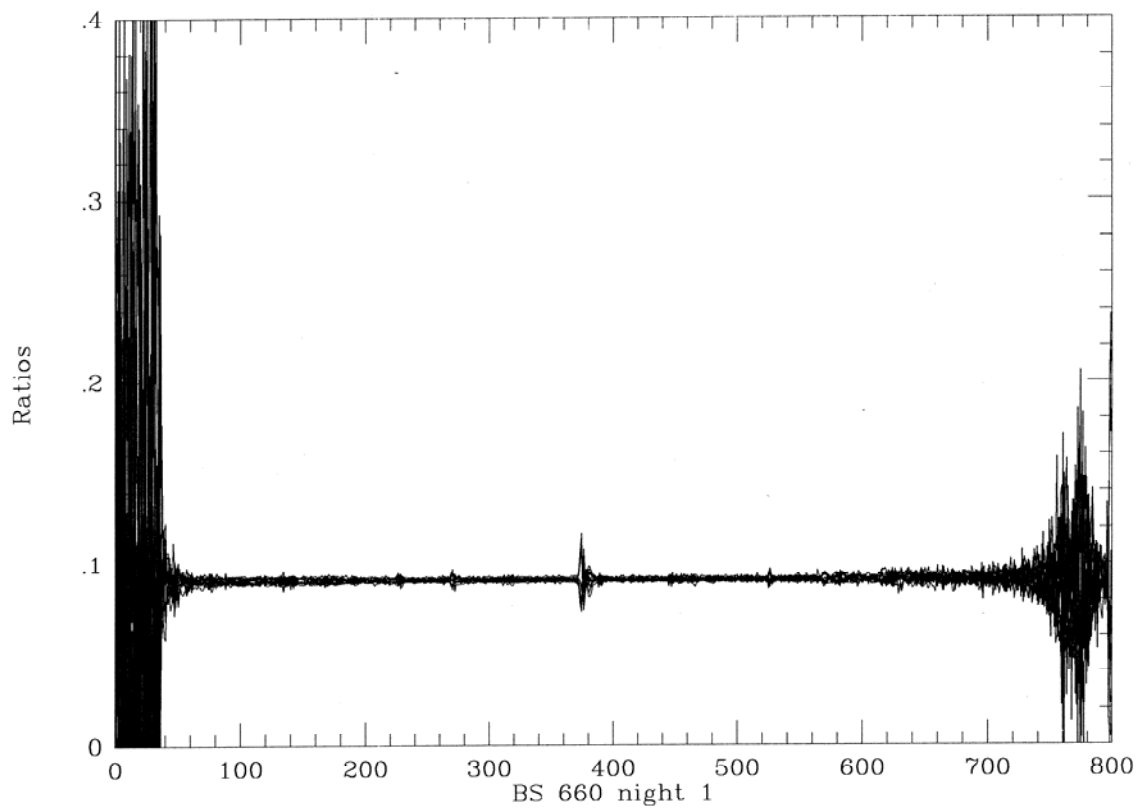


Figure 2.5. Ten superimposed ratioed spectra, used to look for spurious exposures in the individual spectra. The series of ratios shows that the exposures are consistent.

Unfortunately this is a critical region of the spectrum for asteroid classification because the 1- μm pyroxene/olivine absorption occurs here.

Representative spectra for each of the 41 NEAs in our extended survey (Fevig and Fink, 2006) are shown in Appendix A. Spectra for our 14 NEAs observed prior to 1997 can be found in Hicks, Fink and Grundy (1998). Spectral quality varied depending on the brightness of the object, total integration time, and sky conditions. Figures 2.6 and 2.7 show the range in the quality of the NEA spectra, with the spectrum for the large and bright (1036) Ganymed being of the highest quality and 1998 HE3 among the lowest. To increase the SNR for objects with low quality spectra, the data was binned into 50 pixel wide spectral regions roughly 360Å in width. The binned data points and one standard deviation error bars are plotted over the unbinned data in Figures 2.6 and 2.7 for all objects except (1036) Ganymed. (Note that this is not the error of the mean for each bin, in which case the error bars would be a factor of $\sqrt{50}$ smaller since the bin width is 50 pixels.) Also shown in these plots are the potentially problematic regions over this wavelength range where telluric absorptions and solar H_{α} can negatively affect the spectra.

Multiple spectra were obtained for virtually all of the observed objects. These spectra were graded and weighted according to their quality. The average grades for all spectra for a given object are shown in Table 2.2 and give an indication of the relative quality of all spectra for each object. The spectral parameters, mean slope, and mean band depth for a given object were computed based on a weighted average of these quantities. The weighted standard deviation for each of these parameters was computed,

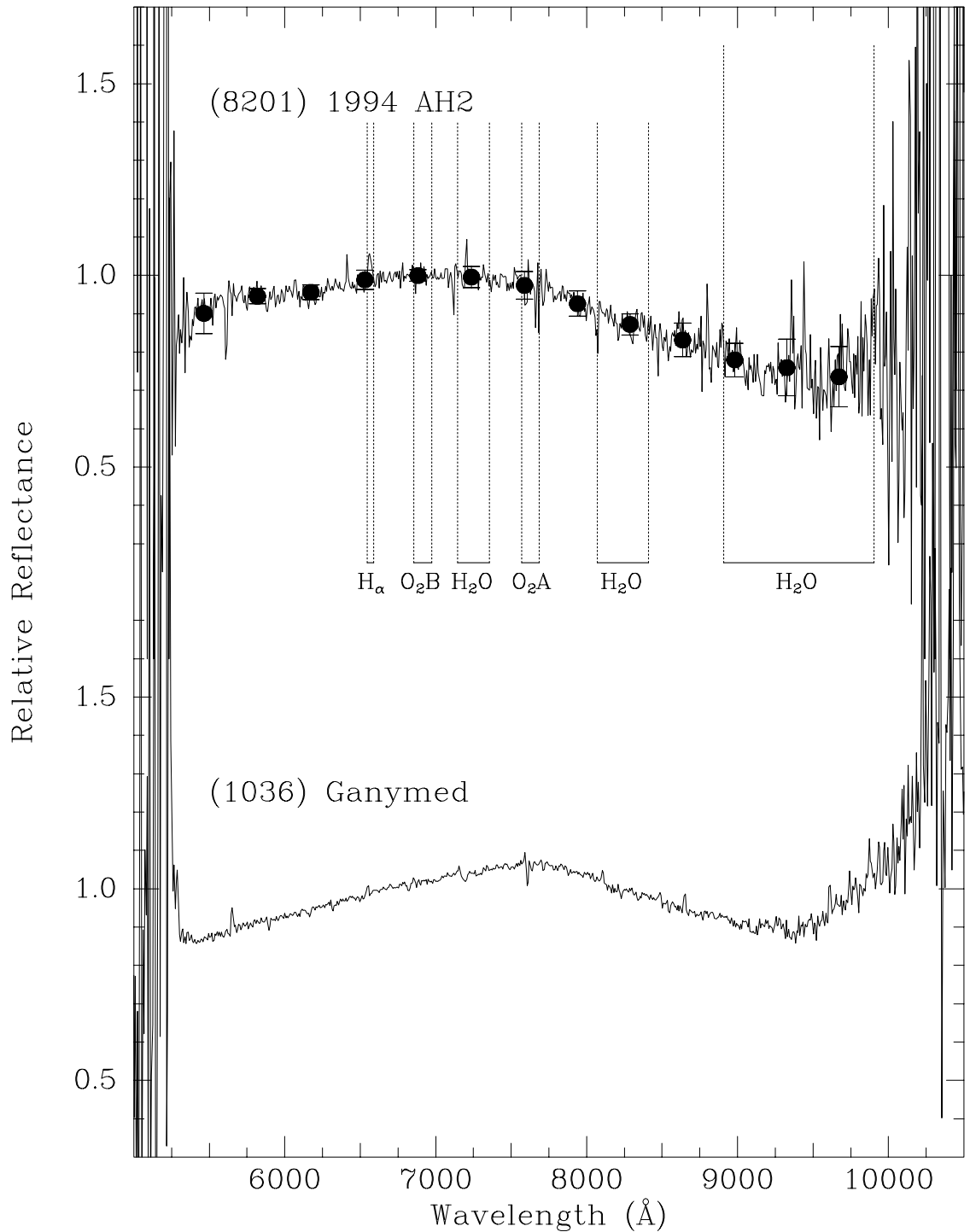


Figure 2.6. *Top*: An example of a moderately high SNR spectrum (OC-like object 1994 AH2, $V_{\text{mag}} = 15.4$, integration time = 77 min.). Positions of telluric absorption bands and the solar H α line are shown. *Bottom*: An example of a high SNR spectrum (S-type object Ganymed, $V_{\text{mag}} = 11.2$, integration time = 15 min.).

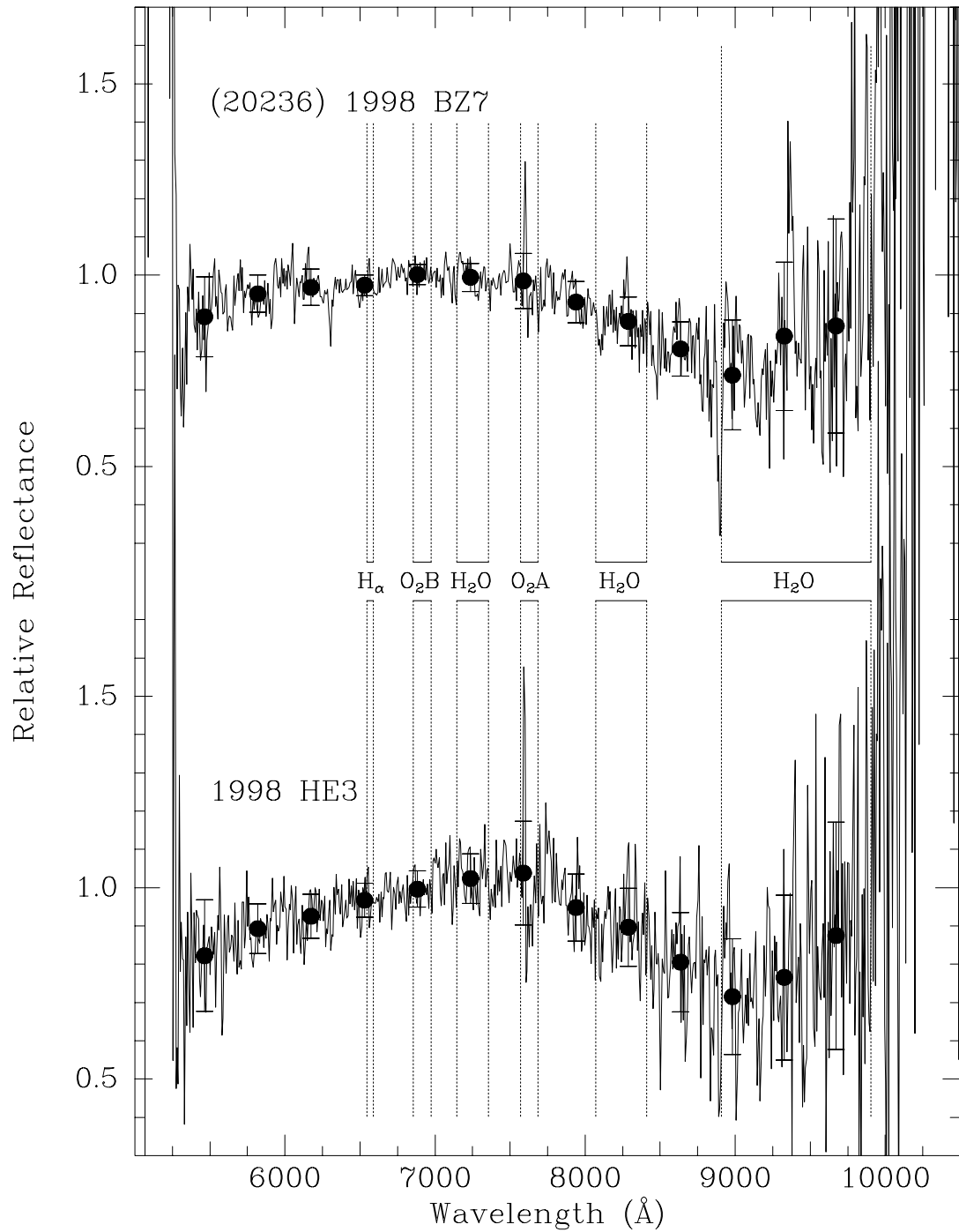


Figure 2.7. *Top*: An example of a spectrum with a moderate SNR (1998 BZ7, $V_{\text{mag}} = 16.5$, integration time = 220 min.). *Bottom*: An example of a moderately low SNR spectrum (1998 HE3, $V_{\text{mag}} = 17.2$, integration time = 114 min.). The spectral noise grows quite large above 9500 Å due to the rapidly falling CCD sensitivity, the strong night sky emissions and the telluric H $_2$ O absorption bands.

Table 2.2 - Supplemental Classification Information

Object	Mean Grade ^a	Potential Tholen Classification	Known Albedo ^b	Assumed Albedo ^c
(433) Eros	A	S	0.21	
(1036) Ganymed	A	S	0.17	
(1627) Ivar	C	S	0.15	
(1685) Toro	C+	Q	0.31	
(1862) Apollo	C	Q	0.26	
(1866) Sisyphus	B	S	0.15	
(1943) Anteros	C+	SA?	0.18	
(1980) Tezcatlipoca	A	S	0.14	
(3103) Eger	B	X	0.53	
(3122) Florence	B-	S	0.2	
(3199) Nefertiti	B-	S	0.41	
(3671) Dionysus	C+	CX	0.16	
(4183) Cuno	C+	Q		0.19
(4341) Poseidon	C+	Q		0.19
(4954) Eric	B+	S		0.19
(5587) 1990 SB	C-	Q	0.32	
(5751) Zao	B-	X	0.36	
(5836) 1993 MF	C-	SQ?		0.19
(6037) 1988 EG	C+	Q		0.19
(7358) 1995 YA3	B	S		0.19
(7482) 1994 PC1	C-	SA?		0.19
(7753) 1988 XB	C	FB?		0.05
(7822) 1991 CS	C+	SA	0.14	
(7977) 1977 QQ5	D	AS		0.40
(8201) 1994 AH2	B	Q		0.19
(10563) Izhdubar	C-	Q		0.19
(11066) Sigurd	C-	S		0.19
(13651) 1997 BR	D	S		0.19
(19356) 1997 GH3	C-	Q	0.34	
(20236) 1998 BZ7	C+	QV		0.19
(20255) 1998 FX2	C-	QS		0.19
(35107) 1991 VH	C+	S		0.19
(85490) 1997 SE5	B	T		0.07
1997 GD32	C-	Q		0.19
1997 UH9	D	S		0.19
1997 US9	C	Q		0.19
1998 HE3	C-	R		0.38
1998 HT31	B-	SQ?		0.19
1998 ME3	C-	CF		0.05
1998 MS2	C-	Q		0.19
2004 LC2	B-	Q		0.19
(1566) Icarus	N.A.	Q	0.33	
(1620) Geographos	N.A.	SQ?	0.19	
(2063) Bacchus	N.A.	Q		0.19
(2102) Tantalus	N.A.	QV		0.19
(2201) Oljato	N.A.	Q	0.24	
(3200) Phaethon	N.A.	BG	0.11	
(4953) 1990 MU	N.A.	Q		0.19
(6053) 1993 BW3	N.A.	RV?	0.18	
(6489) Golevka	N.A.	Q	0.6	
(7092) Cadmus	N.A.	X		0.15
(8176) 1991 WA	N.A.	V		0.38
1994 ES1	N.A.	D?		0.34
1995 CR	N.A.	S		0.19
1996 JA1	N.A.	Q	0.3	

^a NEA spectra at the bottom were reported in Hicks, Fink and Grundy (1998) and were not graded in this same manner.

^b Refer to Table 3.1

^c Typical albedos for the indicated Tholen classification are from Xu et al. (1995). These in turn were estimates from Veeder et al. (1989).

giving a sense for the variation in these spectral parameters for each object. It should be noted that there is some indication of rotational variation for some of these objects. An analysis of spectral inhomogeneity in these objects, though, is beyond the scope of this study.

CHAPTER 3

SPECTRA AND THEIR CLASSIFICATION

This chapter describes the new asteroid classification method that was derived and used to categorize NEA spectra in addition to problems encountered with utilizing other asteroid classification methods. This new asteroid classification method that directly compares NEA spectra with spectral features of meteorites is described in Section 3.1. Spectra of the 41 NEAs from Fevig and Fink (2006) are presented in Section 3.2. Problems associated with using the Bus Taxonomy (Bus, 1999) for our combined NEA spectral data set (Hicks, Fink and Grundy, 1998; Fevig and Fink, 2006) are summarized in Section 3.3.

The term “1- μm absorption” is used extensively in this and subsequent chapters of the dissertation and deserves clarification. This refers to the pyroxene and olivine absorption features present in most asteroids of siliceous (i.e., containing silicate minerals) composition. The pyroxene feature extends from roughly 0.7- μm to 1.2- μm (band center \sim 0.93- μm) while the three overlapping olivine features extend roughly from 0.7- μm to 1.7- μm (band center \sim 1.2- μm) (Gaffey et al., 1993b). The center of the 1- μm absorption and its extent can vary according to the relative amount of pyroxene and olivine present. There is an additional pyroxene band centered near 1.8- μm and a broad spinel absorption centered at \sim 2.1- μm which cannot be addressed in this work.

3.1 – Method of classification

Spectra were parameterized to classify objects and to look for trends in slope and band depth for OC-like and S-type asteroids. To illustrate this, the spectrum of (1036) Ganymed (from Figure 2.6) is repeated in Figure 3.1 to show how the slope, and I_{\max} and I_{\min} parameters are measured. The spectral slope between $\sim 5500 \text{ \AA}$ and $\sim 7000 \text{ \AA}$, defined as the percent change per 1000 \AA at 6500 \AA , was measured for both the unbinned and binned spectra. For spectra which exhibited a $1\text{-}\mu\text{m}$ absorption, the intensity maximum (I_{\max}) near 7500 \AA and the intensity minimum (I_{\min}) in the $1\text{-}\mu\text{m}$ region was measured and used to compute a band depth (I_{\min}/I_{\max}) for these spectra. Increasing sky noise and decreasing detector sensitivity above $\sim 9500 \text{ \AA}$ does not allow the red end of the $1\text{-}\mu\text{m}$ absorption to be resolved. Thus a potentially better parameterization, such as a band depth determined from a continuum fit to points outside of this absorption or a band area (Gaffey et al., 1993a) cannot be used with our spectral data.

The preliminary method of classification had as its basis Tholen's taxonomy (Tholen, 1984). A description of this classification scheme is given in Appendix B. The preliminary classifications using the Tholen approach are shown in Table 2.2. From the mean color indices and associated standard deviations for each of Tholen's 14 taxonomic classes (Tholen, 1984) the ranges of slope and band depth parameters for each of these classes were determined. The resulting 2-dimensional slope and band depth spectral parameter space was then delimited according to these calculated ranges. For each of the NEAs in our spectral data set the most probable Tholen classification for a given object was determined based on where each of the spectral parameters from individual spectra

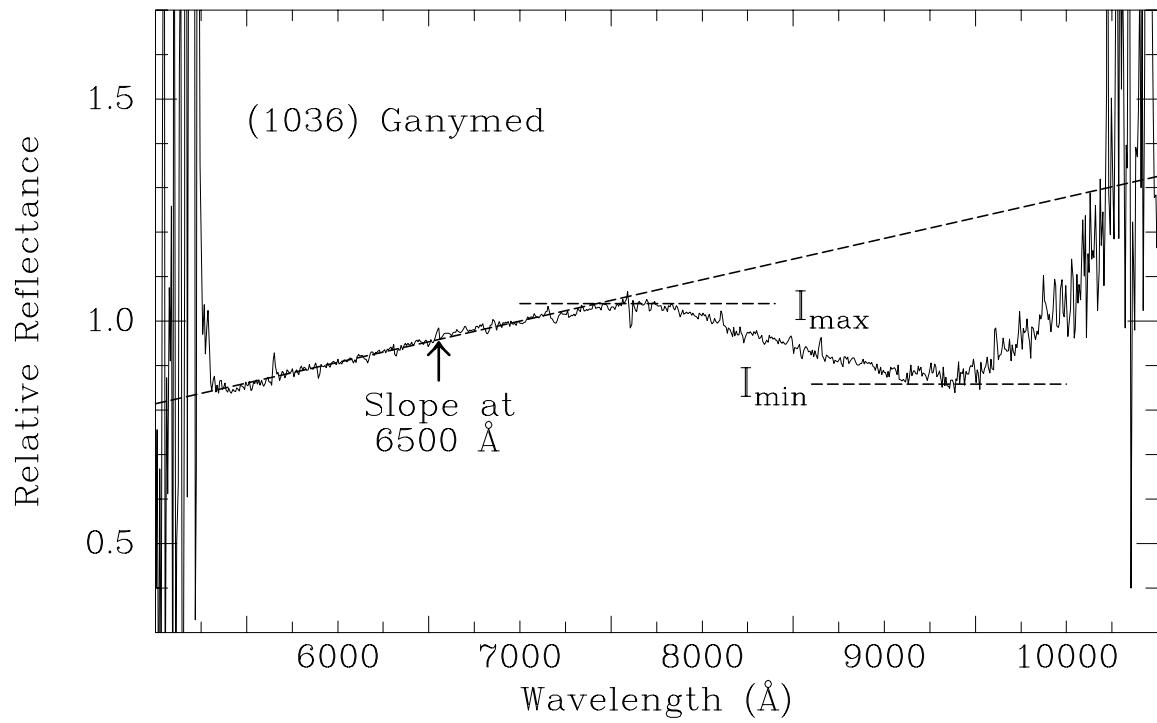


Figure 3.1. This plot illustrates the method by which the spectra are parameterized. The slope at 6500 \AA is measured along with the reflectance maximum, I_{\max} , and the reflectance minimum, I_{\min} .

(unbinned and binned) fell in spectral parameter space. Where ambiguities in classification arose the spectral quality and observing circumstances for each set of spectra for an object were carefully considered to arrive at a spectral classification. As part of our survey, spectra were also acquired of the prototypical Q ((1862) Apollo), R ((349) Dembowska), and V ((4) Vesta) types in Tholen's taxonomy, along with several S types. Taking into account the lower resolution, Tholen's 8-color plots agreed well with spectra of these objects (ref. discussion in sections 3.1.2, 3.1.3, and 3.1.4 and Figure 3.2). For some objects there was an ambiguity in its Tholen classification, in which case two letter designations corresponding to the most likely followed by the next most likely designation are shown. Some of the NEAs in our sample did not have an albedo measured directly. In such cases this Tholen classification was used to determine a reasonable albedo estimate (from Veeder et al. (1989) and shown in Table 2.2) and hence size estimate for such objects.

It should be pointed out that Tholen's taxonomy was based on asteroids in the main belt which have a totally different distribution of taxonomic classes than NEAs. Approximately 60% of Tholen's main belt objects showed no 1- μm absorption. They are associated with the Tholen D, T, X, B, C, F and G classes. In our database 9 objects which did not exhibit a 1- μm absorption were observed. These objects were classified as "Others". They comprise only ~16% of our NEA sample. A detailed discussion of these objects is given in Chapter 6. Tholen reports only one object in each of the classes Q (Apollo), R (Dembowska), V (Vesta) and 4 A class asteroids. These four groups taken together comprise $\leq 2\%$ of the population (Tholen, 1984; PDS asteroid taxonomy archive

at <http://www.psi.edu/pds/resource/taxonomy.html>). On the other hand among the NEAs in our sample roughly 42% Q types, 2 R types (possibly several V types which can't easily be distinguished from Q types) and no A types were observed. Only the S-class has a roughly similar population distribution. In the main belt they comprise about 40% while among the NEAs of our data they represent ~35% of the population. Two objects labeled BOC-like (described in section 3.1.1) were observed during our survey.

While Tholen's classification works reasonably well a more physical approach by directly comparing our spectra to laboratory spectral measurements of meteorite data was used. This method of classification is illustrated in Figure 3.2. In this figure the 1- μm band depth versus the slope between 5500 and 7000 \AA for laboratory measurements of meteorites and observations of S-class asteroids is plotted. The main resources for these data were Gaffey's meteorite spectral data base (Gaffey, 1976) and Gaffey's S-class asteroids (Gaffey et al., 1993a). The band depth and slope were measured for objects in these data bases. This endeavor was greatly aided by the recent availability of the meteorite data in electronic form (<http://www.psi.edu/pds/resource/gaffey.html>).

Gaffey's S-class asteroids are plotted as open triangles. His ordinary chondrites are plotted as open circles. Two major trends are apparent in this figure: (1) S type asteroids and ordinary chondrite meteorites occupy different regions of this plot, and (2) the two groups, nevertheless, are not clearly separated and blend into each other forming a continuum. The two groups separate roughly along a diagonal line running from the upper left to the lower right of the figure (band depth 1.0, slope 7.4% to band depth 0.7, slope 10.0%.) **This plot was used to classify our observed NEAs into OC-like objects**

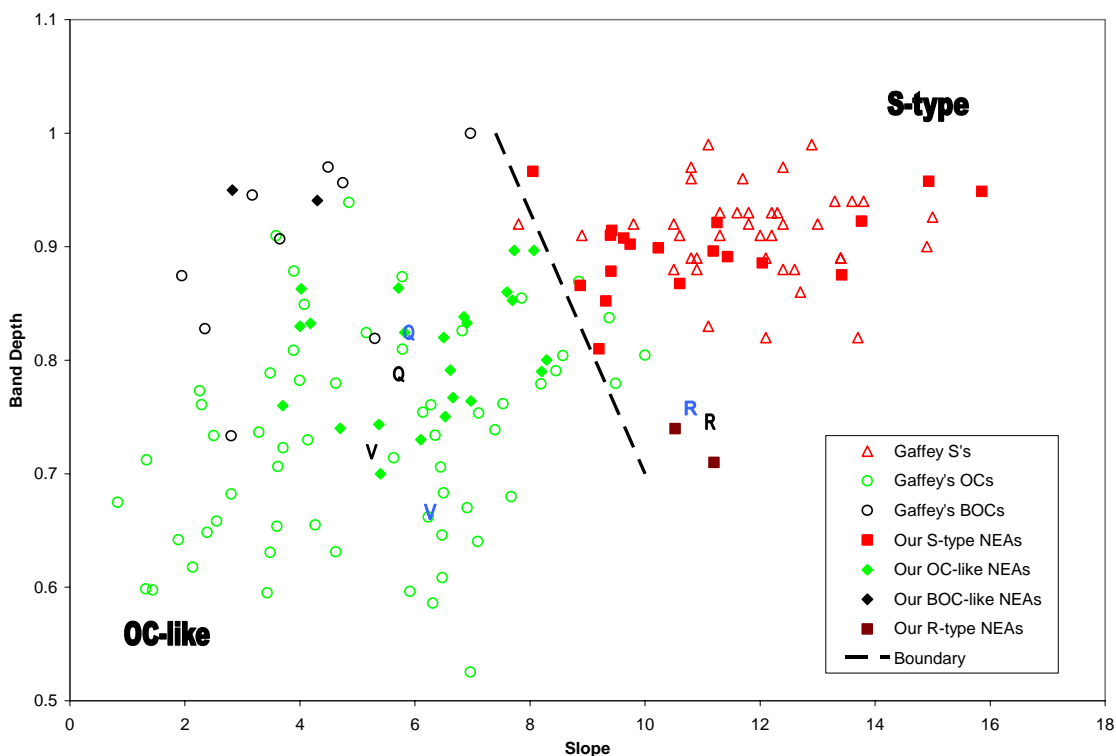


Figure 3.2. Plot of 1- μm band-depth vs. spectral slope which forms the basis of the classification scheme. Meteorite laboratory data and observations of S-class asteroids for the Gaffey databases are shown. Gaffey's S-class asteroids are plotted as open triangles and his ordinary chondrites (OCs) as open circles. Two trends are apparent in this figure: (1) S type asteroids and ordinary chondrite meteorites occupy different regions of this plot, and (2) the separation of the two groups, however, is not firm and appears to form a continuum. There are 23 NEAs classified as OC-like (filled green diamonds), 19 as S-types (filled red squares), two as BOC-like (filled black diamonds) and two as R-types (filled maroon squares). The prototypical Q, R, and V type asteroids that were used in the Tholen classification scheme (Tholen, 1984) were also observed. The measurements of our spectra for these objects are shown as blue letters and the measurements of Tholen's spectra are shown in black. For classification purposes an approximate diagonal dashed line separating the OC-like and S-type groups is drawn on the figure.

which fall in the region of Gaffey's ordinary chondrite meteorites and S-type objects which fall in the region of Gaffey's S-class asteroids. NEAs classified as S-types are plotted as filled squares and those classified as OC-like as filled diamonds. There are roughly 35% S-types and 42% OC-likes in our NEA sample.

A number of objects are plotted in this figure illustrating additional points.

3.1.1. Gaffey also has a number of ordinary chondrites which were spectrally altered by shock effects, being labeled as “black” ordinary chondrites by Britt and Pieters (1991). This shock blackening tends to neutralize the spectra of these meteorites, making both their slopes and 1- μm absorption shallower. They are plotted as black circles and appear to occupy a separate space in the upper left of the diagram. Two of our objects occupy this region and are classified as Black OC-like (BOC-like) objects. These two NEAs were not used in the orbital analysis of the OC-like and S-type population described in Section 4.2 of this dissertation since they are likely to have been optically altered, making it difficult to untangle the effects of space weathering from shock blackening.

3.1.2. As mentioned, OC-like asteroids are generally associated with the Tholen Q-class (McFadden et al., 1985). Tholen's single Q-class object, (1862) Apollo, which is shown on the figure as a black letter Q, falls roughly in the middle of the OC-like asteroids. The spectral parameters from our observations of Apollo, which is shown as a blue Q, plot very close to Tholen's Apollo.

3.1.3. The large V-class asteroid (4) Vesta both from Tholen's data (black V) and our own spectral observations (blue V) are plotted on this figure. They also agree quite well. As has been noted by others, the Vesta class of asteroids cannot be distinguished from the

OC-likes in this type of plot. To separate the ordinary chondrites from the achondrites which have been linked to Vesta (McCord et al., 1970; Larson and Fink, 1975) takes a plot of Bus's Principal Component 3 (Bus, 1999) which is sensitive to the blue/UV absorption or it requires the 0.9- to 2- μm band ratios (e.g. Gaffey, 1993a). In Binzel et al.'s (2004) data of 310 NEAs there were 14 asteroids classified as V types. Thus there may be a few V-class asteroids in our own sample. Using Binzel's roughly 5% V's among the NEAs could yield roughly 2 to 3 such objects within our dataset. These possibly are included in our OC-like dataset but will not substantially modify the statistical analysis presented later in this thesis. This problem of distinguishing V-class asteroids is revisited in Section 5.4 of this dissertation.

3.1.4. Tholen also classified one object, (349) Dembowska, as an R-class asteroid. This is plotted as a black R in Figure 3.2. Our observations of (349) Dembowska are plotted as a blue R on this figure, and again the agreement between the two observations is quite good. Two NEAs from our sample are close to that group and are classified as R-types. These two objects were excluded from the analysis in Section 4.3 of this dissertation.

To provide a reality check of the above parametric classification actual overlays of meteorite and NEA spectra are shown in Figure 3.3. OC-like, meteorite and S-type spectra are plotted. The top spectrum shows an H5 chondrite from Gaffey (1976). The next spectrum shows an OC-like NEA, (8201) 1994 AH2, overlaid by the H5 chondrite spectrum at top. The next spectrum shows another OC-like NEA, (4183) Cuno, overlaid by an LL3 chondrite spectrum (from Gaffey, 1976). There is an excellent match between these NEAs and ordinary chondrite meteorites. Two S-type spectra, (433) Eros and

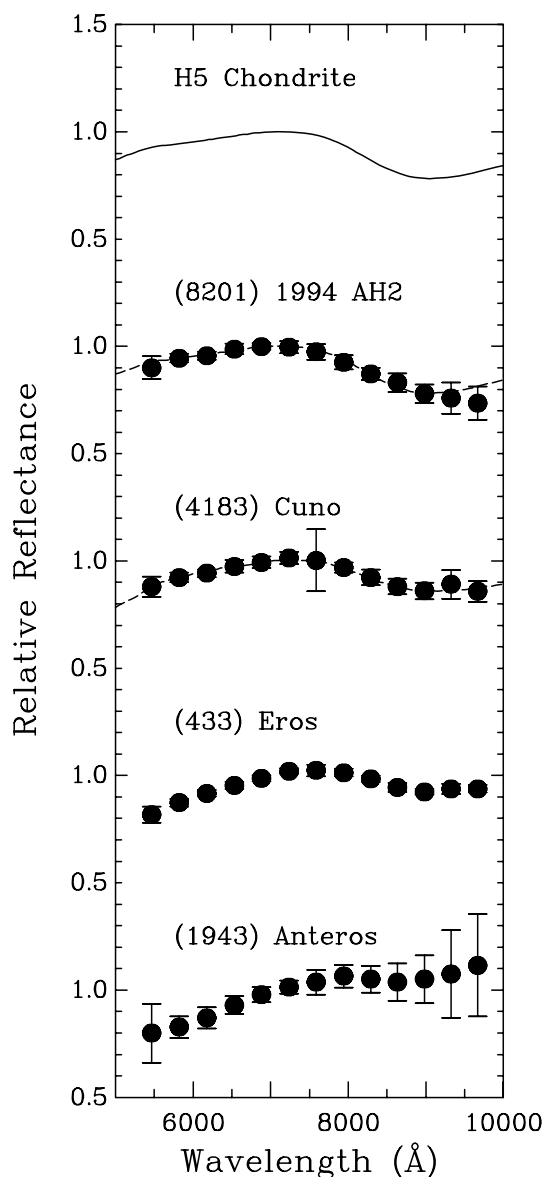


Figure 3.3. Sample spectra of two OC-like and two S-type NEAs (binned data points) along with laboratory meteorite spectra (continuous curves). The top spectrum shows an H5 chondrite from Gaffey (1976). The next spectrum shows (8201) 1994 AH2 overlaid by the H5 chondrite spectrum at top. The next spectrum shows (4183) Cuno overlaid by an LL3 chondrite spectrum (from Gaffey, 1976). There is an excellent match between these NEAs and OC meteorites. The next two spectra are S-type NEAs, (433) Eros and (1943) Anteros. The former has a slope and band depth closer to OCs than the latter. The figure shows the range of spectral characteristics among objects with 1- μm absorptions: from OC-likes with shallow slopes and deep 1- μm absorptions to S-types with steep slopes and shallow 1- μm absorptions. Spectra are plotted from 0.5 to 1.5 reflectance units and are displaced by 1 reflectance unit from each other.

(1943) Anteros are also plotted; the former having slope and band depth closer to ordinary chondrites than the latter. This plot shows how the slope changes from shallow to steep and band depth changes from deep to shallow between OC-like and S-type asteroids. The figure also illustrates that there exists a continuum of spectra among NEAs between those that match ordinary chondrites and S-type asteroids, in accordance with the space weathering hypothesis.

Space weathering of olivine- and pyroxene-bearing asteroids appears to have the following effects: it reddens the slope, diminishes the depth of the 1- μ m absorption, and makes objects darker, giving them lower albedos. It is thought to be caused by:

1. Solar wind particles (which likely produces extremely thin “coatings” of metallic iron on surficial grains of silicate minerals).
2. Micrometeoroid impacts (once again, thin coatings of iron on the surface of siliceous rocks is a likely by-product).
3. Energetic X-ray and UV irradiation (effects are unknown).
4. Other, perhaps less likely causes such as larger meteoroid impacts and cosmic ray bombardment.

Laboratory experiments have been conducted that attempt to determine how space weathering affects the surface reflectivity of ordinary chondrite material. Some of the more noteworthy experiments include the irradiation of olivine samples by hydrogen and helium ions to simulate the effects of the solar wind (Dukes et al., (1999)). It was found that a metallized coating of iron results which would produce the spectral effects attributed to space weathering (i.e., reddened slopes and diminished absorptions.) Sasaki

et al. (2001) simulated the effects of micrometeoroid bombardment using pulsed laser irradiation. Similar to ion bombardment experiments, a thin coating of metallic iron on the olivine grains resulted. The effect of energetic X-ray and UV irradiation does not seem to have been investigated since a literature search for such simulations did not yield any references.

The final classifications for the 41 objects observed since 1997 (Fevig and Fink, 2006) are given in Table 3.1 together with their physical parameters. This table is sorted according to asteroid number, or for objects that are not numbered, asteroid designation. The parameters for the 14 NEAs observed before 1997 (Hicks, Fink and Grundy, 1998) were classified in a manner consistent with the present analysis and are also included in the table. Osculating orbital elements (a,e,i), absolute magnitude (H), and measured or estimated diameters are shown for each object. Objects that have accurately measured lightcurves list rotational periods. Albedos are shown for objects where this quantity has been measured. The measured spectral slope for all NEAs, band depth for those with 1- μm absorptions, and spectral classification are listed. As explained above, these objects are classified into five groups; OC-like, BOC-like, S-type, R-type and Other.

3.2 - Spectra

The binned spectra for all 41 NEAs observed since 1997 are presented in Figures 3.4-3.6. All of the corresponding unbinned spectra are shown in Appendix A.

In order to present spectra of OC-like and R-type asteroids observed in a reasonably clear manner they are subdivided into 4 groups with similar characteristics.

Table 3.1 - Physical Parameters for Our Observed NEAs of Table 2.1

Object	a ^a	e ^a	i ^a	H ^a	Albedo ^b	D(km) ^c	Rotational Period ^b	Band Depth ^d	Spectral Slope ^d	Taxonomic Group
(433) Eros	1.458	0.223	10.83	11.16	0.21	23.6*	5.27	0.90 ± 0.01	11.2 ± 0.2	S-type
(1036) Ganymed	2.664	0.535	26.67	9.45	0.17	38.5*	10.31	0.87 ± 0.03	10.6 ± 0.6	S-type
(1627) Ivar	1.863	0.397	8.45	13.2	0.15	9.12*	4.795	0.87 ± 0.04	8.9 ± 1.9	S-type
(1685) Toro	1.367	0.436	9.38	14.23	0.31	3*	10.196	0.83 ± 0.06	6.9 ± 3.9	OC-like
(1862) Apollo	1.471	0.560	6.36	16.25	0.26	1.4*	3.065	0.82 ± 0.02	5.8 ± 2.0	OC-like
(1866) Sisyphus	1.894	0.539	41.17	13	0.15	8.48*	2.4	0.88 ± 0.03	9.4 ± 1.2	S-type
(1943) Anteros	1.430	0.256	8.70	15.75	0.18	1.8*	2.8695	0.95 ± 0.03	15.9 ± 1.2	S-type
(1980) Tezcatlipoca	1.710	0.365	26.85	13.92	0.14	6.7*	7.2523	0.92 ± 0.02	13.8 ± 1.3	S-type
(3103) Eger	1.405	0.355	20.93	15.38	0.53	2.5*	5.7059		4.9 ± 2.2	Other
(3122) Florence	1.769	0.423	22.16	14.2	0.2	2.5*	2.3581	0.90 ± 0.02	9.7 ± 3.3	S-type
(3199) Nefertiti	1.574	0.284	32.97	14.84	0.41	1.8*	3.0202	0.97 ± 0.01	8.1 ± 1.1	S-type
(3671) Dionysus	2.198	0.542	13.55	16.3	0.16	1.5*	2.705		1.8 ± 1.4	Other
(4183) Cuno	1.982	0.636	6.75	14.4		4.1	3.5595	0.84 ± 0.02	6.8 ± 2.0	OC-like
(4341) Poseidon	1.836	0.679	11.85	15.5		2.5	6.262	0.75 ± 0.08	6.5 ± 1.4	OC-like
(4954) Eric	2.001	0.448	17.47	12.6		9.3	12.056	0.92 ± 0.02	11.3 ± 0.7	S-type
(5587) 1990 SB	2.394	0.547	18.10	13.6	0.32	3.57*	5.0522	0.80 ± 0.03	8.3 ± 1.7	OC-like
(5751) Zao	2.104	0.422	16.06	14.8	0.36	2.3*	76		3.0 ± 0.6	Other
(5836) 1993 MF	2.445	0.532	7.98	13.9		5.1	4.959	0.95 ± 0.02	2.8 ± 0.7	BOC-like
(6037) 1988 EG	1.270	0.499	3.49	18.7		0.6	2.76	0.83 ± 0.02	4.2 ± 0.7	OC-like
(7358) 1995 YA3	2.197	0.503	4.66	14.4		4.1	5.488	0.90 ± 0.05	10.2 ± 1.4	S-type
(7482) 1994 PC1	1.346	0.328	33.49	16.8		1.3	2.5999	0.96 ± 0.03	14.9 ± 2.2	S-type
(7753) 1988 XB	1.467	0.482	3.12	18.6		1.1			-0.3 ± 0.1	Other
(7822) 1991 CS	1.123	0.165	37.12	17.4	0.14	1.1*	2.3893	0.89 ± 0.02	12.0 ± 1.2	S-type
(7977) 1977 QQ5	2.227	0.466	25.18	15.4		1.8	7.457	0.88 ± 0.05	13.4 ± 1.3	S-type
(8201) 1994 AH2	2.534	0.709	9.58	16.3		1.7	23.949	0.76 ± 0.03	7.0 ± 1.2	OC-like
(10563) Izhdubar	1.007	0.266	63.46	16.9		1.3	2.66	0.86 ± 0.02	5.7 ± 0.6	OC-like
(11066) Sigurd	1.392	0.375	36.89	15.2		2.8	8.4958	0.85 ± 0.00	9.3 ± 0.4	S-type
(13651) 1997 BR	1.336	0.306	17.24	17.6		0.9	33.644	0.89 ± 0.03	11.4 ± 4.8	S-type
(19356) 1997 GH3	2.492	0.568	2.99	17.1	0.34	0.91*	6.714	0.85 ± 0.03	7.7 ± 1.6	OC-like
(20236) 1998 BZ7	2.038	0.557	6.49	17.6		0.9	10.182	0.74 ± 0.01	5.4 ± 1.2	OC-like
(20255) 1998 FX2	2.152	0.492	9.96	18.2		0.7	6.826	0.90 ± 0.01	8.1 ± 4.1	OC-like
(35107) 1991 VH	1.136	0.144	13.92	16.9		1.3	2.624	0.91 ± 0.04	9.4 ± 1.6	S-type
(85490) 1997 SE5	3.730	0.666	2.61	14.8		5.6	9.0583		7.4 ± 0.8	Other
1997 GD32	2.101	0.601	5.30	21.36		0.2		0.79 ± 0.02	6.6 ± 0.4	OC-like
1997 UH9	0.830	0.475	25.49	18.68		0.6		0.91 ± 0.01	9.6 ± 1.6	S-type
1997 US9	1.052	0.282	20.02	17.3		1.1	3.52	0.90 ± 0.01	7.7 ± 1.8	OC-like
1998 HE3	0.879	0.441	3.40	21.72		0.1		0.74 ± 0.05	10.5 ± 1.8	R-type
1998 HT31	2.511	0.693	6.78	20.82		0.2		0.94 ± 0.01	4.3 ± 0.8	BOC-like
1998 ME3	2.178	0.482	5.99	19.25		0.9			1.2 ± 1.4	Other
1998 MS2	1.733	0.403	19.23	20.41		0.3		0.86 ± 0.02	4.0 ± 1.3	OC-like
2004 LC2	1.878	0.737	10.98	18.64		0.6		0.77 ± 0.00	6.7 ± 0.2	OC-like
(1566) Icarus	1.078	0.827	22.85	16.9	0.33	1.3*	2.273	0.76 ± 0.05	3.7 ± 1.3	OC-like
(1620) Geographos	1.245	0.335	13.34	15.6	0.19	2.3 ^e	5.2233	0.81 ± 0.04	9.2 ± 1.3	S-type
(2063) Bacchus	1.078	0.349	9.44	17.1		1.2	14.904	0.86 ± 0.02	7.6 ± 1.2	OC-like
(2102) Tantalus	1.290	0.299	64.01	16.2		1.8	2.391	0.74 ± 0.04	4.7 ± 0.7	OC-like
(2201) Ojato	2.172	0.713	2.52	15.25	0.24	2.1*	26	0.83 ± 0.05	4.0 ± 1.7	OC-like
(3200) Phaethon	1.271	0.890	22.17	14.6	0.11	5.1*	3.604		-1.8 ± 0.7	Other
(4953) 1990 MU	1.621	0.657	24.41	14.1		4.7	14.218	0.73 ± 0.04	6.1 ± 1.0	OC-like
(6053) 1993 BW3	2.147	0.529	21.60	15.1	0.18	3.1*	2.573419	0.71 ± 0.06	11.2 ± 1.5	R-type
(6489) Golevka	2.497	0.605	2.28	19.2	0.6	0.3 ^e	6.0264	0.82 ± 0.05	6.5 ± 1.3	OC-like
(7092) Cadmus	2.525	0.702	17.83	15.4		2.9			3.0 ± 1.0	Other
(8176) 1991 WA	1.575	0.643	39.63	17.1		0.8	7.111	0.70 ± 0.06	5.4 ± 1.3	OC-like
1994 ES1	1.425	0.594	0.92	28.55		0.012			21.0 ± 15.0	Other
1995 CR	0.907	0.868	4.03	21.67		0.1		0.91 ± 0.07	9.4 ± 1.6	S-type
1996 JA1	2.561	0.702	21.85	21.05	0.3	0.2*	5.227	0.79 ± 0.02	8.2 ± 0.4	OC-like

^a Osculating orbital elements at epoch 2453600.5 JDT and absolute magnitude from Lowell Observatory's 'ASTORB' database, <ftp://ftp.lowell.edu/pub/elgb/astorb.html>

^b Albedo and rotational period from the European Asteroid Research Node's (E.A.R.N.) Near-Earth Asteroid database, <http://pentium.pe.ba.dlr.de/nea/>

^c Asteroid diameters with an asterisk are from the E.A.R.N database. All other diameters are based on the typical albedo for their taxonomic class and their H magnitude.

^d Band depth and spectral slope for NEAs of siliceous composition as defined in the text.

^e E.A.R.N. lists the axial dimensions for (1620) Geographos, 5x2x1.5 km, and (6489) Golevka, 0.35x0.25x0.25 km. Shown in the table is the diameter of each object based on their albedo and H Magnitude.

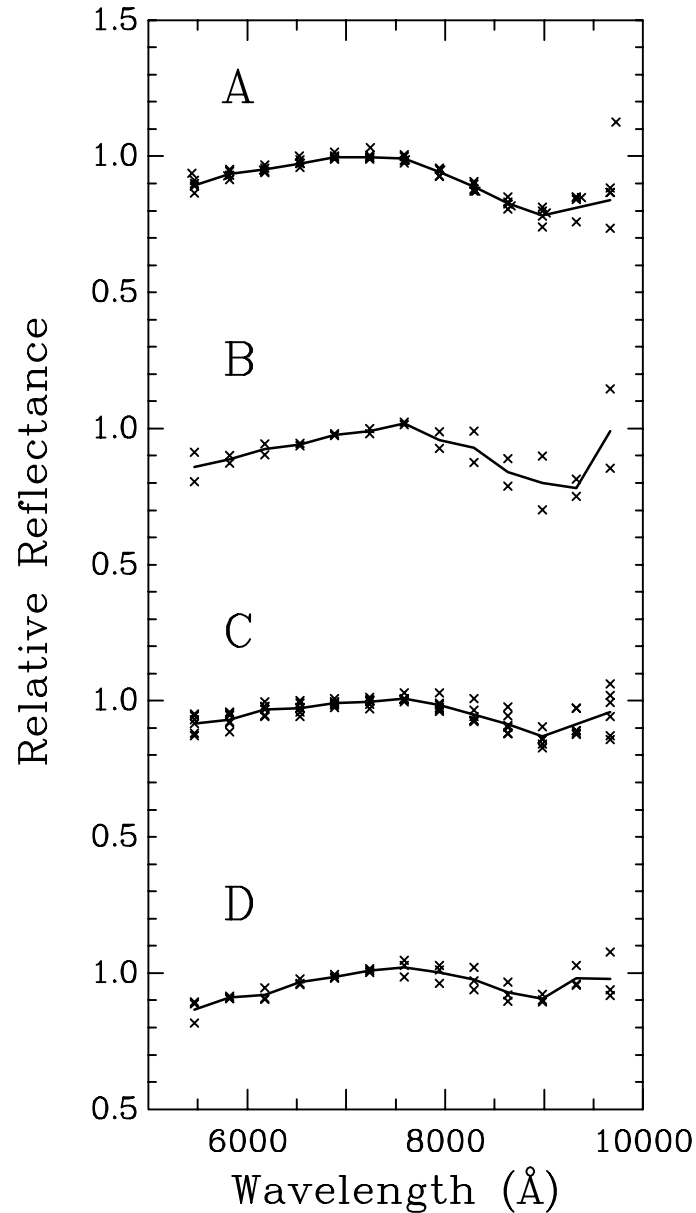


Figure 3.4. A plot of 16 of our observed OC-like and R-type NEAs ordered according to their mean slope and band depth. Group A NEAs have shallow slopes and deep band depths. Group B NEAs have moderate slopes and deep band depths. Group C NEAs have shallow slopes and moderate band depths. Group D NEAs have moderate slopes and moderate band depths. The solid line is the mean of each group. The groups are delimited as follows: shallow slopes (slope $< 7.3\%$), moderate slopes (slope $> 7.3\%$), deep band depths ($I_{\min}/I_{\max} < 0.81$), and moderate band depths ($I_{\min}/I_{\max} > 0.81$). See text for the objects in each group. Spectra are displaced as in Figure 3.3.

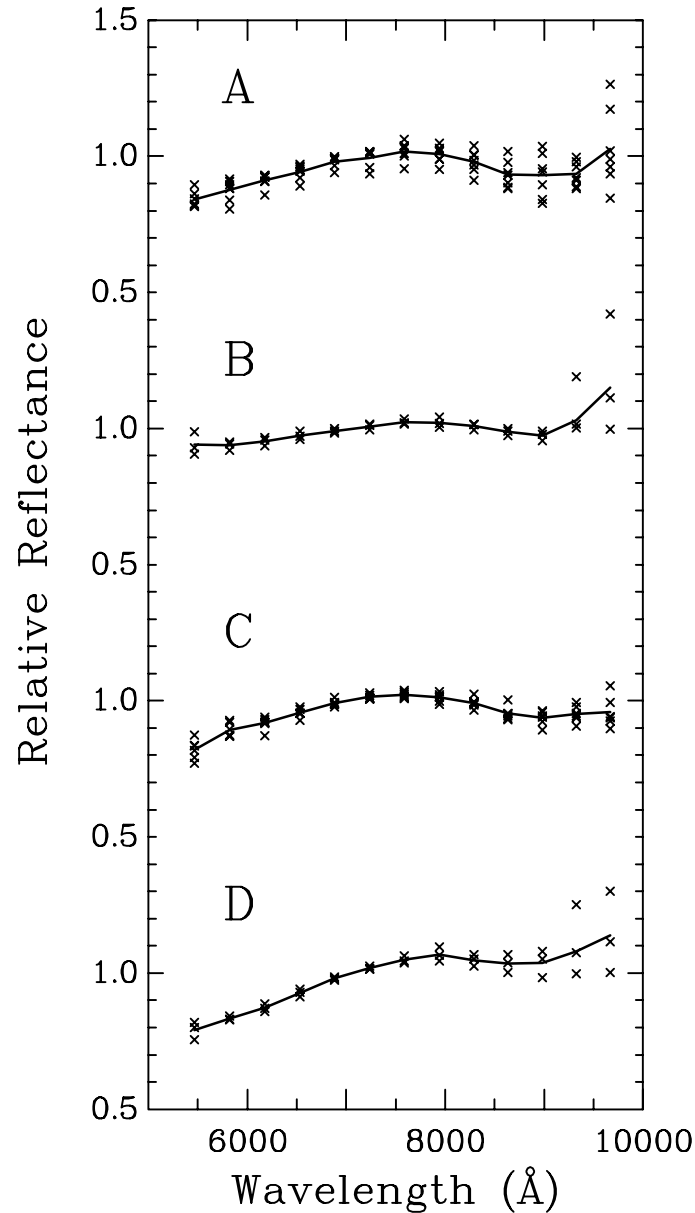


Figure 3.5. A plot of 19 of our observed S-type and BOC-like NEAs grouped according to their mean slope and band depth. NEAs in group A have moderate band depths. Group B NEAs have shallow slopes and shallow band depths. Group C NEAs have moderate slopes and shallow band depths. Group D NEAs have steep slopes and shallow band depths. The solid line is the mean of each group. The groups are delimited as follows: shallow slopes (slope $< 8.5\%$), moderate slopes ($8.5\% < \text{slope} < 12.9\%$), steep slopes (slope $> 12.9\%$), moderate band depths ($I_{\min}/I_{\max} < 0.894$), and shallow band depths ($I_{\min}/I_{\max} > 0.894$). See text for the objects in each group. Spectra are displaced as in Figure 3.3.

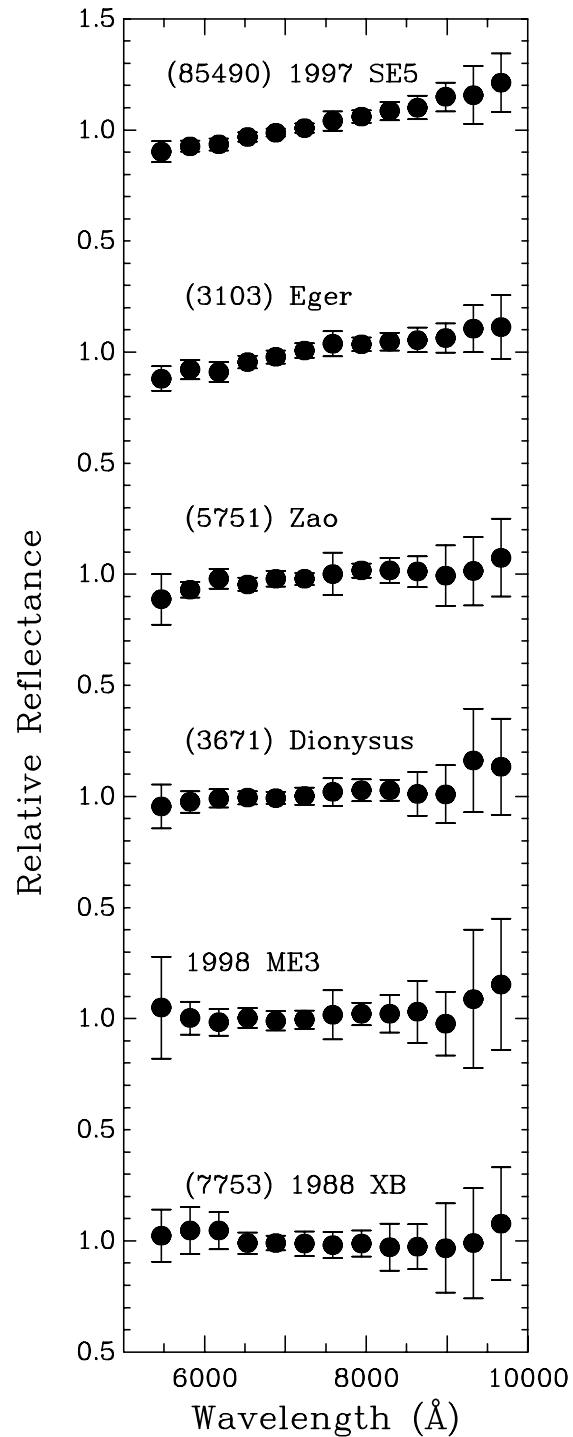


Figure 3.6. NEAs in our sample that do not exhibit a 1- μm absorption feature are shown. These objects span the space between the very red-sloped extinct comet candidate (85490) 1997 SE5 to the slightly blue-sloped (7753) 1988 XB. Spectra are displaced as in Figure 3.3.

These are displayed in Figure 3.4. The delimiting quantities (slope and band depth) for these groups are given in the figure caption. Asteroids in group A have a relatively shallow slope and deep band depth; asteroids in group B have a moderate slope and deep band depth; asteroids in group C have a shallow slope and moderate band depth while group D asteroids have both a relatively moderate slope and moderate band depth. The exact delimitations for each group are given in the caption for Figure 3.4. Group A asteroids are (20236) 1998 BZ7, (4341) Poseidon, (8201) 1994 AH2, 2004 LC2, and 1997 GD32. Group B asteroids are 1998 HE3 and (5587) 1990 SB. Group C asteroids are (1862) Apollo, (6037) 1988 EG, (1685) Toro, (4183) Cuno, 1998 MS2, and (10563) Izhdubar. Group D asteroids are (19356) 1997 GH3, 1997 US9, and (20255) 1998 FX2.

Similarly for purposes of display S-type and BOC-like asteroids are divided into four groups in Figure 3.5. Again, the delimiting quantities for these groups are given in the figure caption. Asteroids in group A have a moderate band depth; asteroids in group B have a shallow slope and shallow band depth; asteroids in group C have moderate slope and shallow band depth while group D asteroids have both relatively steep slope and shallow band depth. The exact delimitations for each group are given in the caption for Figure 3.5. Group A asteroids are (1627) Ivar, (11066) Sigurd, (1866) Sisyphus, (1036) Ganymed, (13651) 1997 BR, (7822) 1991 CS, and (7977) 1977 QQ5. Group B asteroids are (5836) 1993 MF, 1998 HT31, and (3199) Nefertiti. Group C asteroids are (35107) 1991 VH, 1997 UH9, (3122) Florence, (7358) 1995 YA3, (433) Eros, and (4954) Eric. Group D asteroids are (1980) Tezcatlipoca, (7482) 1994 PC1, and (1943) Anteros.

In Figure 3.6 the spectra of 6 NEAs that exhibit no discernible absorptions are shown. Included in this plot is the NEA extinct comet candidate, (85490) 1997 SE5. This very red-sloped asteroid is in a cometary orbit since its Tisserand parameter (Danby, 1988) is 2.66, significantly less than 3.0, the delimitation between asteroids and Jupiter Family comets (Weissman et al., 1989). Asteroid (3103) Eger also exhibits a linear, rather red-slope, though its orbit and high albedo (0.53) imply that it is not an extinct comet. It should be noted this very interesting object has been intensively studied by Gaffey et al. (1992). Also shown in this plot are asteroids that exhibit slightly red ((5751) Zao, (3671) Dionysus and 1998 ME3) to slightly blue slopes ((7753) 1988 XB). A detailed analysis of these objects is given in Chapter 6.

3.3 – The Bus classification method and Principal Component Analysis

While the Tholen classification scheme can be reasonably well combined with one described above, the same can not be said about the Bus taxonomy (Bus, 1999). This taxonomy is based on CCD spectroscopic observations of 1447 (primarily main belt) asteroids over a wavelength range of 4400 to 9200 Å. It uses Principal Component Analysis and attempts to be consistent with the Tholen taxonomy. One problem with using the Bus taxonomy is that it partitions the asteroids into 26 separate classes, more than can be supported by our observations of 55 asteroids. In reality, the only significant clustering in their data is for those objects that exhibit a 1- μm absorption and those that do not (Bus and Binzel, 2002b). Furthermore, this taxonomy is not entirely consistent

with the Tholen taxonomy. Some members of Bus's X-class show a 1- μm absorption while Tholen's X-class clearly does not have a 1- μm absorption.

The difficulty in transforming the Bus taxonomy to physical parameters is illustrated in Chapter 5 where the larger Binzel et al. (2004a) dataset was used to corroborate the findings of Chapter 4. There is not a ready correspondence between the parameters measured for our spectra and Bus's Slope, PC2' and PC3' parameters. His Slope parameter is measured over their entire wavelength range, from 4400 to 9200 \AA , and includes the 1- μm absorption region. The slope parameter used to classify our spectra is only over the essentially featureless portion of all asteroid spectra from 5500 \AA to 7000 \AA . According to Bus and Binzel (2002a), PC2' is most sensitive to the depth of the 1- μm absorption while PC3' is more sensitive to a UV or 7000 \AA absorption. It was found, however, that PC2' is not necessarily well correlated with a 1- μm absorption, nor is it clear that PC3' can be very well-correlated with a UV absorption shortward of 5500 \AA . A detailed explanation of these difficulties with the Bus taxonomy is given in Appendix B.

As an exercise a Principal Component Analysis on our NEA and Gaffey's data was performed. No additional information was gained by doing such an analysis as compared to the one outlined in section 3.1. The Principal Component Analysis that was performed on our NEA dataset is explained in Appendix B.

As is pointed out in Bus and Binzel (2002b), "taxonomy does not necessarily equate to mineralogy." Once Principal Component Analysis is applied to asteroid spectra, the relationship to physical mineralogical features can become obscured. The

classification method outlined at the beginning of this chapter begins to approach the ideal stated by Bell et al. (1989) that “the true value of classification can only be realized if a class name can be firmly linked with a surface chemical composition.” This parameterization method is simple, applicable to any spectrum that includes the wavelength range of our observations, and is directly related to the mineralogical features over this wavelength range: in particular the slope over the featureless portion of asteroid spectra and the 1- μm band depth (or absence thereof) associated with a pyroxene/olivine absorption. This classification method relies on the direct comparison of NEA spectral parameters with the same spectral parameters for meteorites to classify OC-like and BOC-like objects, and the careful work of Gaffey et al. (1993a) to classify S-types. The R-types are consistent with the prototypical R-class asteroid, (349) Dembowska, in Tholen's taxonomy and "Others" are objects with linear, featureless spectra.

CHAPTER 4

ANALYSIS OF OUR SPECTRAL DATA

Compared to S-type spectra, ordinary chondrites are characterized by quite deep 1- μm absorptions and shallow spectral slopes shortward of $\sim 7000 \text{ \AA}$. As mentioned several times, until fairly recently, not many asteroid spectra exhibiting these features had been observed.

To analyze our observations a number of correlations for the two groups of S-type and OC-like NEAs were investigated. These included correlations of taxonomic classifications and spectral parameters with semi-major axis, eccentricity, inclination, perihelion and aphelion distance, absolute magnitude and, from measured or estimated albedo information for an object, size. Most of these investigations did not yield statistically significant correlations.

Four significant results were found during this parameter search which is described in sections 4.1, 4.2 and 4.3 below and is illustrate in Figures 3.2, 4.1, 4.2 and 4.3:

1. There is no clear boundary between the spectral features of S-type and OC-like NEAs. The objects in our sample exhibit a continuum of spectral parameters between these two types.
2. There is no size-dependent trend for NEAs that have a 1- μm absorption.
3. S-type NEAs tend to reside in low eccentricity orbits while the opposite is true for OC-like NEAs.

4. Apollo class asteroids which cross the asteroid main-belt are predominantly OC-like objects.

4.1 – The continuum of spectral types between OC-like and S-type NEAs

Figure 3.2 was discussed earlier and forms the basis of the classification method. It clearly shows a continuum of objects whose spectra span the gap between S-type asteroids and ordinary chondrites. The same trends can be seen in the data of Binzel et al. (1996a). Since space weathering is a slow continuous process one would expect a continuum of objects from young unweathered surfaces with spectral features that closely match ordinary chondrites to mature weathered surfaces that match S-type asteroids. If our data had yielded two distinct groups of S-type and OC-like objects with no intermediate case it could have been interpreted as two distinct, compositionally separate groups, instead of the same type of object modified by a continuous slow weathering process.

4.2 – Size-dependent trends

As was pointed out in Chapter 1, no characterized main-belt asteroids have spectra similar to OCs while many NEAs do. To explain the lack of objects that resemble ordinary chondrites in the asteroid main belt, it has been hypothesized that main belt OC-like bodies are small and below the limits of spectroscopic detection. Smaller objects might appear fresh (OC-like) because the frequency of catastrophically disruptive events increases as an asteroid's size decreases. Bell et al. (1989) suggest that the parent bodies of ordinary chondrites were too small to differentiate. Due to their small size they

were ground down to even smaller sizes by impacts more rapidly than the larger and, at least partially, differentiated S-type parent bodies. Gaffey et al. (1989) offered another explanation: that an event heated the surfaces of ordinary chondrite parent bodies, melting the mantle but leaving the core undifferentiated. Subsequent collisions released a large numbers of small, undifferentiated ordinary chondrites. If either of these scenarios is valid, one ought to see a different size trend for OC-like and S-type objects. Small objects are difficult to observe in the asteroid main-belt but relatively easy among the NEAs since they approach close to Earth. If OC-like objects are predominantly small this trend could persist among the NEAs.

Our dataset spans the range of the largest NEA, (1036) Ganymed (diameter \sim 30km) to one of the smallest spectroscopically observed NEAs, 1994 ES1 (diameter \sim 12m). Size-dependent trends were looked for in the parameterized data with plots of band depth versus size and slope versus size. If there were a trend toward smaller objects being OC-like and larger ones S-type, one would expect to see an increasing slope and decreasing band depth (i.e., increasing I_{\min}/I_{\max} in our data) with increasing size. These plots are shown in Figure 4.1. Only the 46 NEAs from our dataset which have a 1- μ m absorption are included in these plots. The 9 objects that have neutral to red linear slopes (i.e., those classified as “Others”) are not represented in these figures. Both plots in Figure 4.1 look more or less like scatter plots with no readily discernible trends in the data. A statistical analysis of this data was performed and no statistically significant trend was found. Therefore, over the size range spanned by our dataset there is little or no indication that OC-like objects tend to be among the small members of the NEA

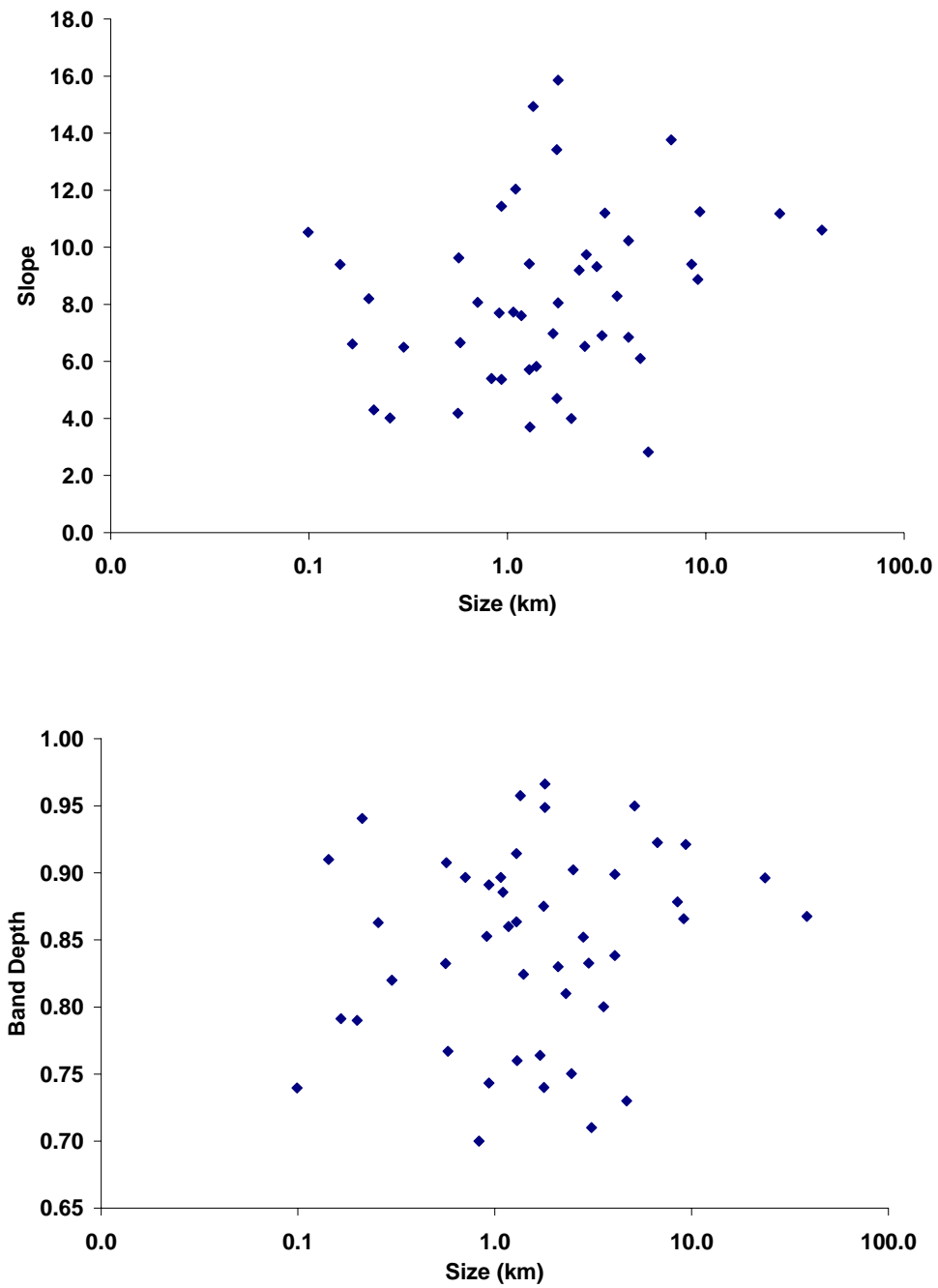


Figure 4.1. Slope vs. size for our NEAs (top panel). Band depth vs. size for our NEAs (bottom panel). There is no discernible size-dependent trend in this data.

population and S-types among the large. Thus the hypothesis that smaller NEAs tend to be OC-like (Hicks, Fink and Grundy, 1998) is not confirmed, or is at best very tenuous, in our enlarged dataset. It should be noted that there can be substantial uncertainties and biases among the size estimates derived from radiometric observations for small NEAs since such objects are likely to have relatively rocky, regolith-free surfaces for which simple thermal models cannot be readily applied (Harris and Lagerros, 2002). It is also possible that with additional observations using the suite of large telescopes coming on line (yielding better signal-to-noise ratio and extending the observed size-range to smaller objects) a trend may become evident.

4.3 – Orbit-dependent trends

Figure 4.2 is a plot of the eccentricity, e , versus semi-major axis, a , for S-type and OC-like NEAs in our sample. The eccentricity distribution of OC-like and S-type bodies appears clearly bimodal. Most OC-like bodies tend to be in highly eccentric orbits (15 with $e > 0.5$, only 8 with $e < 0.5$) while most S-type bodies are in lower eccentricity orbits (only 4 with $e > 0.5$, 15 with $e < 0.5$).

Figure 4.3 is a plot of aphelion distance, Q , versus perihelion distance, q , for this same subset of our data. Objects above the shaded line encounter main belt objects during their orbit. The solid vertical line represents Earth's aphelion distance and separates the Amors (which cross Mars's orbit but not that of the Earth) from the Apollos. The solid diagonal line separates the Atens from the Apollos. Several trends are evident in this representation: the vast majority of Apollos in our sample which encounter main-

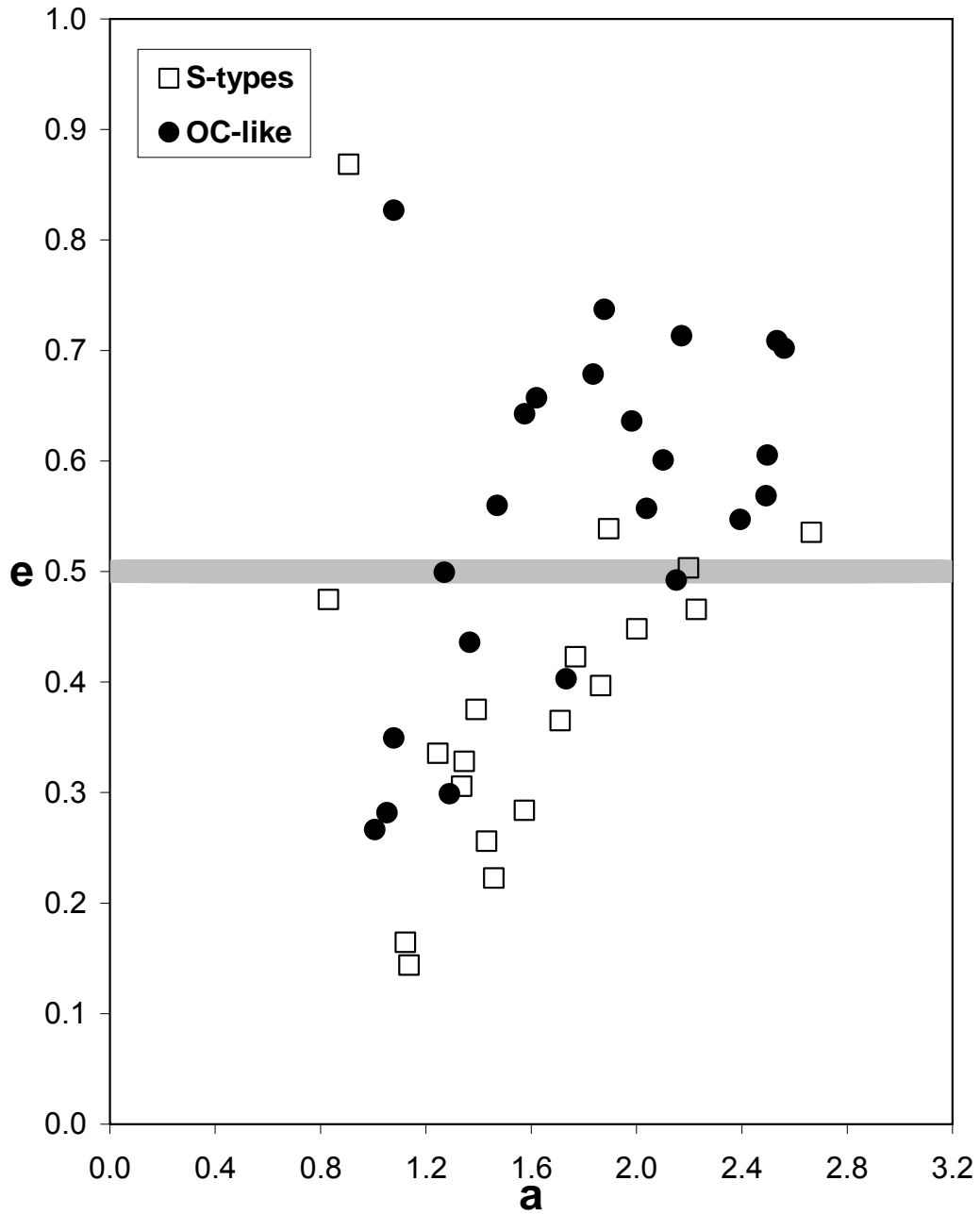


Figure 4.2. A plot of eccentricity, e , vs. semi-major axis, a , for S-type (squares) and OC-like (circles) NEAs from our sample. The majority of objects with OC-like spectra occupy highly eccentric orbits.

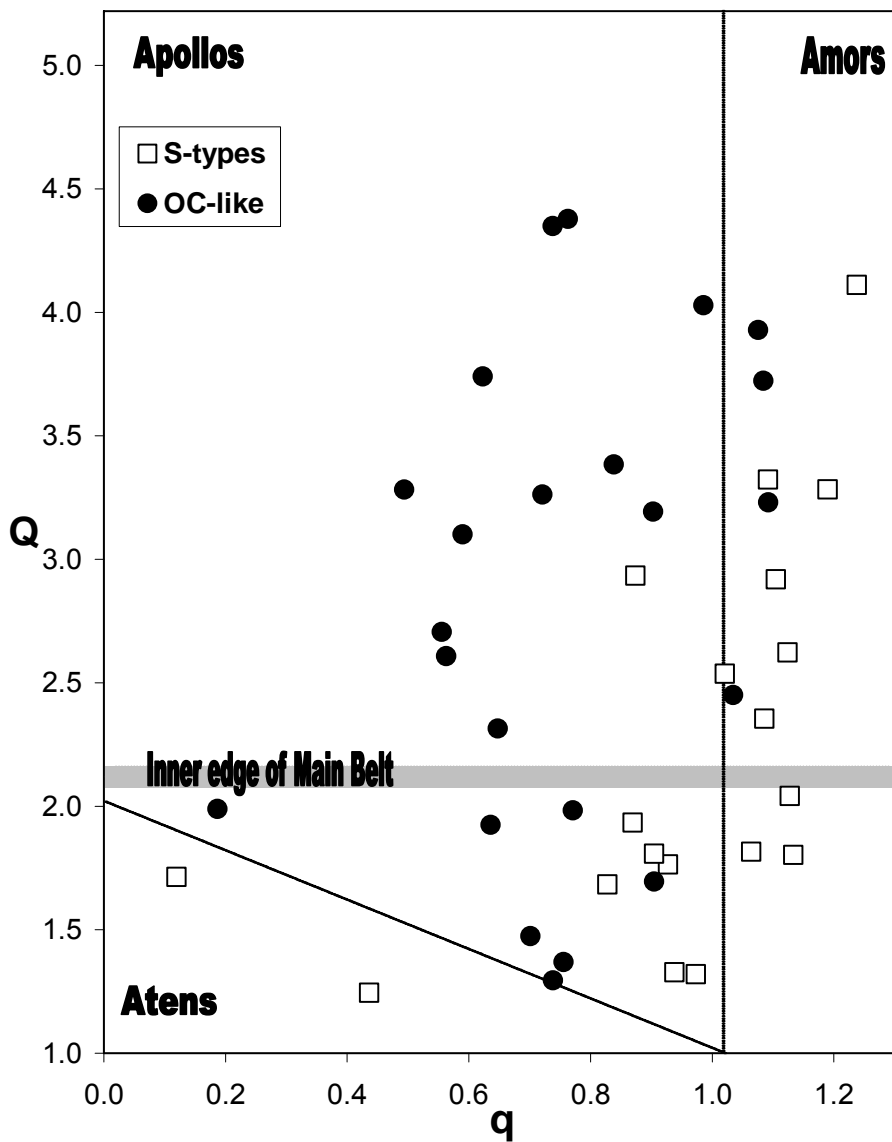


Figure 4.3. A plot of aphelion distance, Q , vs. perihelion distance, q , for S-type (squares) and OC-like (circles) NEAs from our sample. The solid band represents the approximate inner edge of the asteroid main belt. The vertical line at 1.017 AU represents Earth's aphelion distance and delimits the Amors. The slanted line in the lower left separates the Apollos from the Atens. The objects with OC-like spectra in our sample are skewed toward Apollos which enter the main-belt.

belt objects are OC-like asteroids; the Amor population appears to have an overabundance of S-type objects; Atens and Apollos which do not enter the main-belt are a mixture of S-types and OC-like objects. These results came as a surprise since no such trend had been described before. Sufficiently large numbers of NEA spectroscopic observations were not available before these trends were first reported (Fevig and Fink, 2001), so that apparently it had gone unnoticed. These results provide constraints for NEA dynamical and collisional models.

Although the trends in eccentricity and (q,Q)-space are readily visible in Figures 4.2 and 4.3, statistical hypothesis tests were applied to check the veracity of these conclusions: namely the χ^2 -test, the Kolmogorov-Smirnov test, and the Student t-Test. These tests are used in this and subsequent chapters of this dissertation to determine if there are statistically significant differences between the distributions and means of two data sets. In each test, an assumption is made about the relationship of the two data sets (the null hypothesis), a statistical quantity is computed from the observed data (a test statistic), and the location of that test statistic along its associated distribution is determined. If this test statistic lies in the tail of this distribution, then there is some level of confidence that the null hypothesis is false. By convention, confidence levels above 90% for a given test are considered to indicate possibly significant results, while 95% indicates a significant result, and above 99% a very significant result (i.e., the null hypothesis is almost certainly incorrect.)

To test the significance of the trends for S-type versus OC-like NEAs in eccentricity and (q,Q)-space the χ^2 -test for two binned data sets was used (Press et al.,

2001). This method allows one to test for differences between distributions without presupposing an underlying distribution. The data in Figure 4.2 was binned in eccentricity according to a low-eccentricity ($e < 0.5$) bin where S-type bodies dominate the distribution and a high-eccentricity bin ($e > 0.5$) where OC-like bodies are prevalent. The χ^2 value was then computed from the observed number of S-type and OC-like NEAs in each bin. Its value was found to be far enough out in the tail of the χ^2 distribution to cause doubt that the observed number of S-type and OC-like NEAs were drawn from eccentricity distributions that were the same (the null hypothesis). The χ^2 -test of the significance of this result shows the two distributions are different at a confidence level of 98.3%. This confidence level implies that the relative proportion of S-type to OC-like NEAs in low-eccentricity versus high-eccentricity orbits is significantly different.

Similarly, the data in Figure 4.3 was divided into four bins in order to perform a χ^2 -test on the distributions of S-type and OC-like NEAs in (q,Q) space. The boundaries for these four regions were defined by $Q = 2.1$ AU (the approximate inner edge of the asteroid main-belt) and $q = 1.017$ AU (Earth's aphelion distance). In this case, the results of the χ^2 -test showed the two distributions to be different at a confidence level of 98.8%. This high confidence level again implies that the S-type and OC-like NEAs have significantly different distributions in (q,Q) space and supports the hypothesis that OC-like NEAs are skewed toward Apollos which enter the main-belt.

Like the χ^2 -test above, the Kolmogorov-Smirnov (K-S) test (Press et al., 2001) was used to judge the difference between the eccentricity distributions for S-type and OC-like NEAs. In this case, the test statistic for the K-S test is the absolute value of the

maximum difference between the cumulative distribution functions for the observed eccentricities. This test statistic's distribution under the assumption that the two eccentricity distributions are the same (the null hypothesis) can be approximated (Press et al., 2001), allowing the significance level of the test to be determined. The K-S test on the eccentricities of our S-type and OC-like NEAs gave a highly significant confidence level of 99.9%, indicating that the eccentricity distributions of these two spectral types are indeed very different.

The Student t-Test can be used to judge the significance of the difference between two means (Press et al., 2001). The test statistic, Student's t , is based on the standard error of the difference of the means for two data sets. Its value with respect to Student's distribution yields the significance level of the test. For the purpose of this statistical analysis, the difference between the mean eccentricity of OC-likes versus the mean eccentricity of S-types was tested. From the Student t-Test it was found the two means were different at a highly significant confidence level of 99.8%.

After considering the results in Figures 4.2 and 4.3, the most likely explanation that came to mind was that objects in highly eccentric orbits which impact main-belt objects (which are on relatively circular orbits) will suffer more catastrophic collisions due to the relatively large difference in their velocity vectors. Their velocity vectors will be closer to orthogonal than objects in low eccentricity orbits, such as Amors that cross the asteroid main-belt. This is analogous to the collision two vehicles would experience if they impacted at right angles versus a glancing blow while merging on a highway, the former being far more catastrophic than the latter even though the speeds of the vehicles

in both scenarios may be the same. Such collisions are expected to either catastrophically disrupt an NEA, producing fragments with freshly exposed surfaces, or to essentially cause the surface age of the NEA to be reset to zero by exposing fresh regolith.

Not only do asteroids in highly eccentric orbits that impact main-belt objects suffer more energetic impacts, they also suffer more impacts with main-belt objects. NEAs in such orbits spend a considerable fraction of their orbital period in the main-belt near aphelion and relatively little time outside of the main-belt near perihelion. As these asteroids slowly traverse the main-belt near aphelion they cross the paths of numerous main-belt objects. As pointed out in the preceding paragraph, there is a relatively large difference in velocity between the two objects. The net effect of these circumstances is to increase the flux of impactors on NEAs in such orbits.

A literature search revealed that these simple arguments can be supported by dynamical calculations. Bottke et al. (1996) produced maps in (a,e,i) space which allow estimation of the frequency of catastrophic disruption for NEAs. These maps (e.g., Figure 7 in that publication) show that the frequency of catastrophic collisions increases greatly for NEAs in highly eccentric orbits that cross the asteroid main-belt. Such objects will have shorter collisional lifetimes or, at the very least, the frequency with which their surface ages are reset to zero will increase. Therefore, the average surface age of these objects will be younger than NEAs which occupy other types of orbits. These dynamical results are in accordance with our spectral data which show that the majority of these high eccentricity NEAs are OC-like bodies while the Atens, Amors and low eccentricity Apollos are a mixture of S-type and OC-like asteroids.

To arrive at a scenario that can explain these observed results the question of how main belt asteroids evolve into NEAs in the first place must be addressed. The lifetimes of objects in NEA space is estimated to be several million years (Gladman et al., 1997; Morbidelli et al., 2002). Thus the population of NEAs has to be continually replenished during a time scale of roughly the same length. It is generally believed that most main-belt asteroids evolve into NEAs from the vicinity of strong resonances in the asteroid main-belt (Morbidelli et al., 2002). ProtoNEAs are transported to these resonances via the velocity change imparted by the collision that produced the object or the Yarkovsky effect (Bottke et al., 2002b) or both. The Yarkovsky effect slowly alters the orbits of asteroids due to anisotropic radiation of thermal energy. The lifetime of a protoNEA's migration into a strong resonance is not certain but appears to be at least tens of millions of years (Marti and Graf, 1992). Once in a strong resonance such as the ν_6 , 2:1, 3:1, or 5:2, an asteroid's eccentricity increases rapidly, allowing it to become Earth-approaching on a timescale of ~ 0.5 -1 million years (Morbidelli et al., 2002).

Timescales for space weathering range from 50,000 years to 100 MY (Chapman, 2004). The most likely timescale is a few million years (Nesvorný et al., 2005). Based on this estimate and considering it typically takes tens of millions of years for a main belt object to evolve into Near Earth space, one would expect nearly all such objects to be weathered by the time they evolve into an NEA orbit. Thus in order to explain the large fraction of fresh OC-like objects among the high eccentricity NEA population a scenario that produces fresh surfaces on a timescale of a few million years or less in the Near Earth environment is required.

A scenario that could explain this is as follows. Main belt asteroids have their eccentricity “pumped up” by interactions with resonances. Once such objects reach the orbit of Mars they can be gravitationally perturbed out of their resonances and into slower evolving, relatively low eccentricity Amor class orbits. Those that are not perturbed by Mars continue to have their eccentricities increased. These objects can then be decoupled from the resonance by gravitational interactions with Earth, Venus and possibly Mercury, ending up in high eccentricity orbits. These NEAs which cross a number of terrestrial planet orbits are in particularly chaotic orbits so their orbital parameters, in particular their eccentricity, e , and aphelion distance, Q , change on short timescales. Those asteroids where eccentricity is high and aphelion distance is beyond the inner edge of the asteroid main-belt (~ 2.1 AU) are in a collisionally enhanced environment where their surface is modified by either a catastrophic disruption or “regolith gardening” (i.e., frequent overturning of the regolith), exposing fresh unweathered material as described in pages 68 and 69. The surfaces of such NEAs are “young” inasmuch as they have not been exposed to the space environment for a long time period. This leads to an increased abundance of NEAs in high eccentricity orbits with OC-like spectra. When the orbits of such NEAs evolve further through interactions with planets and they become decoupled from the asteroid main-belt (e decreases and $Q < 2.1$ AU) they enter a more quiescent environment where space weathering instead of impact processes becomes the dominant surface modifying mechanism as their surfaces are allowed to age.

In a random sample of the NEA population one would thus expect to see objects with surface ages that span the gap from young and fresh (OC-like) to old and weathered (S-type), which is precisely what is observed (cf. Figure 3.2 and Figure 3.3).

Another scenario could explain our observations. Asteroids that have collisions in the main-belt will produce fresh resulting fragments as well as impart a considerable change in velocity. Given the proper change in velocity vector a fraction of these fragments could enter the Near Earth environment very quickly. Without dynamical calculations one would expect however that these objects are partitioned into a range of eccentricities not necessarily favoring higher eccentricities. Probably only a very small fraction is required to provide enough flux to populate the Near Earth environment with fresh objects. Quantitative estimates for this scenario in the literature were searched for but no calculations for this case have been found. Alternatively if a collision occurs close to a strong resonance some fraction of the collisional fragments may evolve into highly eccentric Earth-approaching orbits before they have time to weather.

Tidal disruption induced modifications to NEA surfaces is a third scenario that may explain our observations. An NEA must pass within several planetary radii to a terrestrial planet for tidal disruption to occur (Richardson et al., 1998). All NEAs that enter the main-belt cross the orbit of Mars, but high eccentricity Apollo asteroids also cross the orbits of several terrestrial planets: at least Earth's orbit and if q is small enough for an NEA, Venus and Mercury. Therefore, a higher probability of experiencing a tidal disruption exists for asteroids in such orbits. As the orbits of such NEAs precess they can

make sufficiently close approaches to terrestrial planets so that tidal effects can disrupt an object, or at least churn its regolith sufficiently so the surface appears fresh.

Any of the above three hypotheses, or a combination thereof, can explain the large fraction (~50%) of fresh objects that were observed, *particularly in high eccentricity orbits*. It will require further modeling of orbital evolution, collision processes, tidal disruptions and their timescales to see whether one of these scenarios is dominant.

4.4 - Summary

1. OC-like objects are quite abundant among the NEAs (Table 3.1 and Figure 3.2). In our data sample there are 23 OC-like and 19 S-type NEAs. This corroborates the earlier work of Hicks, Fink and Grundy (1998) as well as the results of other researchers (e.g. Binzel et al., 1996, 2004; Whiteley, 2001).
2. The spectral characterization of S-type asteroids and OC-like NEAs appear to merge and form a continuum (Figure 3.2 and Figure 3.3) rather than being two clearly separated groups. This has also been noted by others (e.g. Binzel et al., 1996).
3. OC-like objects tend to occupy high eccentricity orbits that intersect the asteroid main belt (Figure 4.2 and Figure 4.3).
4. OC-like objects appear to dominate the Apollo group of asteroids which reside in a potentially more severe collisional environment.

The objects in our spectral survey that are in highly eccentric orbits are probably youngest and have relatively fresh surfaces. Three methods are proposed by which these

fresh surfaces can be produced. First, NEAs in such orbits that also cross the asteroid main-belt are in a collisionally enhanced environment. Such an environment will reset the surface age of objects fairly frequently due to collisions with main-belt objects. Second, objects produced in main-belt collisions can be injected into strong resonances that rapidly increase their orbital eccentricity. These impact-produced fragments may be transported into NEA orbits on a short timescale before their surfaces age substantially. Finally, Apollo class NEAs in highly eccentric orbits can make close approaches to terrestrial planets. If such an approach is sufficiently close tidal forces can disrupt a rubble-pile asteroid. Following a tidal disruption event and the re-accretion of some of its component parts, the surface age of an NEA will likely be reset to zero as previously unexposed subsurface material now resides on the surface. These three processes can form freshly surfaced NEAs which exhibit OC-like spectra. These objects then undergo space weathering which transforms their surface reflectance over time to match S-type asteroids. In a sample of such NEAs having different surface ages one would expect to see a continuum of spectral parameters between OC-like and S-type asteroids. Since the mean lifetime for NEAs is several million years a steady state population of about 55% OC-likes and 45% S-types results. Thus, the conclusions from this analysis strongly support the space weathering hypothesis.

CHAPTER 5

OC-LIKE AND S-TYPE NEAS IN BINZEL ET AL. (2004a)

This chapter presents the results of an analysis combining our data and that of Binzel et al. (2004a). The purpose of this analysis is to verify the results in Chapter 4 using this larger dataset. The primary obstacle is to convert their classification method to a physical description of OC-like and S-type objects. Since they do not use the same spectral parameterization methods as ours, analyzing the two datasets in the same manner is not straightforward.

NEAs were characterized in Binzel et al. (2004a) using Principal Component Analysis in accordance with the Bus taxonomy (Bus, 1999). Three Principal Components resulted from this analysis: Slope, PC2' and PC3'. Slope corresponds to a spectrum's overall slope and PC2' roughly corresponds to the depth of its 1- μm absorption (Bus and Binzel, 2002b). These two parameters, though, cannot simply be used as a proxy for our slope and band depth spectral parameters. These problems have been touched upon earlier (Section 3.3) and are explained in more detail in Appendix B.

Two methods by which the Binzel/Bus classification scheme can be transferred to one that is consistent with my own were examined. The first method, outlined in section 5.1, uses an analysis of 33 NEAs in common between the two data sets. This includes a separate statistical cross check in tabular form in section 5.2. The second method, presented in section 5.3, uses an analysis by Bus (1999) of 78 of Gaffey's (1976) meteorite spectra using the same Principal Component Analysis for NEAs as employed in

Binzel et al. (2004a). This chapter concludes with a brief discussion of the problems associated with recognizing basaltic V-class (Vesta) asteroids in both Binzel's and our dataset.

5.1 - Combining Binzel's and our data into one data set using 40 NEAs observed in common by the two groups

The basis for my classification (Figure 3.2) shows that with our slope and band depth parameterization, the NEAs fall into roughly 5 reasonably distinct groups; OC-like, S-type, BOC-like, R-type, and "Others" which do not exhibit a 1- μm absorption. The OC-likes and S-types will be used in the analyses in this chapter.

To classify Binzel's data into OC-like and S-type objects a subset of 33 asteroids that were observed by both Binzel and us were taken. These were classified as OC-likes or S-types in Chapter 3, Table 3.1. Binzel assigned Slope and PC2' values to these 33 objects. These objects are plotted using the Slope and PC2' values as given by Binzel et al. (2004a) in Figure 5.1. Our OC-like NEAs are plotted as green diamonds and our S-types as red squares. It can be seen that they fall into reasonably distinct regions. The boundary lines in the (Slope, PC2')-space can now be drawn which separate the OC-like NEAs, those to the left of Line 1, from the S-type NEAs, those to the right of Line 2. The area between the lines is a region of overlap and uncertainty.

These dividing lines are transferred onto the plot of Binzel et al.'s (2004a) data (Figure 5.2). This now allows Binzel's objects to be grouped into S-types (primarily composed of the Bus and Binzel S, Sa, Sk, Sl, S(IV), K, L, Ld, and A classes which are

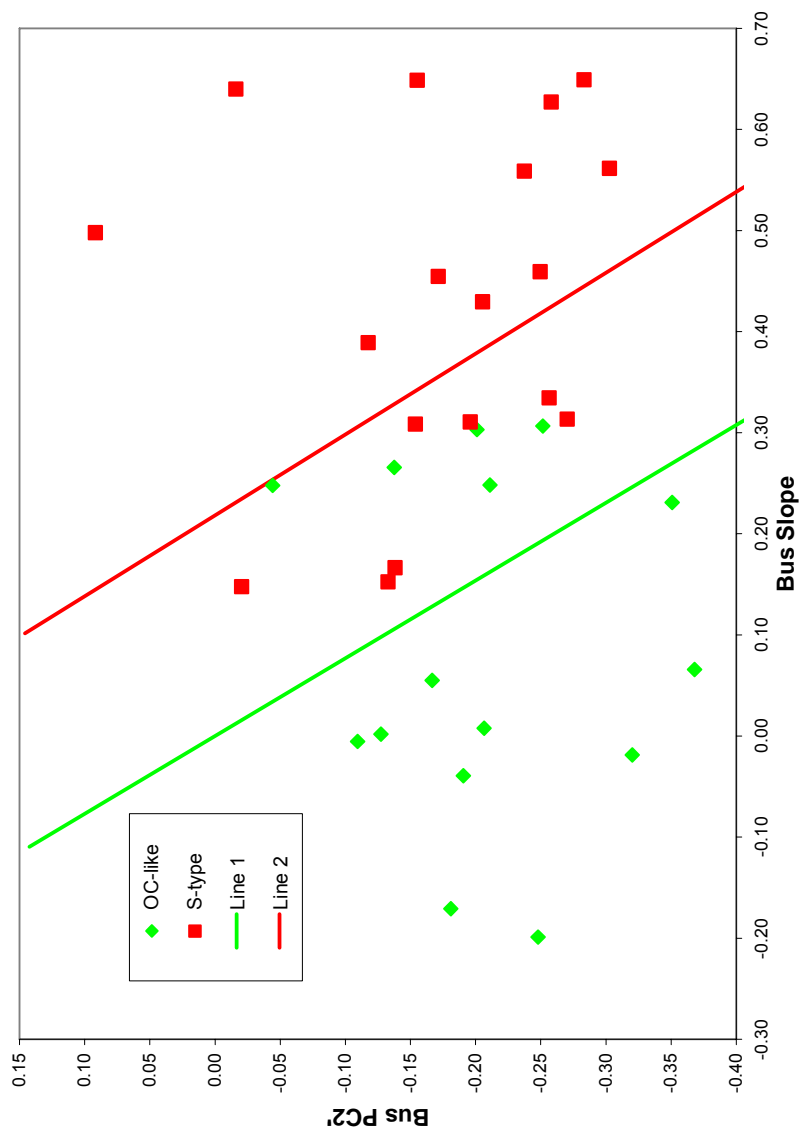


Figure 5.1. Principal Component plot of NEAs observed by us and also classified by Binzel et al. (2004a). Their Slope and PC2' values for objects classified as OC-like (green diamonds) and S-type NEAs (red squares) in this dissertation are shown. The green and red lines delimit the region of uncertainty where it is unclear in Principal Component space whether an object exhibits OC-like or S-type spectra.

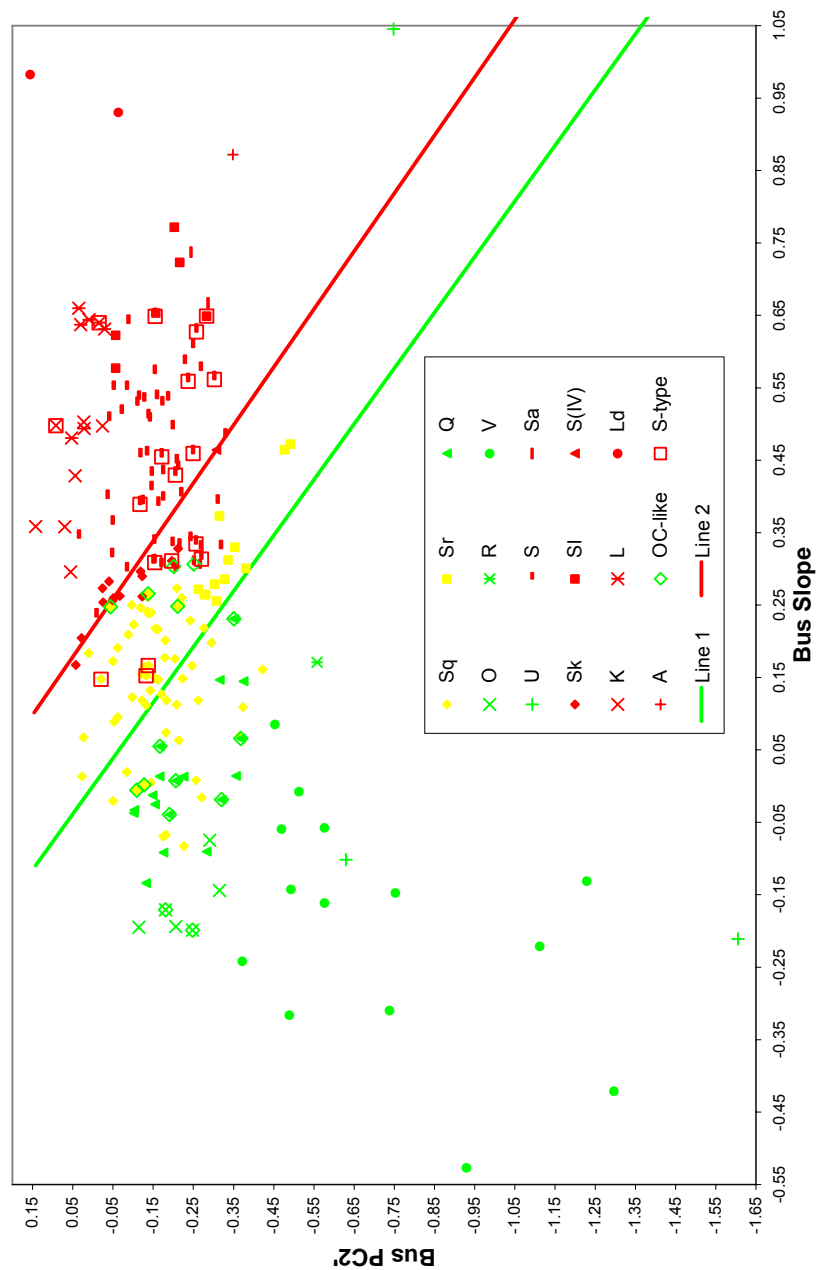


Figure 5.2. Principal Component plot for NEAs in Binzel et al. (2004a) that they classify as Sq, Sr, Q, O, R, V, U, S, Sa, Sk, Sl, S(IV), K, L, Ld, and A types. This subset of their dataset was chosen since these taxonomic types clearly show a 1- μ m absorption. This plot allows the classification of OC-like and S-type NEAs in their data, forming the basis for the first method of classification for their data. The delimitation for the uncertain region shown in Figure 5.1 is overlaid on this plot. NEAs to the left of the green line are classified as OC-like. Those to the right of the red line are S-type.

plotted with red colors) and OC-likes (primarily composed of the Q, O, R, V, U classes which are plotted with green colors.) It should be noted that only 214 of the 310 NEAs from the Binzel et al. (2004a) database are used since only asteroids that have a demonstrable 1- μm absorption are plotted. The uncertain group in the boundary between the two lines is populated primarily by Sq and Sr types which are colored yellow. NEAs in this region are not assigned to either the OC-like group or S-type group. It is likely the region of overlap stems from the peculiarities of Bus's classification scheme (cf. Section 3.3 and Appendix B), whereby PC2' is not well correlated with the 1- μm absorption and Bus includes the 1- μm absorption in his Slope measurements.

A subset of NEA spectra from the Binzel et al. (2004a) database was used to double check this classification method. Most of the reflectance spectra in this data set only extend to 0.92- μm and do not resolve the band minimum of the 1- μm absorption. However some spectra were taken which extend to 1.6- μm . These spectra were measured using our slope and band depth parameterization method. Good agreement was found when these objects were classified according to the method used earlier. Only one of the 12 NEAs classified as OC-like in the method outlined in this section would have been classified as an S-type in the method of classification described in Chapter 3. Similarly, only one of the 8 objects classified as S-type in the method of classifying Binzel's data in this section would have been classified as OC-like in my original classification method.

Having come to a reasonable transformation between the Binzel/Bus classifications and my own the Binzel et al. (2004a) database was investigated for trends found in our NEA data. Figure 5.3 shows S-type and OC-like NEAs from Binzel et al.'s

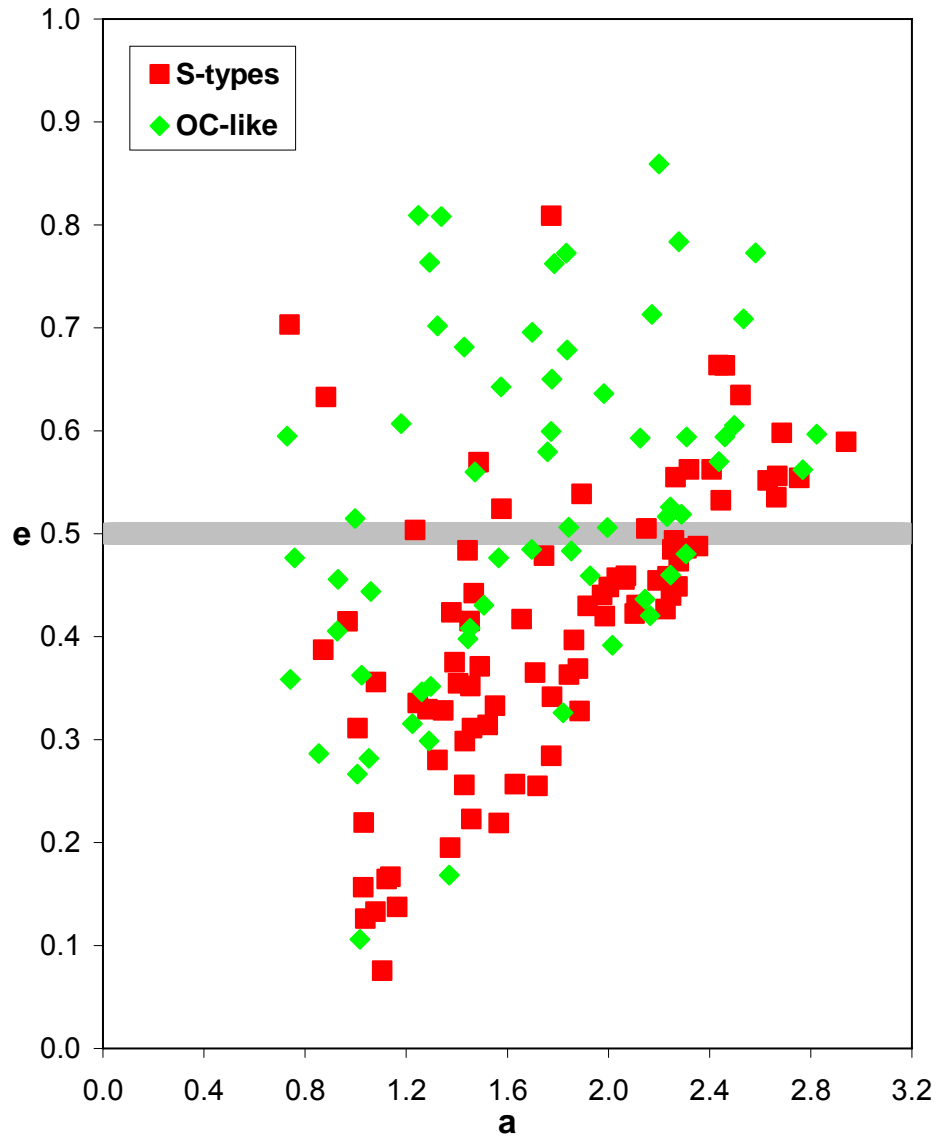


Figure 5.3. Plot of eccentricity vs. semi-major axis for S-type (red squares) and OC-like (green diamonds) NEAs in Binzel et al. (2004a). These classifications are based on the first classification method of their objects that involved NEAs in common between both of our data sets. OC-like objects tend to reside in high-eccentricity orbits ($e > 0.5$) while S-type objects tend to be in low-eccentricity orbits ($e < 0.5$).

(2004a) database in eccentricity space. As in Figure 4.2 there is a noticeable difference in the distribution of these two groups of asteroids with a strong trend toward OC-like NEAs in high eccentricity orbits.

Figure 5.4 shows S-type and OC-like NEAs in (q,Q)-space. While there are some OC-like Atens and Amors, there is a noticeable difference in the distribution of the S-type and OC-like groups of NEAs with a trend toward OC-like objects in main-belt crossing orbits, particularly in the box of Apollo-class objects that enter the main-belt. The scatter however is worse than for our data. A portion of this may be attributed to their choice of Principal Components and the difficulty in transferring their classification scheme to my own.

The same hypothesis tests that were used to check for statistically significant differences in the eccentricity and (q,Q) distributions of our OC-like versus S-type NEAs were applied to the OC-like and S-type objects in the Binzel et al. (2004a) data set (cf. Chapter 4). For the χ^2 -tests, the same bin delimitations in eccentricity and (q,Q) space were used. Unlike our NEA data set, the sizes of the OC-like and S-type samples in Binzel's data set were large enough to support the use of one additional test, the two-dimensional Kolmogorov-Smirnov (K-S) test (Press et al., 2001). This was used to test the difference between the (q,Q) distributions for the OC-like versus S-type NEAs. The upper half of Table 5.1 summarizes the results of these tests. (The lower half of this table summarizes the results for an alternate classification method of the Binzel et al. (2004a) data, summarized in Section 5.3.) The confidence levels for all of these tests were above

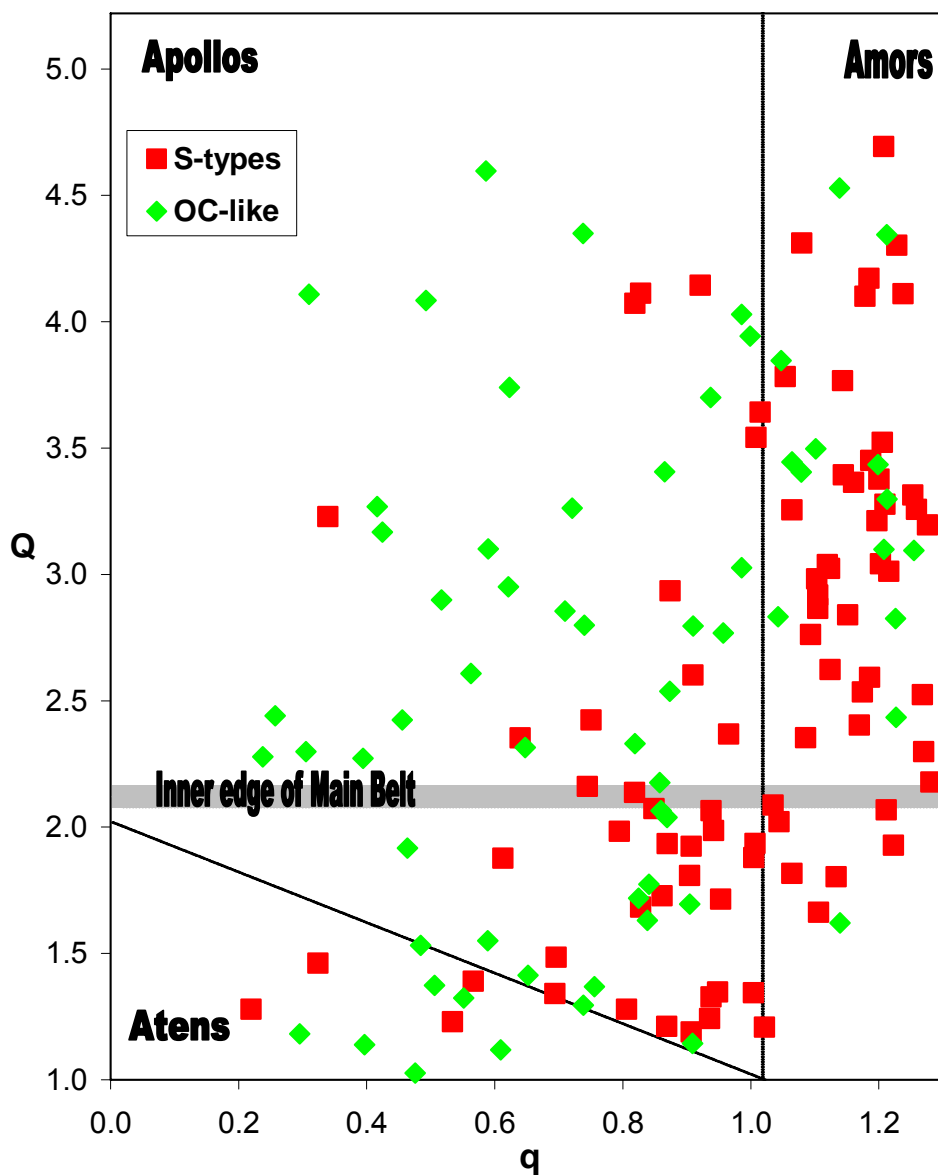


Figure 5.4. Plot of aphelion distance vs. perihelion distance for S-type and OC-like NEAs, determined by the first method of classifying objects in Binzel et al. (2004a). The shaded band and slanted and vertical lines delimit the same regions as described in Figure 4.3. OC-like NEAs tend to reside in Apollo-class orbits which have aphelia in the asteroid main-belt.

Table 5.1 - Statistical Results from the Binzel et al. (2004a) Data

Classification Method ^a	Statistical Test ^b	Distribution or Quantity Tested ^c	Confidence Level (%)
1st (Overlap)	χ^2	e-distribution	99.902
"	χ^2	(q,Q)-distribution	99.977
"	K-S (1-dim.)	e-distribution	99.949
"	K-S (2-dim.)	(q,Q)-distribution	99.965
"	Student t	mean e	99.998
2nd (Meteorites)	χ^2	e-distribution	99.692
"	χ^2	(q,Q)-distribution	99.943
"	K-S (1-dim.)	e-distribution	99.835
"	K-S (2-dim.)	(q,Q)-distribution	99.992
"	Student t	mean e	99.998

^a The first method of classifying the Binzel et al. (2004a) NEAs that uses overlapping observations, described in Section 5.1, is denoted by "1st (Overlap)". The second method of classifying their NEAs that uses meteorite data, described in Section 5.3, is denoted by "2nd (Meteorites)".

^b The χ^2 test, Kolmogorov-Smirnov (K-S) tests for one dimensional (1-dim.) and two dimensional (2-dim.) distributions, and the Student t-Test are from Press et al. (2001).

^c Hypothesis tests are performed on the OC-like and S-type data, looking for differences between their eccentricity distributions (e-distribution), two-dimensional (q,Q)-distributions (where q = perihelion distance and Q = aphelion distance), and mean eccentricities (mean e).

99%, strongly indicating that the OC-like and S-type NEAs have different eccentricity and (q,Q) distributions.

Thus, using this delimitation of $(\text{Slope}, \text{PC2}')$ -space to classify OC-like and S-type NEAs in Binzel et al. (2004a), essentially the same results as in Chapter 4 are evident: for the subset of OC-like and S-type NEAs, Apollo class NEAs in highly eccentric orbits which cross the asteroid main-belt tend to be OC-like while NEAs in other types of orbits tend to be S-types. The following set of conclusions from the observations in Chapter 4 still apply, namely:

1. Objects with spectra close to ordinary chondrites are quite abundant (23 OC-like and 19 S-types in our dataset) among the NEAs.
2. These OC-likes occupy high eccentricity orbits that intersect the asteroid main belt.
3. There appears to be a continuum of spectral types between OC-like and S-type NEAs in our data.

It is noted however that the scatter is worse than for our data.

5.2 - Tabular form of asteroid classification comparison and statistical check

The difficulty of transferring between my classification scheme and Binzel et al.'s (2004a) (Bus's) is illustrated in a different form in Table 5.2. This table again uses NEAs that were observed both by us and Binzel et al. (2004a). My classifications are shown in the fourth column of this table. In column 5 the taxonomic classifications of Binzel et al. (2004a) are listed. For most NEAs there is good agreement between the two research

Table 5.2 - Comparison of Our Classifications with those of Binzel et al.'s (2004a)

<u>Asteroid</u>		Provisional	Our	Binzel et al.
<u>Number</u>	<u>Name</u>	<u>Designation</u>	<u>Taxonomic Group</u>	<u>Taxonomic Classification</u>
1862	Apollo	1932 HA	OC-like	Q
2102	Tantalus	1975 YA	OC-like	Q
4341	Poseidon	1987 KF	OC-like	O
6489	Golevka	1991 JX	OC-like	Q
8176	1991 WA	1991 WA	OC-like	Q
8201	1994 AH2	1994 AH2	OC-like	O
10563	Izhdubar	1993 WD	OC-like	Q
		1997 US9	OC-like	Q
1685	Toro	1948 OA	OC-like	S ²
19356	1997 GH3	1997 GH3	OC-like	S ²
2063	Bacchus	1977 HB	OC-like	Sq ¹
2201	Oljato	1947 XC	OC-like	Sq ¹
4183	Cuno	1959 LM	OC-like	Sq ¹
5587	1990 SB	1990 SB	OC-like	Sq ¹
20255	1998 FX2	1998 FX2	OC-like	Sq ¹
1566	Icarus	1949 MA	OC-like	
4953	1990 MU	1990 MU	OC-like	
6037	1988 EG	1988 EG	OC-like	
20236	1998 BZ7	1998 BZ7	OC-like	
		1996 JA1	OC-like	
		1997 GD32	OC-like	
		1998 MS2	OC-like	
		2004 LC2	OC-like	
433	Eros	1898 DQ	S-type	S
1036	Ganymed	1924 TD	S-type	S
1620	Geographos	1951 RA	S-type	S
1627	Ivar	1929 SH	S-type	S
1866	Sisyphus	1972 XA	S-type	S
1980	Tezcatlipoca	1950 LA	S-type	Sl
3122	Florence	1981 ET3	S-type	S
4954	Eric	1990 SQ	S-type	S
7482	1994 PC1	1994 PC1	S-type	S
7822	1991 CS	1991 CS	S-type	S
7977	1977 QQ5	1977 QQ5	S-type	S
13651	1997 BR	1997 BR	S-type	S
35107	1991 VH	1991 VH	S-type	Sk
3199	Nefertiti	1982 RA	S-type	Sq ¹
7358	Oze	1995 YA3	S-type	Sq ¹
		1997 UH9	S-type	Sq ¹
1943	Anteros	1973 EC	S-type	L ³
11066	Sigurd	1992 CC1	S-type	K ³
		1995 CR	S-type	
		1998 HT31	BOC-like	C: ⁴
5836	1993 MF	1993 MF	BOC-like	S
6053	1993 BW3	1993 BW3	R-type	Sq ¹
		1998 HE3	R-type	
3103	Eger	1982 BB	Other	Xe
3200	Phaethon	1983 TB	Other	B
3671	Dionysus	1984 KD	Other	Cb
5751	Zao	1992 AC	Other	X
7753	1988 XB	1988 XB	Other	B
85490	1997 SE5	1997 SE5	Other	T
7092	Cadmus	1992 LC	Other	
		1994 ES1	Other	
		1998 ME3	Other	

Notes: ¹ There are a significant number of NEAs which were classified as Sq's in Binzel et al. (2004a) that we classified as OC-like. Vice-versa, there are several NEAs which were classified as Sq's in Binzel et al. (2004a) that we classified as S-types.

² Our spectra of these NEAs were fairly noisy and showed possible rotational variation so my classifications of these two objects are marginal.

³ Referring to Bus et al. (2002), L, Ld, and K types ought to be assigned to the S category in our taxonomic group.

⁴ The colon after the C in Binzel et al.'s (2004a) classification indicates a questionable classification. Our spectrum of 1998 HT31 clearly shows a 1- μ m absorption, eliminating a C-type classification.

groups (i.e., our OC-likes are classified mainly as Q by Binzel and our S-types are classified mainly as S by Binzel). Several points need additional clarification.

1. The major problem occurs for the Sq's which are in the region of uncertainty. In my classification scheme the Sq's were divided roughly evenly between the OC-like and S-type groups. It appears that the Bus Principal Component method cannot make a clean distinction between the latter two groups.

2. (1685) Toro and (19356) 1997 GH3 are classified as OC-like asteroids by my method but as S class asteroids by Binzel et al. (2004a). McFadden et al. (1984) noted possible rotational variation for (1685) Toro. Our observed spectra of these two objects clearly showed relatively deep 1- μ m absorptions but also gave indications of possible rotational variations over several nights which may explain the discrepancy between the two methods of classification.

3. (1943) Anteros and (11066) Sigurd received an L and K classification in Binzel et al. (2004a), respectively. Bus et al. (2002) points out that these classes of objects would fall within Tholen's S taxonomic class and hence my grouping them as S-types is consistent with those classifications.

4. The colon following the C classification of 1998 HT31 by Binzel et al. (2004a) indicates a questionable assignment. Our spectra show a shallow 1- μ m absorption, clearly ruling out a C classification.

It is also useful to check whether the **distribution fractions** of taxonomic groups are in rough accord between Binzel et al.'s (2004a) data and our data. This is done in Table 5.3. While the number of overlapping NEA observations (41) could desirably be

**Table 5.3 - Comparison of NEA statistics in various groups
for our data and our classification of those of Binzel et al. (2004a).**

Preliminary Taxonomic Groups for Binzel Data	Binzel et al.'s (2004a) taxonomic classes included in this group	Number and Percentage of NEAs in this group			
		Binzel et al. (2004a)		Our Data	
		Number	Percent	Number	Percent
<i>OC</i>	Sq	19	6.5		
<i>OC</i>	Q	17	5.8		
<i>OC</i>	O	6	2.1		
<i>OC</i>	R	1	0.3		
<i>OC</i>	V	14	4.8		
<i>OC</i>	U	2	0.7		
OC		59	20.3	10	24.4
<i>Uncertain</i>	Sq	42	14.4		
<i>Uncertain</i>	Sr	9	3.1		
<i>Uncertain</i>	Q	1	0.3		
<i>Uncertain</i>	S	8	2.7		
<i>Uncertain</i>	Sk	3	1.0		
Uncertain		63	21.6	12	29.3
<i>S</i>	Sr	3	1.0		
<i>S</i>	U	1	0.3		
<i>S</i>	S	52	17.9		
<i>S</i>	Sa	2	0.7		
<i>S</i>	Sk	10	3.4		
<i>S</i>	Sl	6	2.1		
<i>S</i>	S(IV)	1	0.3		
<i>S</i>	K:	7	2.4		
<i>S</i>	L	7	2.4		
<i>S</i>	Ld	2	0.7		
<i>S</i>	A	1	0.3		
S		92	31.6	11	26.8
<i>Other</i>	B	5	1.7		
<i>Other</i>	Cb	3	1.0		
<i>Other</i>	C	12	4.1		
<i>Other</i>	Cg	1	0.3		
<i>Other</i>	Ch	1	0.3		
<i>Other</i>	Xc	6	2.1		
<i>Other</i>	Xk	9	3.1		
<i>Other</i>	X	29	10.0		
<i>Other</i>	Xe	2	0.7		
<i>Other</i>	T	5	1.7		
<i>Other</i>	D	4	1.4		
Other		77	26.5	6	14.6
<i>Our R-types</i>	Not Applicable			1	2.4
<i>Our BOC-likes</i>	Not Applicable			1	2.4
All Types	All asteroids with PCA values	291	100.0	41	100.0

Note: Some objects in the "Other" taxonomic group, in particular those in the X complex in the Bus taxonomy (Bus and Binzel, 2002b), really show a 1- μ m absorption. They are inconsistent with the Tholen X class which clearly show no spectral curvature longward of $\sim 4500 \text{ \AA}$ (Tholen and Barucci, 1989). We would have classified many of these as S-types.

higher, it is large enough that the rough percentage of our objects in each of the OC-like, S-type, and Other taxonomic groups along with those that fall in the Uncertain region should agree with Binzel et al.'s (2004a) database which offers considerably better statistics.

In the analysis in Chapter 4 the Sq/uncertain classification was not used. For purposes of the statistical comparison in Table 5.3 some of our asteroids were put into this overlapping region by using the boundaries in Bus's Principal Component space between the OC-like and S-type taxonomic groups (Figure 5.1 & Figure 5.2).

The results of Table 5.3 can now be summarized. Considering the different methodology used Binzel shows roughly 20% OC-likes, 22% fall in the uncertain region, 32% S-types and 26% Others. Our data shows 24% OC-likes, 29% in the uncertain region, 27% S-types and 15% Others. While the general agreement of the population fractions is quite good some discrepancy exists for the "Others". Because there are only six NEAs from our database in this group the statistics for these objects are more uncertain. Secondly, some objects in the X complex in the Bus taxonomy (Bus and Binzel, 2002b) show a downturn near 0.9- μm . This is inconsistent with the Tholen X class which shows no spectral curvature longward of $\sim 4500 \text{ \AA}$ (Tholen and Barucci, 1989). It should also be noted that NEAs classified as "Other" are not considered in Figures 5.1 and 5.2. Some of these objects in Binzel's data set appear to have a 1- μm absorption and could have been grouped into the S-type and Uncertain categories, improving the agreement between our two datasets.

For the purpose of this initial analysis of Binzel et al's (2004) data an attempt to classify any of their objects as BOC-like or R-type was not made. Very few of our own objects received these classifications (4 out of 55) and only two of these were observed by both Binzel's group and our own. Therefore, excluding these rare taxonomic groups from this preliminary analysis does not significantly affect the statistical results. One clearly cannot expect perfect agreement between two diverse data sets, and so the agreement between the two datasets in Tables 5.2 and 5.3 is quite gratifying.

5.3 - Classifying OC-like and S-type NEAs in Binzel et al. (2004a) using Principal Component Analysis by Bus (1999) of Gaffey (1976) meteorite data

Fortunately Bus (1999) carried out a Principal Component Analysis on a set of 78 meteorite spectra from Gaffey (1976) using the same methodology and principal components as for the NEAs in Binzel et al. (2004a). Of these 78 meteorites, 31 were ordinary chondrites. This allowed me to use an approach analogous to the classification method for our own data to determine which of the NEAs in Binzel et al. (2004a) correspond to OC-like and S-type asteroids.

In Figure 5.5 a plot of PC2' versus Slope for 27 of the OCs (green diamonds) is shown. (The four very dark black ordinary chondrites that have been spectrally altered (Britt and Pieters, 1991) are left out.) Also shown in Figure 5.5 are 11 achondrites from the 78 meteorites Bus analyzed (blue triangles). A more detailed discussion of these is given in section 5.4. Figure 5.5 was utilized to define a region in (Slope,PC2')-space which is occupied by the ordinary chondrite meteorites. On the figure this section is

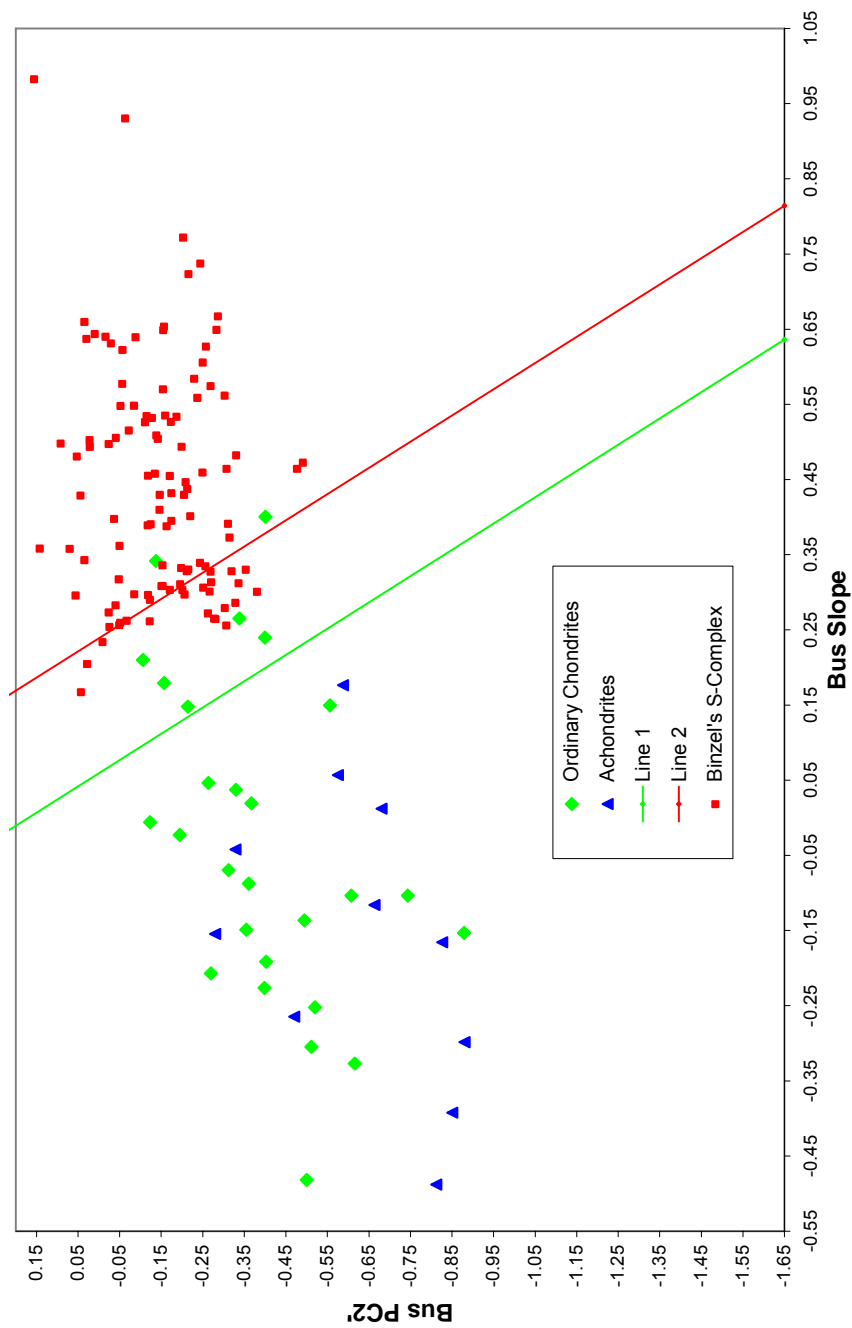


Figure 5.5. Principal Component plot for OCs (green diamonds) and achondrites (blue triangles) from Gaffey's (1976) meteorite data. The Principal Component Analysis was performed by Bus (1999). The set of NEAs in Binzel's "S-complex" (Binzel et al., 2004a) are shown with red squares. The green and red lines encompass the outliers in the OC data and define a "region of uncertainty" for the classification of OC-like and S-type NEAs in the Binzel et al. (2004a) data set.

given by the region to the left of the green line. The green and red lines were used to indicate a region of uncertain classification in the Bus (Slope,PC2') space analogous to Figures 5.1 and 5.2. The chosen lines are clearly somewhat arbitrary but are very reasonable. The slope of the lines are roughly perpendicular to the general trend of the OC meteorites using the Bus PC2' and Slope parameterization. Unfortunately, Principal Component Analysis in the Bus taxonomy is not available for Gaffey's S-class asteroids, so these objects which are expected to fill the upper right quadrant of Figure 5.5 could not be plotted. In their place were plotted the "S-complex" NEAs (red squares), defined in Binzel et al. (2004a).

As was done in the last section the delimitations of Figure 5.5 can be transferred to determine which NEAs in the Binzel et al. (2004a) data set have OC-like spectra. This is done in Figure 5.6 which shows a plot of PC2' versus Slope for the objects classified as OC-like (green diamonds) and those classified as S-type (red squares) from Binzel et al. (2004a) along with those in the uncertain region (yellow triangles). Those which have OC-like spectra are to the left of the boundary lines of Figure 5.5 while those that have S-type spectra are to the right of the boundary lines.

In Figure 5.6 the NEAs are divided into reasonably certain ordinary chondrite meteorite types, reasonably certain S-types and overlapping uncertain classifications. This allows plots (Figures 5.7 and 5.8) similar to Figure 4.2 and Figure 5.3 in eccentricity space and Figure 4.3 and Figure 5.4 in (q,Q) space to be produced. Again it is noted that the same trends as seen in Figure 5.3 and Figure 5.4 appear in these two figures. As would be expected for a population intermediate between the two, NEAs in the Uncertain

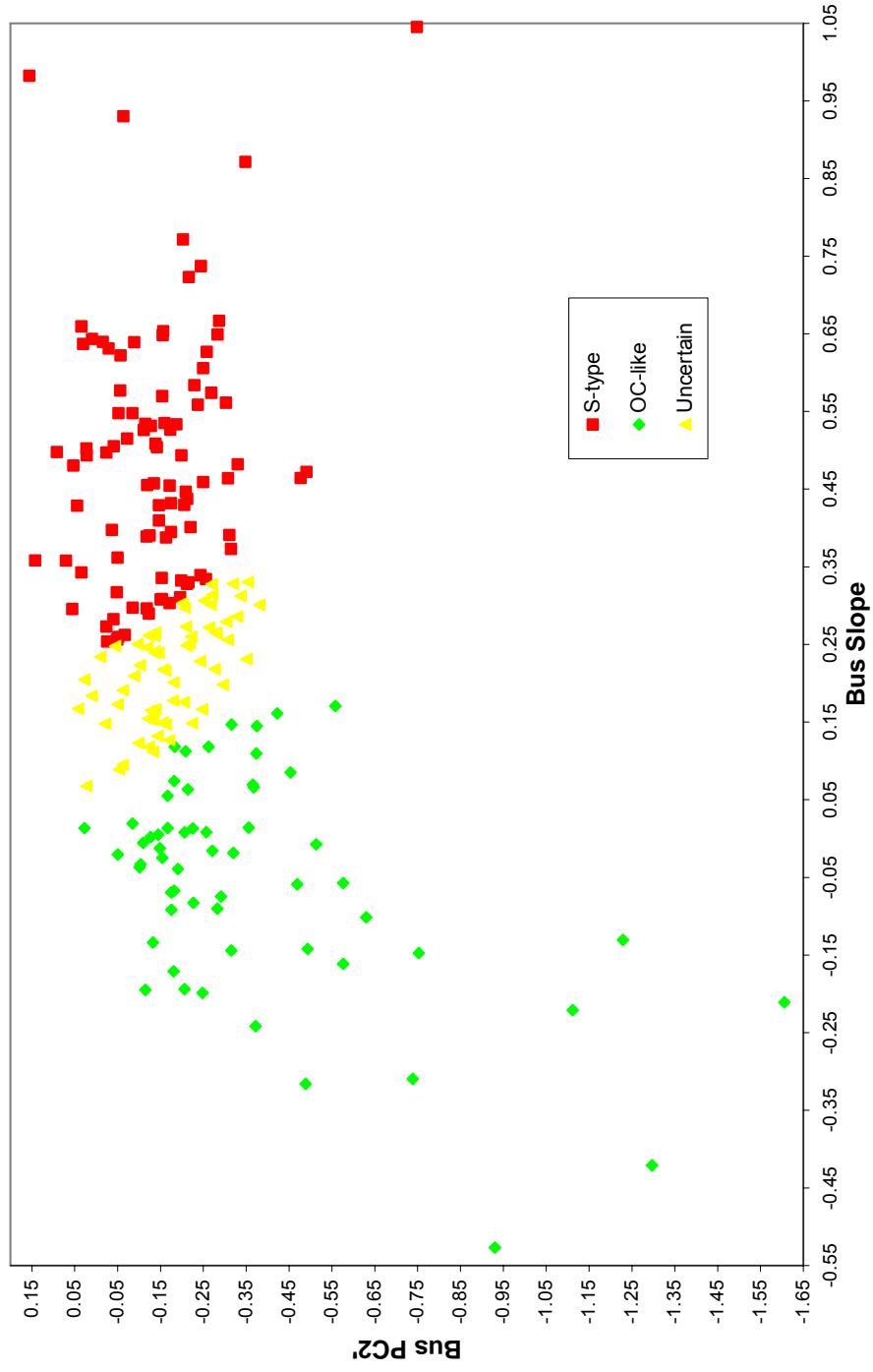


Figure 5.6. Principal Component plot of the same set of NEAs in Binzel et al. (2004a) that are shown in Figure 4.2. This plot provides a second, independent method of classifying OC-like and S-type NEAs in their data. Their NEAs are classified as OC-like (green diamonds), S-type (red squares), and Uncertain (yellow triangles) using Gaffey's (1976) meteorite data.

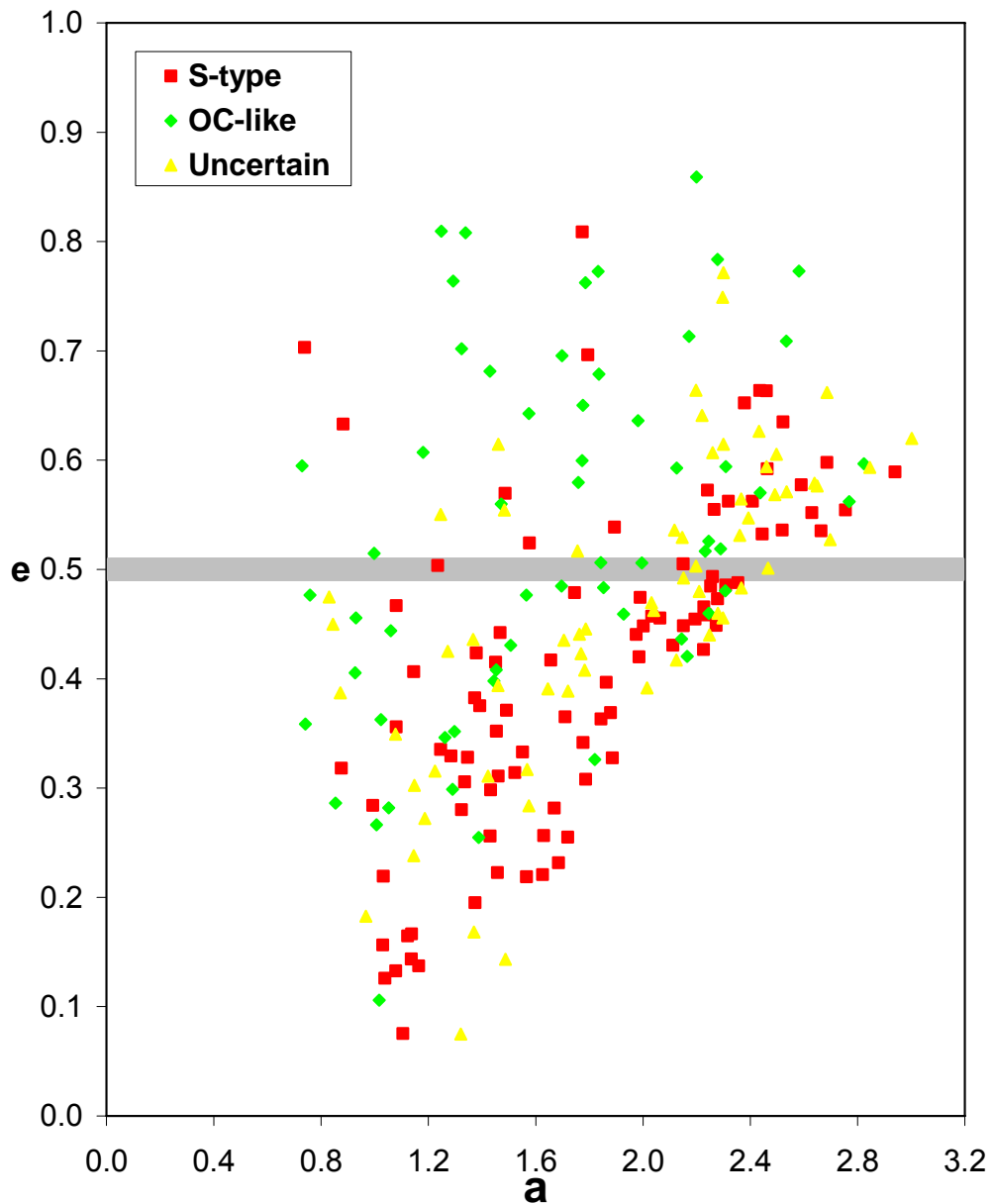


Figure 5.7. Eccentricity plot for NEAs in Binzel et al. (2004a). S-type (red squares), OC-like (green diamonds) and Uncertain types (yellow diamonds) were determined by the second method of classifying their objects involving Gaffey's (1976) meteorite data. This plot shows the same trend for S-type and OC-like objects as Figure 5.3.

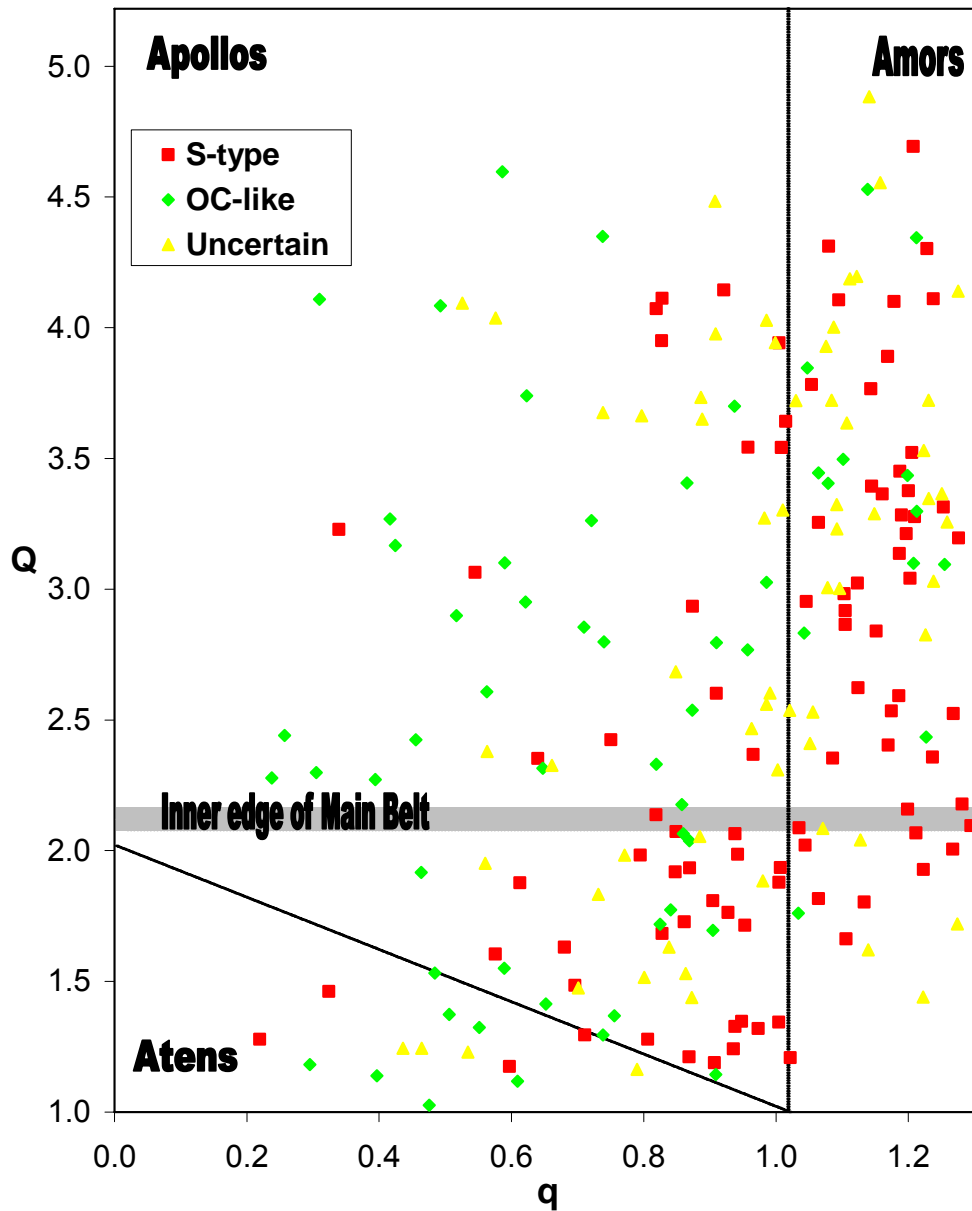


Figure 5.8. Plot of aphelion distance vs. perihelion distance for S-type (red squares), OC-like (green diamonds) and Uncertain (yellow diamonds) NEAs, determined by the second method of classifying objects in Binzel et al. (2004a). This plot shows the same trend for S-type and OC-like objects as Figure 5.4.

region bridge the gap between the distributions of OC-like and S-types in Figure 5.7 and Figure 5.8.

The hypothesis tests used in earlier sections of this dissertation were applied to this alternate method of classifying OC-like and S-type objects in the Binzel et al. (2004a) data set (cf. Chapter 4 and Section 5.1). These were used to test the difference between the eccentricity and (q,Q) distributions for the OC-like versus S-type NEAs. The lower half of Table 5.1 summarizes the results of these tests. As was the case for the classification method used in Section 5.1, the confidence levels for all of these tests were above 99%, strongly indicating that the OC-like and S-type NEAs have different eccentricity and (q,Q) distributions.

This third method of looking at the relationship of OC-like NEAs with eccentricity and perihelion and aphelion distance leads again to the same conclusions as mentioned in Chapter 4 and Section 5.1.

5.4 - The achondrite ambiguity

In addition to the 27 ordinary chondrites (green diamonds) 11 achondrites (blue triangles) are plotted in Figure 5.5. (Note that 6 additional achondrites in Bus (1999) have slope values less than -0.55 and would plot beyond the left boundary of the figure.) The 11 achondrites plotted cannot be distinguished from ordinary chondrite meteorites in this diagram. However, using Gaffey's meteorite spectra they can be separated in a plot of PC3' versus Slope which is done in Figure 5.9. This figure unfortunately can not be used in this analysis since our spectral data does not encompass the UV absorption and

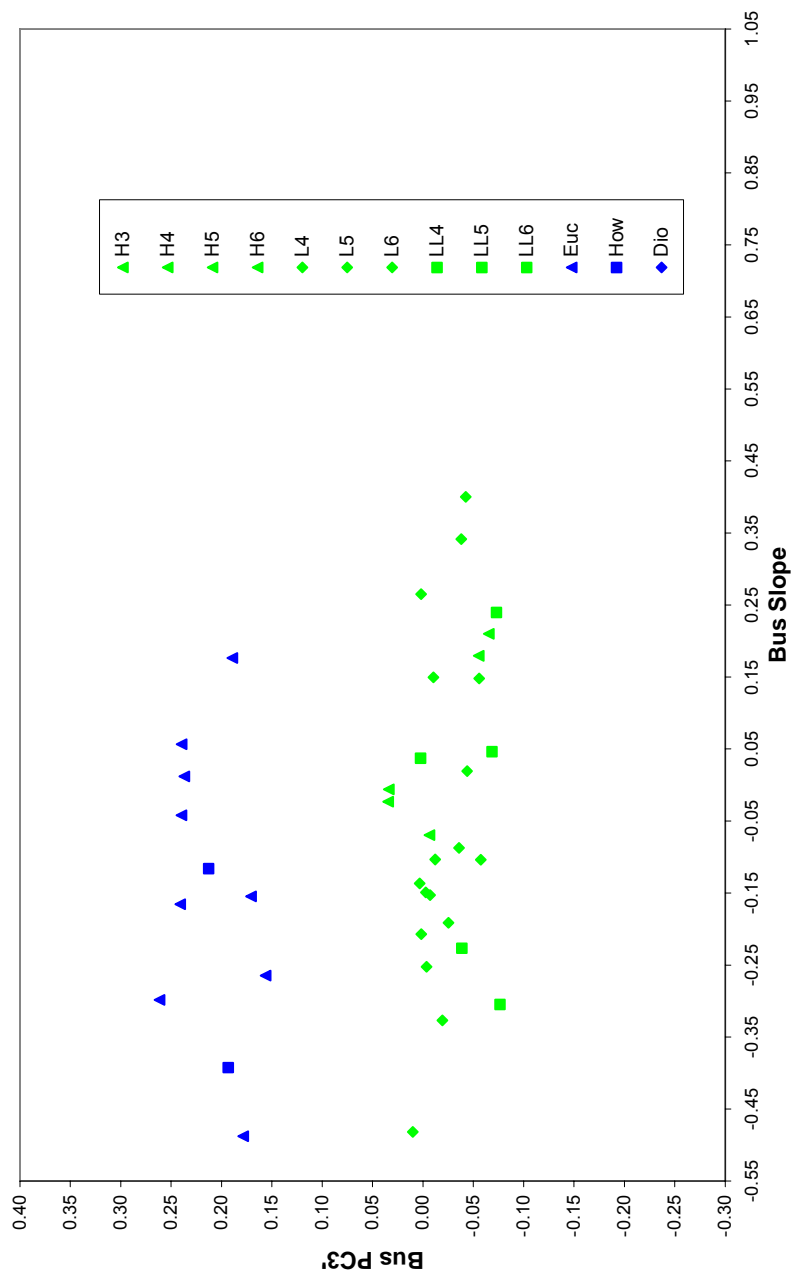


Figure 5.9. Principal Component plot of ordinary chondrites (green symbols) and achondrites (blue symbols) from Gaffey's (1976) meteorite data. Compare this plot with the PC2' vs. Slope plot in Figure 5.5. The Third Principal Component, PC3', is required to separate the ordinary chondrites from the achondrite class of meteorites which have been associated with V-class asteroids.

thus there is no spectral parameter equivalent to PC3' in my classification method. (Bus and Binzel (2002b) state that PC3' is best correlated with a UV absorption.) While Binzel et al.'s (2004a) database goes to somewhat shorter wavelength (4400 Å) they are only partially able to observe the UV absorption for asteroids. This allowed them to marginally separate some “achondrite-like” (i.e., V type) asteroids. They found a few V types, ~5%, in their NEA spectroscopic survey. If this is generally the case one would expect to find 2 or maybe 3 such NEAs among the OC-like objects in our data set. This would not significantly affect the statistical results of the analyses in this dissertation.

CHAPTER 6

EXTINCT COMETS AMONG THE NEAR-EARTH ASTEROIDS

In this chapter NEAs labeled as Others (i.e., those objects which show featureless reflectance spectra with neutral or red slopes) are discussed. Three types of physical objects fit this category; extinct comets, iron meteorites, and enstatite chondrite meteorites. Two types of meteorites that have featureless flat or slightly red spectra are iron meteorites and enstatite chondrites (Cloutis et al., 1990). They both likely formed in the inner part of the solar system (Bottke et al., 2006; Keil, 1989) where temperatures were too high for their parent bodies to retain volatiles. Enstatite chondrites are primarily composed of enstatite (MgSiO_3), iron, nickel and other minerals that formed under highly reducing conditions (Keil, 1989) and exhibit no 1- μm absorption because of their lack of transition series elements (Cloutis et al., 1990).

With each passage through the inner solar system a comet loses volatiles due to insolation. After numerous orbits a comet may produce a thick surface crust so that it is no longer active. Such objects are termed Extinct Comets. If observed through a telescope an Extinct Comet would appear asteroidal. At least one NEA has been observed to be in transition between an active comet and an Extinct Comet. When it was first discovered (4015) Wilson-Harrington was identified as a comet (Cunningham, 1950). It was subsequently lost and then re-discovered 30 years later and identified as an asteroid (Helin, 1979), its linkage to its cometary origin made some time later (Bowell,

1992; Marsden, 1992). No cometary activity has been observed since 1949 and it is considered to be an Amor class NEA.

In the following sections an orbital trend analysis for NEAs that exhibit no 1- μm absorption is carried out. It was found that such objects tend to cluster in low inclination orbits (Section 6.1). An attempt was made to estimate what fraction of these objects can be associated with iron and enstatite chondrite meteorites and what fraction could be Extinct Comets (Section 6.2). In section 6.3 plausible arguments are presented that explain why Extinct Comets concentrate in low inclination orbits. The results from this chapter are summarized in Section 6.4.

6.1 - Trends in orbital inclination for Extinct Comet Candidates in our NEA dataset and Binzel et al.'s (2004a)

Observations of comet nuclei, taken at large heliocentric distances when the comet is not active, give an idea of the spectra one would expect for Extinct Comet Candidates among the NEAs. Over our wavelength range these spectra are essentially featureless with spectral slopes ranging from slightly blue ($\sim 3\%/1000 \text{ \AA}$) to very red ($\sim 20\%/1000 \text{ \AA}$) (Luu, 1993). Spacecraft observations from 1.3- μm to 2.6- μm of 19P/Borrelly from Deep Space 1 (Soderblom et al., 2002) indicate this trend persists in the infrared. Objects exhibiting featureless, slightly blue to red spectra would fall within our "Other" classification which is discussed in Chapter 3. Examples of our observed spectra for such objects with no 1- μm absorption are shown in Figure 3.6.

When our data of these “Other” objects were compared to their orbital inclination a trend appeared. Figure 6.1 shows the inclination distribution for NEAs in our dataset that do not have a 1- μm absorption. There seems to be a preponderance of objects having low inclinations. As shown in Figure 6.2 the inclination distribution is broader for objects that have a 1- μm absorption. Due to our small sample of 9 objects which show no 1- μm absorption, this is not a statistically significant result. Hence, an analysis of a larger NEA spectral dataset was required to see whether this trend was real.

In order to make a similar plot using the Binzel et al. (2004a) dataset it was first necessary to determine which of their NEAs complied with my "Other" classification. In Chapter 3 and Appendix B problems are cited regarding the difficulty in correlating spectral features with Principal Component values in Binzel et al. (2004a). For objects that do not have a 1- μm absorption, this can more easily be resolved. The spectral plots for their NEAs (Xu et al., 1995; Binzel et al., 2001a; Binzel et al., 2001b; Binzel et al., 2004a; Binzel et al., 2004b; Binzel et al., 2004c) were checked visually to see which objects had 1- μm absorptions. The presence of a 1- μm absorption was then correlated with Principal Component values. Figure 6.3 shows the results of this procedure. Objects with values of $\text{PC2}' > 0.15$ have essentially no 1- μm absorption. This line therefore forms a natural break in the data, with objects above this line not having any 1- μm absorption while objects with $\text{PC2}' < 0.15$ exhibiting a 1- μm absorption.

Two figures similar to Figures 6.1 and 6.2 were then constructed. Objects that have no 1- μm absorption (i.e., $\text{PC2}' > 0.15$) are depicted in Figure 6.4 while in Figure 6.5 objects that show a 1- μm absorption (i.e., $\text{PC2}' < 0.15$) are plotted. The same trend that

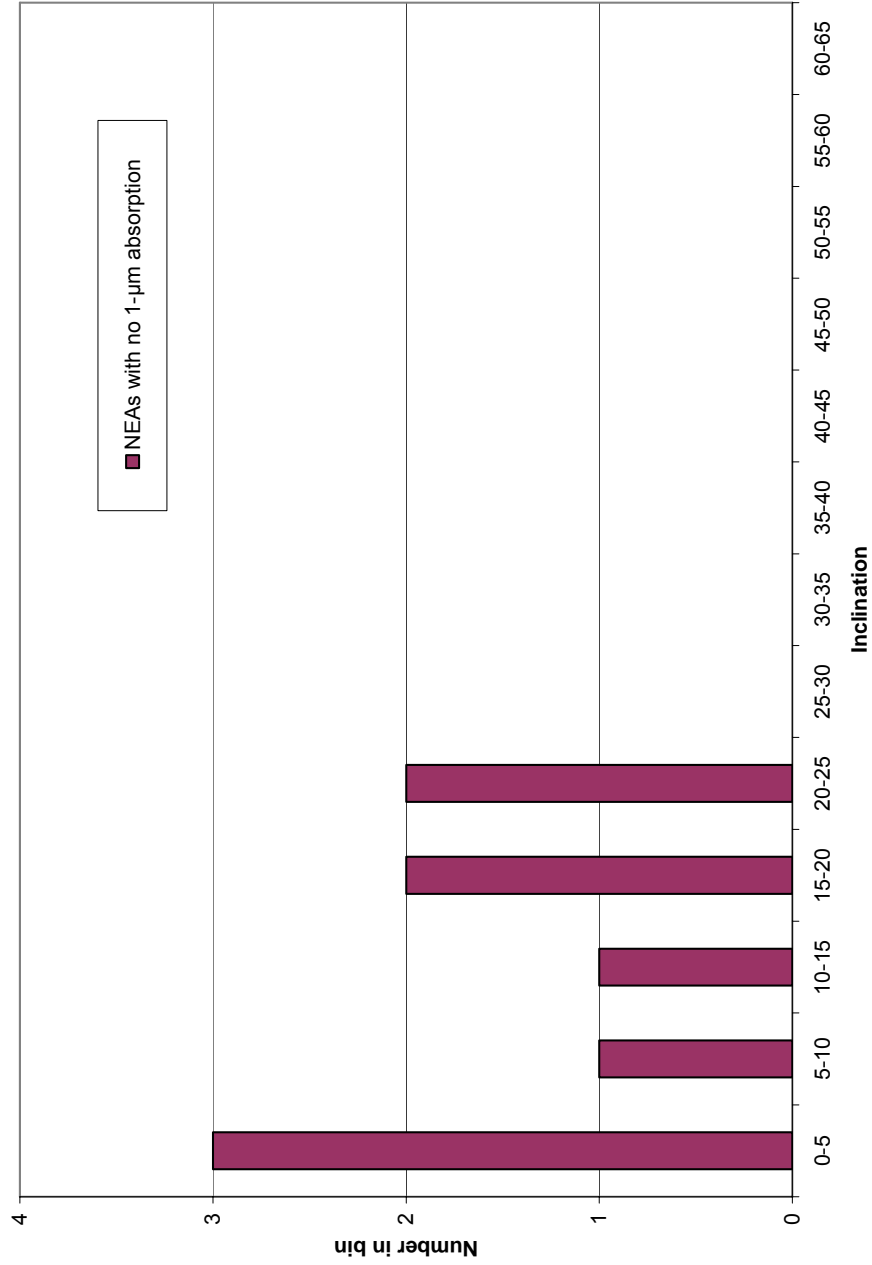


Figure 6.1. Inclination distribution for our NEAs which do not have a 1- μ m absorption. All of these objects are below an inclination of 25°. There appears to be an increased abundance of such objects in the 0° - 5° inclination bin, though due to the small number of such NEAs in our sample meaningful statistics can not be derived.

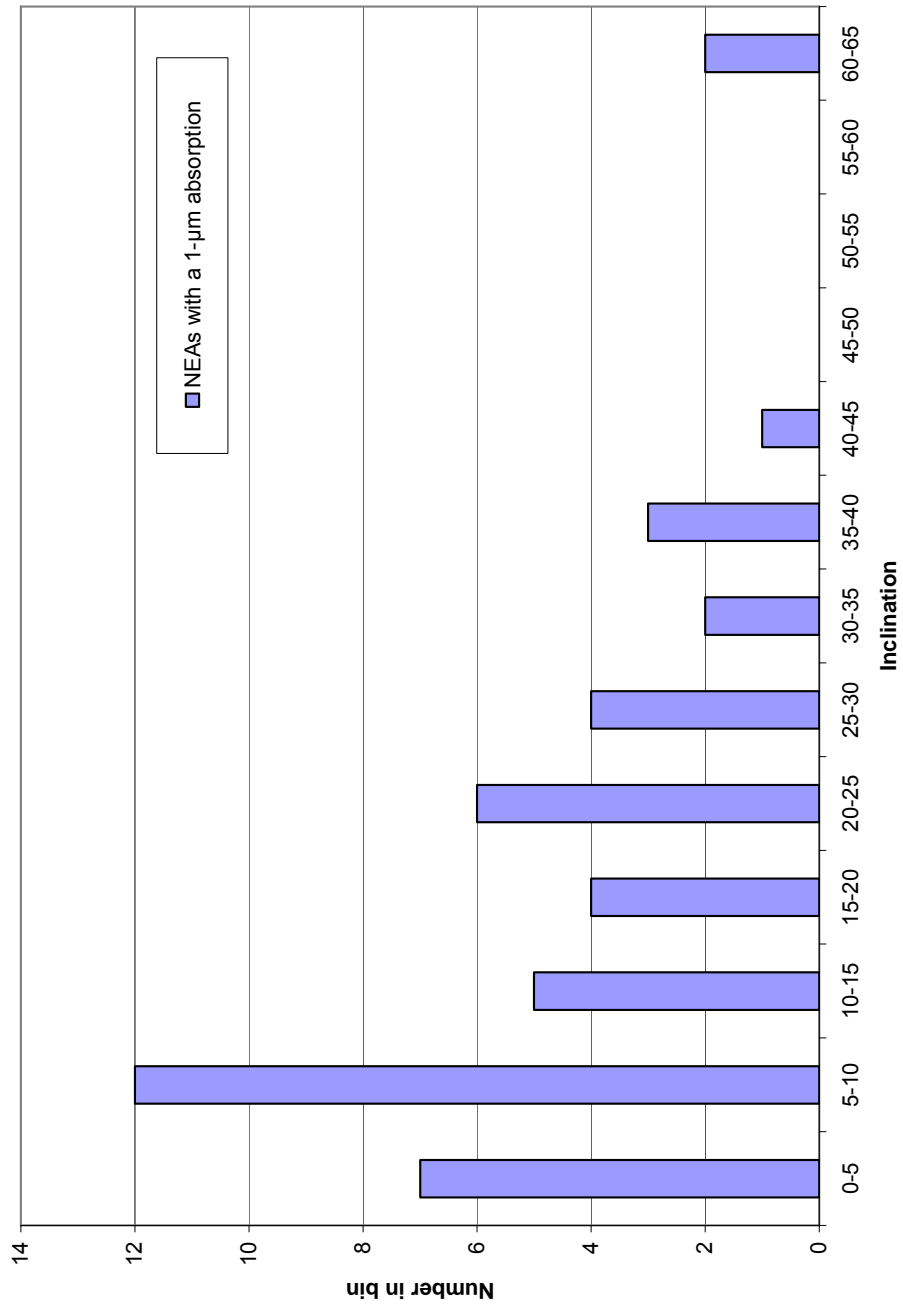


Figure 6.2. Inclination distribution for our NEAs which have a 1-μm absorption. Compare with Figure 6.1. Such objects have a broader inclination distribution than objects that do not have a 1-μm absorption.

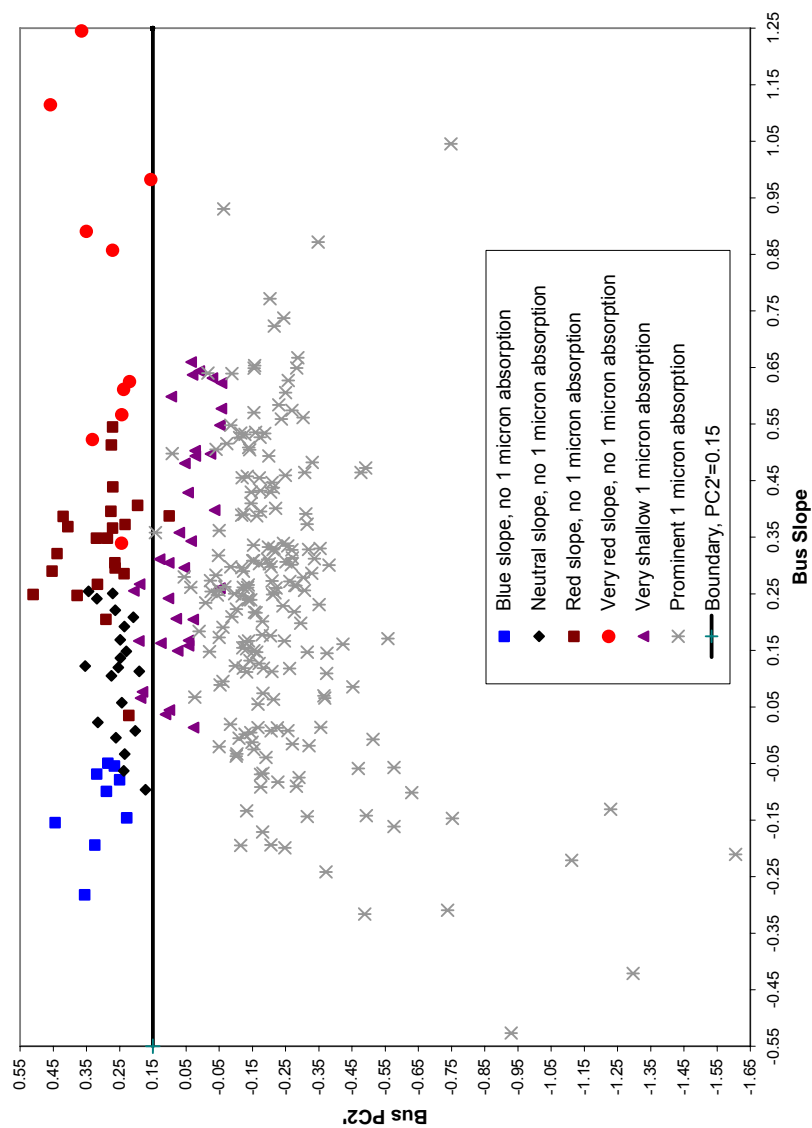


Figure 6.3. The method of classifying NEAs in Binzel et al. (2004a) that have neutral to red featureless spectra. By visually inspecting each of their spectra those objects which had no 1- μm absorption were identified and their approximate spectral slopes were determined. Those NEAs that plot above $\text{PC2}' = 0.15$ are considered to be consistent with the “Other” classification.

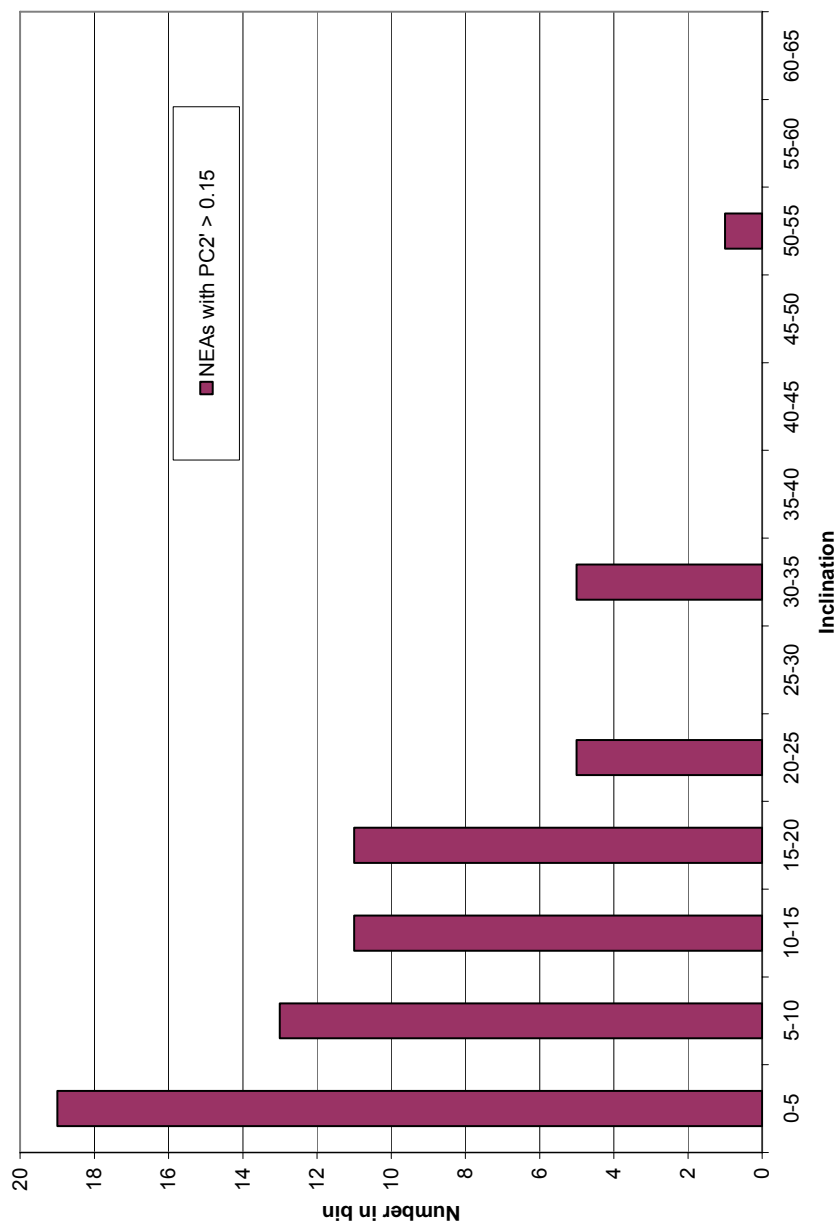


Figure 6.4. Inclination distribution for Binzel et al. (2004a) NEAs with $PC2' > 0.15$. Objects with such $PC2'$ values are considered to have no 1- μm absorption and fall in the “Other” classification. As with NEAs in our dataset which have linear, featureless spectra, most of these objects are at low inclinations. There also seems to be an increased abundance of such objects in the $0^\circ - 5^\circ$ inclination bin.

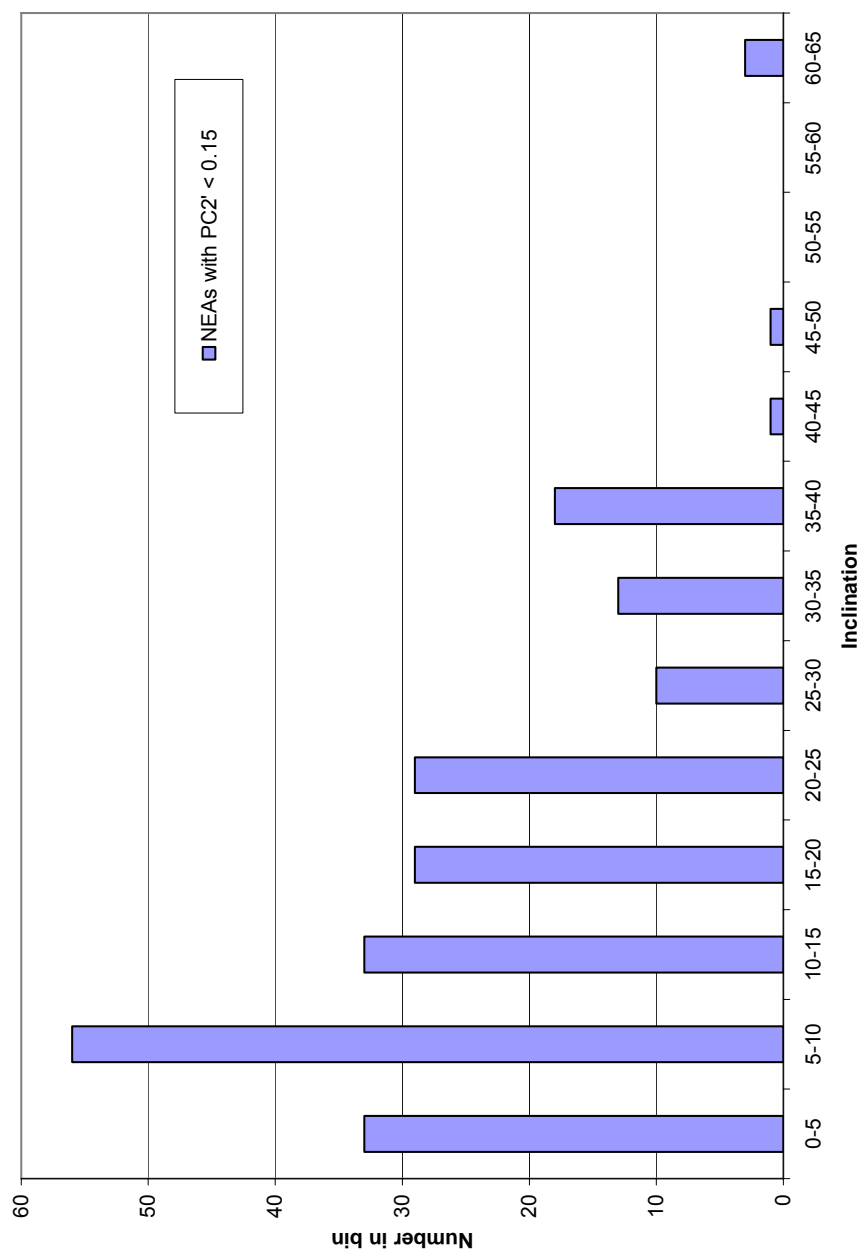


Figure 6.5. Inclination distribution for Binzel et al. (2004a) NEAs with $PC2' < 0.15$. Objects with such $PC2'$ values are considered to have a 1- μm absorption. As with NEAs in our dataset which exhibit this absorption, there is a relatively broad and flat distribution.

was noted in our own data (Figures 6.1 and 6.2) can be seen. Those NEAs with no 1- μm absorption are concentrated in low inclination orbits, with the peak in the 0° - 5° inclination bin. The inclination distribution is broader for objects that have a 1- μm absorption. In this case the sample size for both types of objects is large enough that statistical tests can be applied. The χ^2 -test for two binned data sets (Press et al., 2001) was used to test for differences between the inclination distributions for NEAs that show a 1- μm absorption compared to those which do not. The data was binned in inclination according to a low-inclination ($i < 20^\circ$) bin and a high-inclination bin ($i > 20^\circ$). Using this bin delimitation, the χ^2 -test shows the two distributions are different at a confidence level of 95.9%. Two additional statistical tests, the Kolmogorov-Smirnov (K-S) test and Student t-Test (Press et al., 2001), gave similar results. The K-S test gave a confidence level of 90.8%, indicating that the two distributions in inclination are likely different. This weaker, though still significant result, may be due to the fact that no bin delimitation is used for this test so biases in the choice of such a delimitation are removed. From the Student t-Test it was found the mean inclination for each of these groups was different at a highly significant confidence level of 99.4%. The original trend seen in our data thus persisted as statistically significant in the larger NEA spectral dataset of Binzel et al. (2004a).

6.2 – Extinct Comets within the NEA population

A dynamical method for distinguishing Extinct Comets from asteroids is the Tisserand parameter, T . Many researchers have used this quasi-constant for individual

orbits to identify asteroids that are in comet-like ($T < 3$) versus asteroid-like ($T > 3$) orbits (e.g. Kresák, 1979; Weissman et al., 1989). In Figure 6.6 those NEAs that have a low Tisserand parameter of $T < 3$ were identified. NEAs with $2.9 < T < 3.0$ were considered to be weakly associated with cometary orbits and those with $T < 2.9$ to be strongly associated with cometary orbits. This figure shows that the majority of objects which have comet-like orbits also have $PC2' > 0.15$. There are several objects, though, that are weakly associated with comet orbits that have unmistakable 1- μm absorptions. These were likely main-belt asteroids that had their eccentricity increased sufficiently to allow them to gravitationally interact with Jupiter (i.e., aphelia have approached Jupiter's semimajor axis). It is quite satisfying that essentially all NEAs that are strongly associated with comet orbits ($T < 2.9$) plot in the region of Principal Component space where one would expect Extinct Comets to reside.

Next, it was determined where the iron meteorites and enstatite chondrites plot in the diagram of $PC2'$ versus slope. Bus in his dissertation (1999) measured these parameters for 8 of these objects. These are plotted in Figure 6.7. By drawing a rough boundary around the iron and enstatite chondrite meteorites it was found that the region occupied by these types of meteorites is much smaller than that of the Extinct Comet Candidates. There are roughly 19 objects within this boundary which includes objects with no 1- μm absorption and those with a weak 1- μm absorption.

There are 9 NEAs in the intersection between that region and $PC2' > 0.15$. However 9 in this subset have $T < 2.9$ and thus are almost certainly Extinct Comets. Subtracting these leaves 5 objects with $PC2' > 0.15$ and whose spectra are consistent with

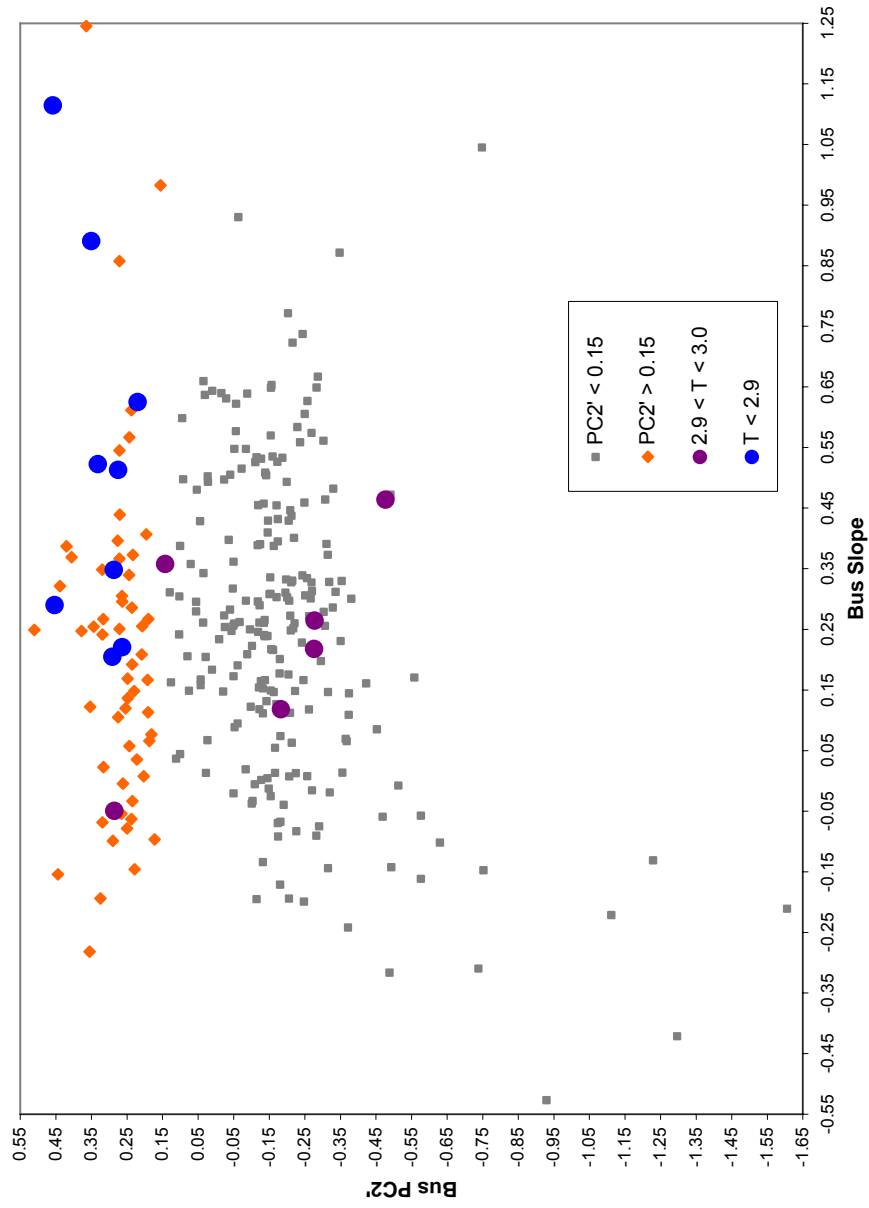


Figure 6.6. PC2' vs. Slope for Binzel et al.'s (2004) NEAs with low Tisserand values, T. Objects with $T < 3$ are assumed to have “comet-like” orbits. Objects with $T < 2.9$ are considered to be strongly associated with a cometary origin and those with $2.9 < T < 3.0$ to be less well-associated with such an origin.

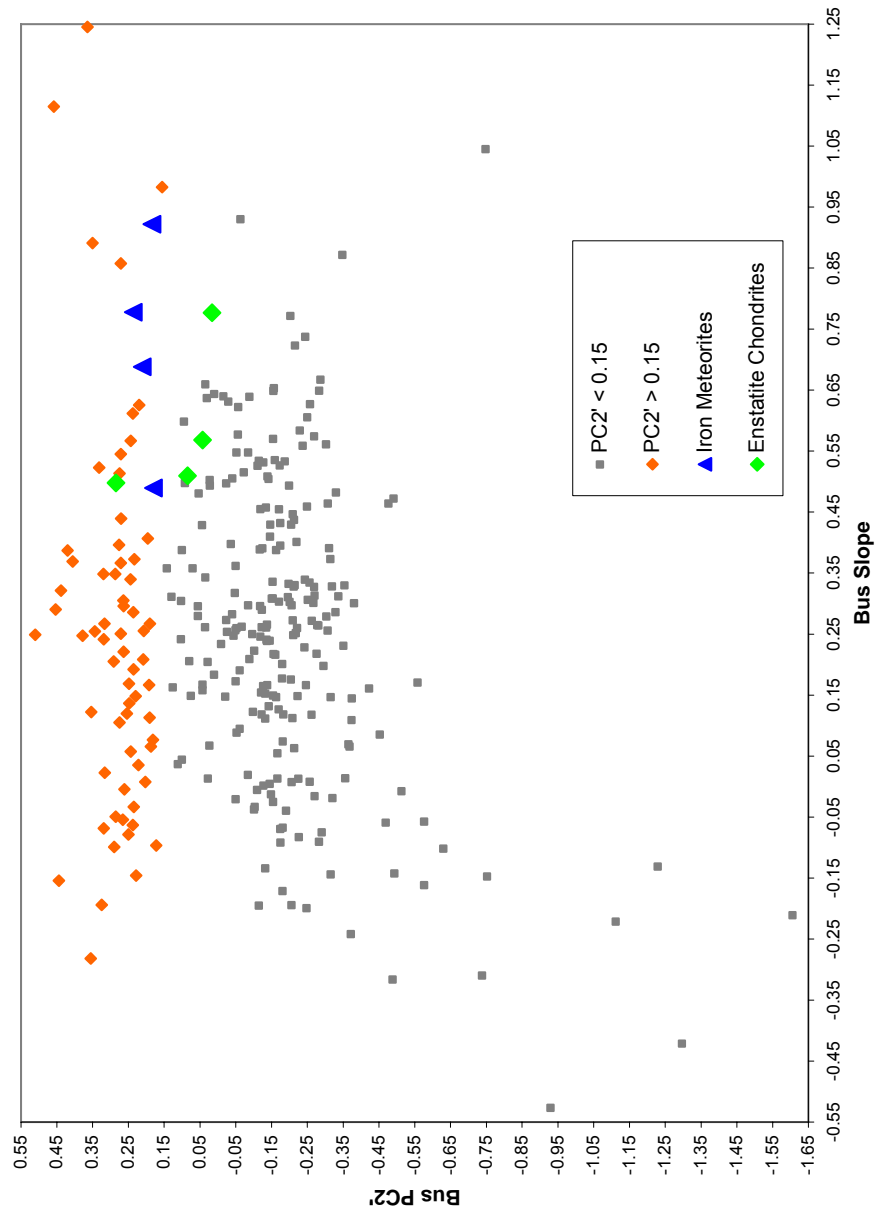


Figure 6.7. PC2' vs. Slope for Iron Meteorites (blue triangles) and Enstatite Chondrites (green diamonds) along with Binzel et al.'s (2004a) NEAs that are above and below a PC2' value of 0.15. The Iron and Enstatite Chondrite classes of meteorites have been associated with the M and E taxonomic classes of asteroids.

iron meteorites and enstatite chondrite meteorites. There are a total of 291 objects in the Binzel et al. (2004a) database for which spectral parameters are given. Of these, 65 have $PC2' > 0.15$. Therefore among the 65 objects that show no 1- μm absorption (i.e., $PC2' > 0.15$), the fraction that can be ascribed to iron and enstatite chondrite meteorites is roughly $5/65$ or roughly 8%. The majority of objects ($\geq 90\%$) above the line $PC2' = 0.15$ must be Extinct Comet Candidates. Considering the whole population of 291 objects in the Binzel et al. (2004a) data set, the total fraction of irons and enstatite chondrites is roughly $15/291$ or $\sim 5\%$.

As an independent check, the fraction of iron and enstatite material can be determined using meteorite falls and Antarctic finds. Table 6.1 lists the number and relative percentages of meteorite types of the least biased datasets, the global fall and Antarctic find data. Based on rough estimates of the amount of meteoritic material that survives passage through the atmosphere (Alexeev (2003); Pasek (2006)), the amount of material in NEA orbits can be estimated, and is shown in the last set of columns. From the fall data the percentage of enstatite-based NEAs is 1.17% and the percentage of iron-based NEAs is 0.75%. From the Antarctic find data the percentages of enstatite- and iron-based NEAs are 0.69% and 0.16%, respectively. Therefore, the total fraction of metallic and enstatite chondritic material in NEA orbits should be fairly low, between $\sim 1\%$ and $\sim 2\%$. This number is smaller than the estimate of roughly 5% in the previous paragraph. It should be emphasized that this is a very rough estimate. The amount of material that is vaporized or ablated during passage through the atmosphere for different meteorites (Alexeev (2003); Pasek (2006)) is quite uncertain. Nevertheless, by using

Table 6.1 - Estimate of NEA Compositional Abundances from Meteorite Fall and Find Data

<u>Class</u>	<u>Global Data^a</u>		<u>Antarctic Data^b</u>		<u>% Vaporized or Ablated^c</u>	<u>% in NEA Orbits</u>	
	<u>Falls</u>	<u>Freq. (%)</u>	<u>Finds</u>	<u>Freq. (%)</u>		<u>Falls</u>	<u>Antarctic Finds</u>
Chondrites							
Carbonaceous	35	4.21	342	3.24	99	31.44	25.22
Ordinary	661	79.45	9624	91.10	90	59.37	70.96
Enstatite	13	1.56	94	0.89	90	1.17	0.69
Other	3	0.36	7	0.07	90	0.27	0.05
Total	712	85.58	10067	95.29	90	92.24	96.92
Achondrites	69	8.29	365	3.46	90	6.20	2.69
Stony-irons	9	1.08	31	0.29	90	0.81	0.23
Irons	42	5.04	110	1.02	50	0.75	0.16

Notes: ^aSears and Todd (1988)

^bAstromaterials Curation, Meteorites from Antarctica website - http://www-curator.jsc.nasa.gov/antmet/us_clctn.cfm

^cAlexeev (2003) and Pasek (2006)

either of the above two methods the majority of objects ($\geq 90\%$) with no 1- μm absorption must be Extinct Comet Candidates. The fraction of Extinct Comet Candidates among the entire NEA population is roughly 60/291 or 21%. The rest are objects that are primarily composed of varying amounts of olivine and pyroxene and exhibit a 1- μm absorption.

6.3 - Conclusion

The question now naturally arises why Extinct Comet Candidates would concentrate in low inclination orbits. This clearly requires a detailed orbital evolution study which is beyond the scope of this dissertation. In lieu of this, some observational data is offered which lends support to the conjecture that as comet orbits evolve into NEA orbits the inclination appears to become smaller. Figure 6.8 shows the inclination distribution for those comets that have orbital periods greater than 200 years and whose perihelia are greater than 0.06 AU (i.e., all Long Period Comets excluding those among the Sungrazing groups (Marsden, 2005)). It has been known for a long time that such comets are isotropically distributed in space, thus yielding a rather uniform inclination distribution over the entire range of inclinations from 0° - 180° . (Note: The inclination distribution for comets that enter the planetary region from an isotropic distribution will follow a sine-law (Fernández and Ip, 1991).) Comets having periods between 20 and 200 years are shown next. These have a less uniform inclination distribution than the Long Period comets in Figure 6.9. This distribution is shifted toward lower inclinations, though it is still distributed over the entire 180° inclination range. Finally in Figures 6.10 and 6.11 the inclination distributions for comets with periods less than 20 years are

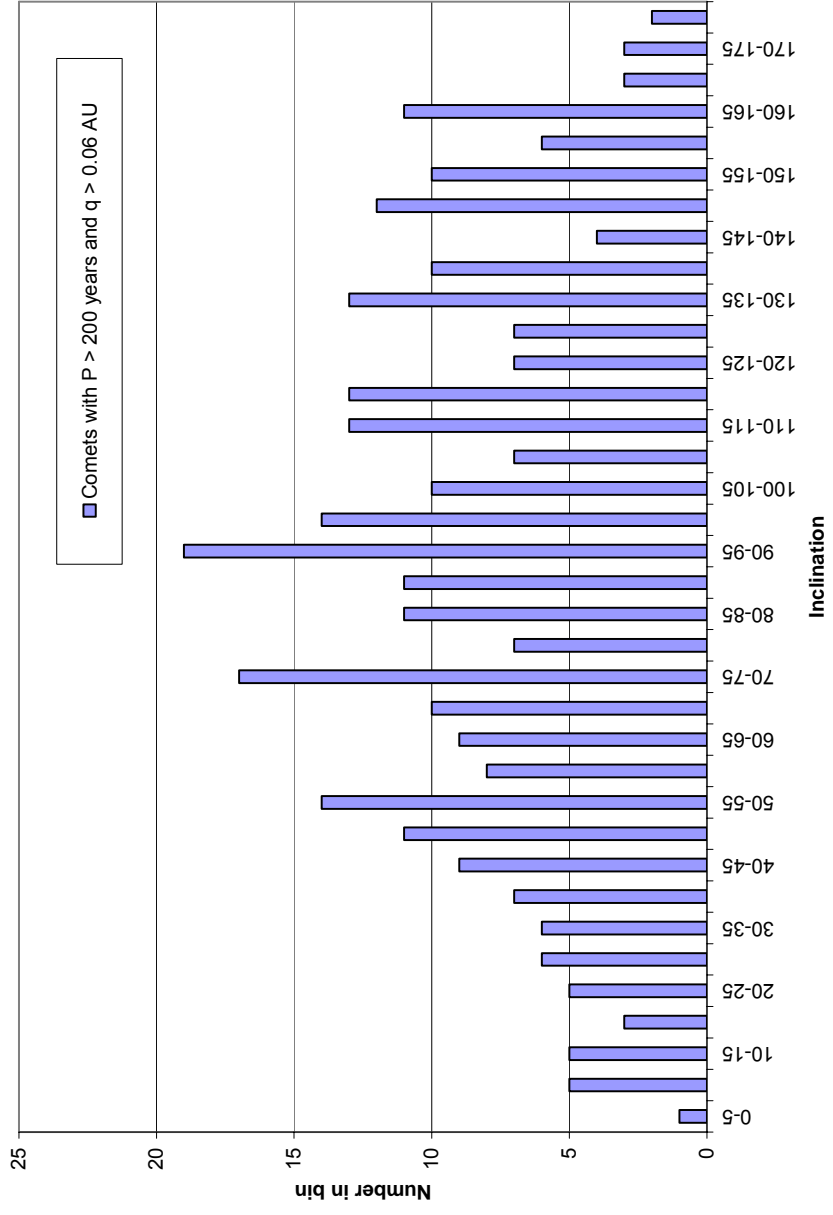


Figure 6.8. Inclination distribution for comets with orbital periods greater than 200 years (Long Period Comets). Those comets whose perihelia are less than 0.06 AU have been removed due the large number of split comets in that “Sungrazer” population. The Long Period Comets are distributed rather uniformly with respect to inclination once the Sungrazer population is taken out.

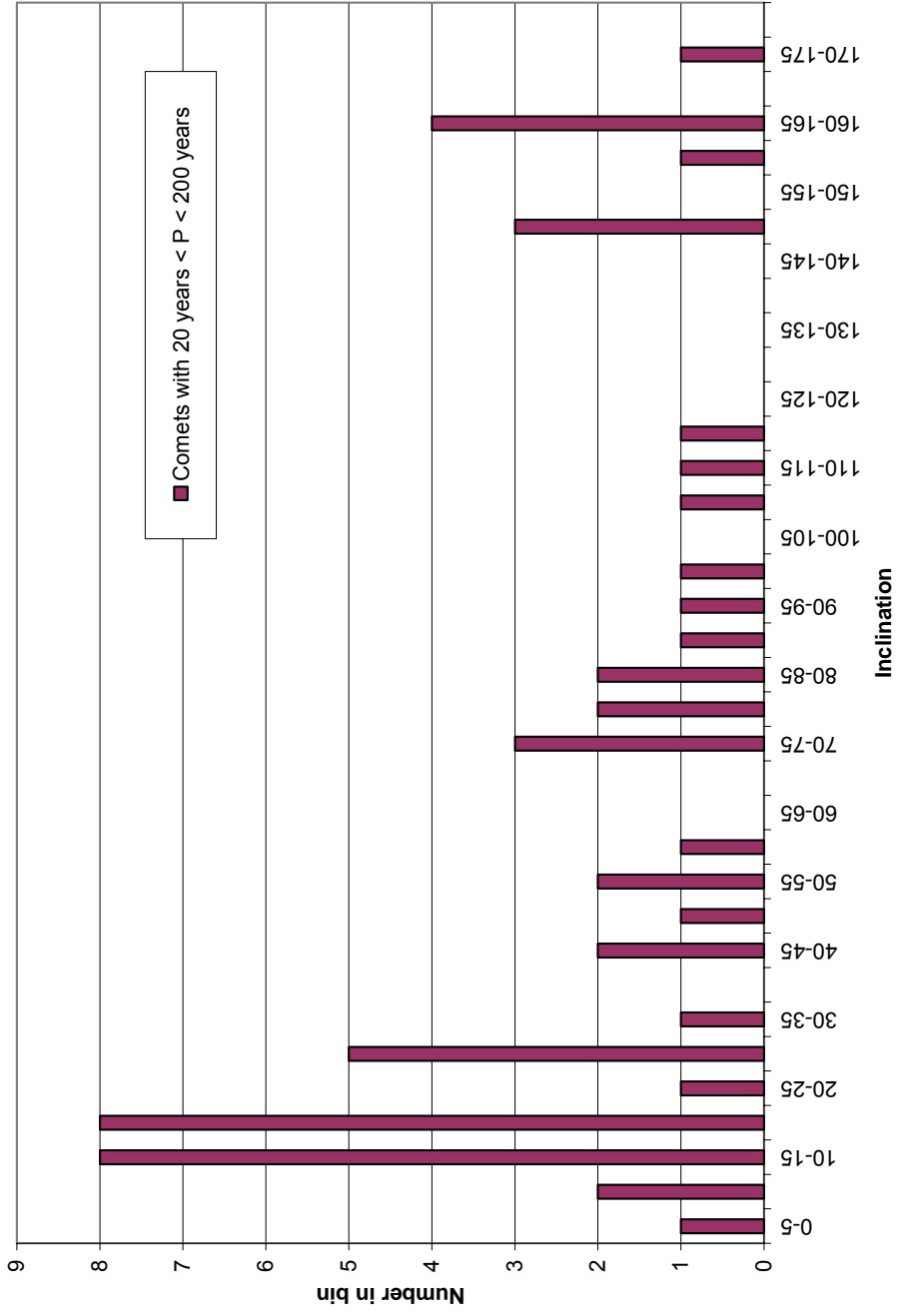


Figure 6.9. Inclination distribution for comets with intermediate orbital periods between 20 years and 200 years. This distribution is relatively evenly distributed across the range of inclinations except for the enhancement near low inclinations.

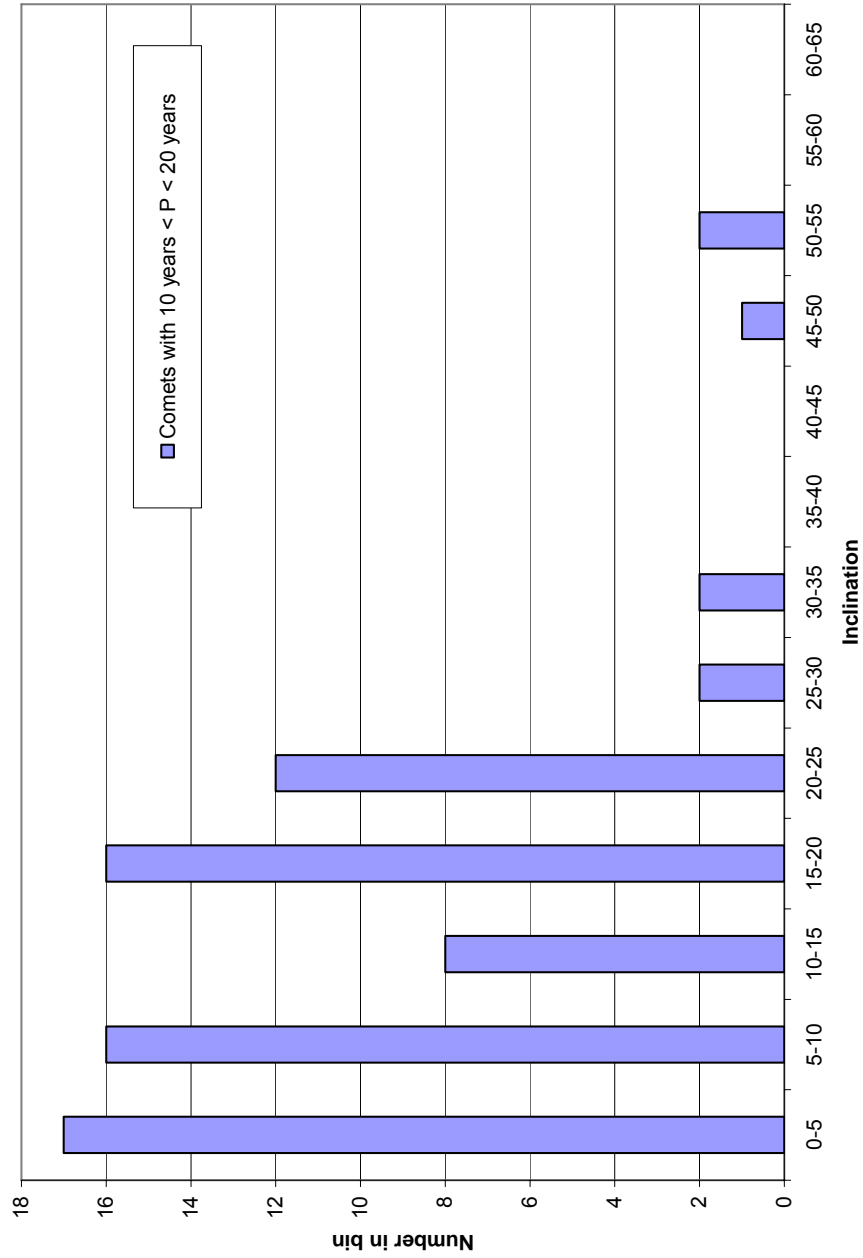


Figure 6.10. Inclination distribution for Short Period Comets with orbital periods between 10 and 20 years. Very few have inclinations above 25° and none have an inclination above 55° . These comets exhibit a flatter distribution between 0° and 25° than Short Period Comets with orbital periods less than 10 years, shown in Figure 6.11.

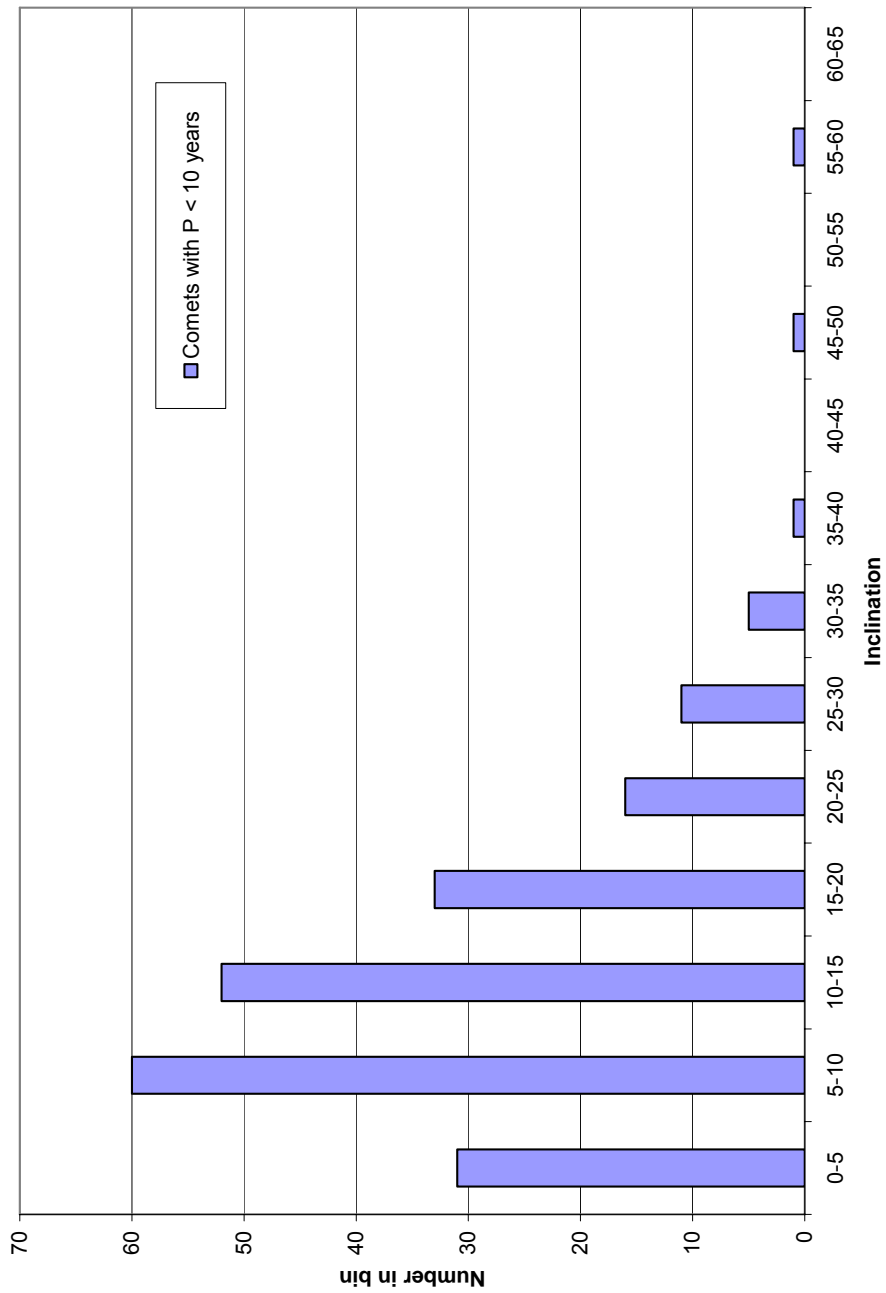


Figure 6.11. Inclination distribution for JFCs with periods less than 10 years. This inclination distribution approaches that of NEAs which are classified as “Others” in our NEA sample and those that have PC2’ values greater than 0.15 in the Binzel et al. (2004a) data.

shown. No members of this group of comets have inclinations greater than 60° and their distributions are shifted fairly strongly toward lower inclinations.

There appears to be a real trend of lower comet inclination with shorter orbital period. An explanation is that there is a selection effect. Comets that are in low inclination orbits have a much higher probability of making a close approach to a planet since they are near the ecliptic plane. Furthermore, they are in prograde orbits so close approaches to planets will be made at lower relative velocities, allowing the gravitational perturbing effects of these planets to act over longer periods of time.

6.4 – Summary

The primary source region for the NEAs is thought to be the asteroid main-belt though a small but significant fraction of these objects likely evolve into NEA orbits from cometary source regions, becoming asteroidal in appearance during this process. Levison and Duncan (1994) estimate there are 5-20 times as many extinct Jupiter Family Comets (JFCs) as there are active JFCs based on the orbital lifetime versus active lifetime of such objects. Because they are dormant there is an observational bias against finding them. A sizable number of these objects, though, can be perturbed into NEA orbits. Orbital analyses indicate the JFCs are a likely source region for such objects (Bottke et al., 2002a). Since such extinct JFCs are so much closer to Earth they are observed. Therefore, one would expect to find a number of Extinct Comets among the NEA population.

The investigations conducted for this dissertation indicate that Long Period Comets in low inclination orbits are preferentially perturbed into orbits with shorter periods. Those that have been perturbed into shorter period orbits (i.e., those whose distributions are shown in Figure 6.9) interact with planets more frequently and this selection effect becomes even more pronounced. The set of comets that have been perturbed into orbits with periods below 20 years have a distribution that has been shifted toward still lower inclinations (ref. Figures 6.10 and 6.11). For those with periods below 10 years (ref. Figure 6.11) the inclination distribution approaches that of the Extinct Comet Candidates (ref. Figures 6.1 and 6.4).

Extinct Comets in NEA orbits may result from this iterative dynamical process that preferentially perturbs some of the longer period comets in low inclination orbits into shorter period orbits. As these comets are perturbed into still shorter period orbits a greater fraction of their orbit is spent close to the Sun where insolation allows them to develop a thick crust. Because an insulating crust develops their cometary activity is extinguished. These Extinct Comet Candidates in our database and that of Binzel et al. (2004a) are consistent with this scenario.

In summary, empirical evidence that Extinct Comets preferentially occupy NEA orbits with low inclinations has been provided. While for the whole NEA population Extinct Comet Candidates comprise about $60/291 \approx 21\%$, for objects with inclinations less than 5° , Extinct Comet Candidates may comprise almost twice that fraction or about $19/52 \approx 37\%$. This finding can help in searching for Extinct Comet Candidates which should be more prevalent among low inclination NEAs.

CHAPTER 7

SUMMARY AND FUTURE WORK

It was found that unlike the asteroid main-belt, a large number of objects among the NEAs have spectra consistent with ordinary chondrites. There is a continuum of spectral types between S-type and OC-like spectra. Objects which exhibit the spectral signature of ordinary chondrites tend to be in highly eccentric Apollo class orbits that cross the asteroid main-belt. These same objects are in a collisionally enhanced environment which likely is a reason for their fresh surfaces. About 20% of the NEAs have spectra consistent with Extinct Comets. These objects tend toward low inclination orbits which may point toward a cometary origin.

In order to determine more definitive conclusions regarding S-type and OC-like NEAs, the following research endeavors would be very helpful:

1. a) Dynamical models that address the surface lifetime (i.e., time between resurfacing events) for NEAs in different orbits.
b) Dynamical models that can estimate lifetimes of various asteroid populations.
2. a) Observations with modern spectrographs that span 0.3- μm to 2.5- μm so that all of the major asteroid absorption features that are diagnostic of mineralogical composition can be analyzed.
b) Such spectra can then be used to determine a number of important mineralogical parameters rather than just our slope and band depth parameters. These parameters can then be used to better define the presence and relative abundances of olivine,

pyroxene, iron, organics, feldspar and spinel.

3. This type of data can then lead to the derivation of an asteroid taxonomy that is directly related to mineralogical features.
4. Better understanding of “space weathering” including laboratory experiments to determine the effects of solar UV and X-ray radiation.
5. Spacecraft missions that provide in-situ characterization of the surface mineralogy and regolith of NEAs of varying spectral types and sizes.

Investigations of Extinct Comet Candidates among the NEAs are clearly in an early phase of development. The following studies are suggested:

1. Orbital evolution computer simulations which test the conjecture that Short Period Comets and Extinct Comets evolve from the low-inclination subset of Long Period Comets.
2. Detailed surveys of the known population of low-inclination NEAs to determine if there is a correlation with other physical characteristics (e.g. low albedo) consistent with Extinct Comets.
3. Better estimates for the amount of iron- and enstatite-based material in NEA orbits.
4. Determinations as to whether other meteorite types (e.g. metamorphically altered carbonaceous chondrites) are inconsistent with Extinct Comets along with their estimated abundance within the NEA population.
5. Spacecraft sample-return missions from NEAs that have featureless neutral to red sloped spectra to determine if their composition is consistent with Extinct Comets.

APPENDIX A - NEA SPECTRA FROM OUR SURVEY

Individual NEA spectra used in this dissertation are shown. The best spectrum of each object is plotted. In each of the plots the binned spectrum is superimposed on the unbinned spectrum. The NEA's name is shown in the upper left corner. On the line below the name, the object's classification is shown, along with the grouping (in parentheses where applicable) to which it was assigned in Figure 3.4 or 3.5. The grade shown on the third line is the **average** grade for all spectra of the object.

As outlined in the captions of Figures 3.4 and 3.5 the spectra are grouped into classes A, B, C and D according to their slope and band depth. The spectra are grouped in this appendix using the same method.

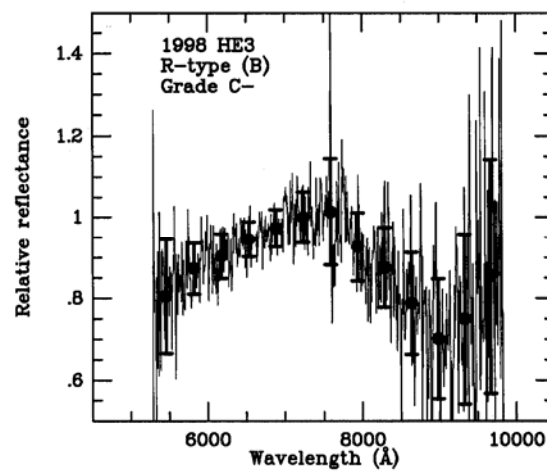
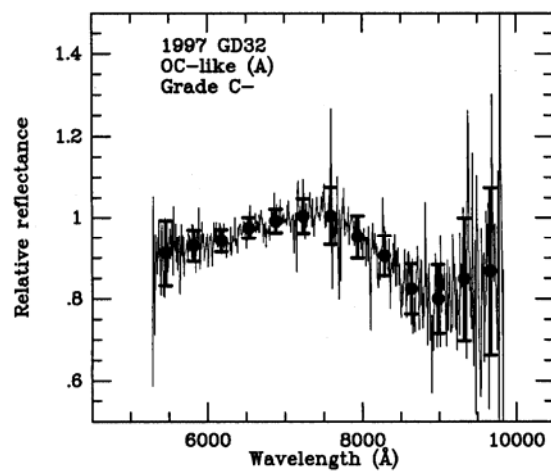
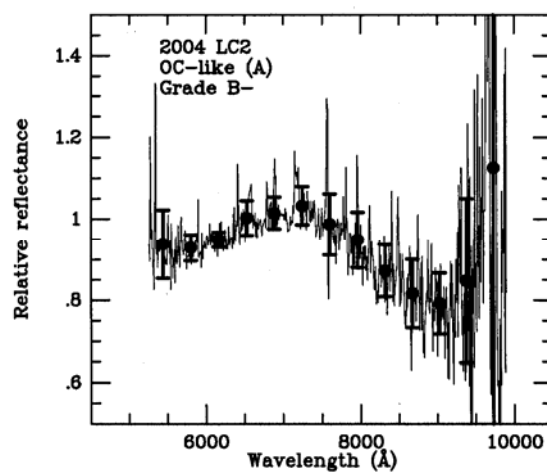
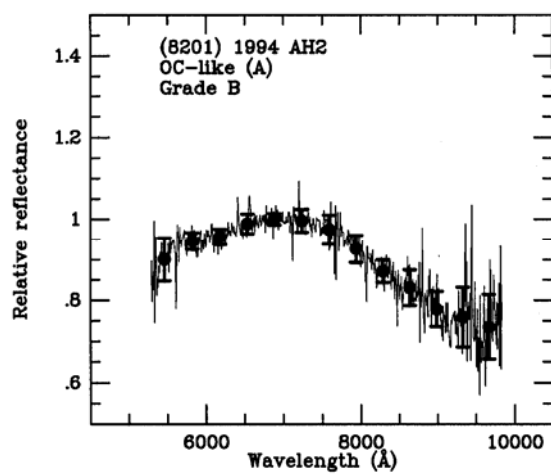
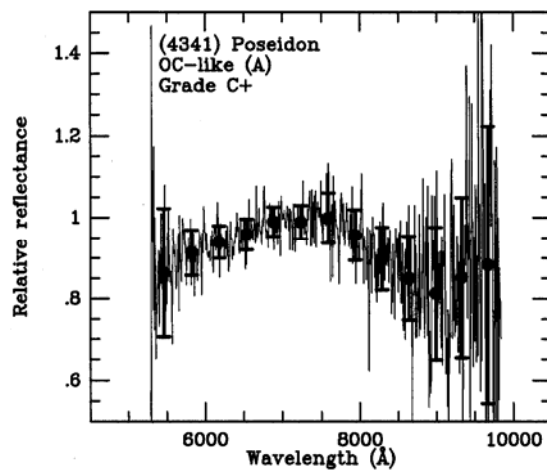
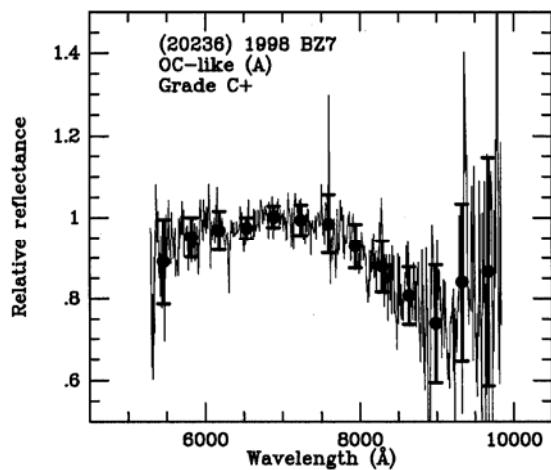
Pages 114-116 – 15 OC-likes and 1 R-type (cf. Figure 3.4)

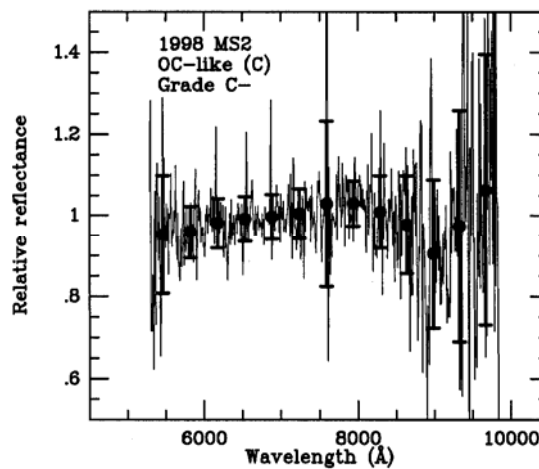
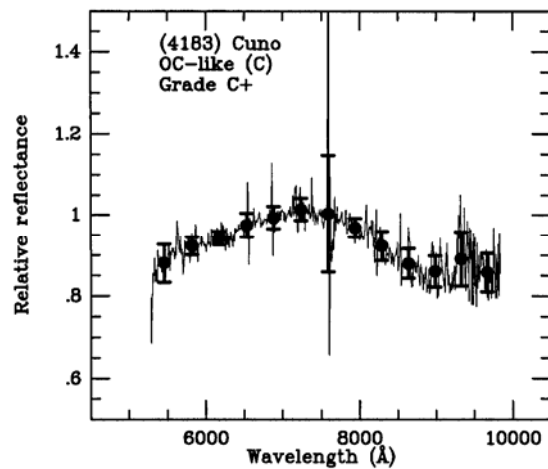
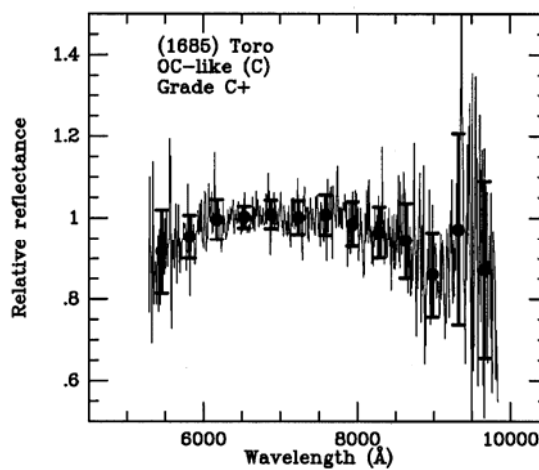
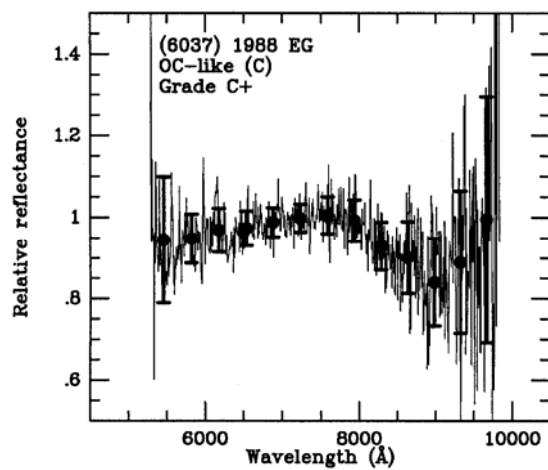
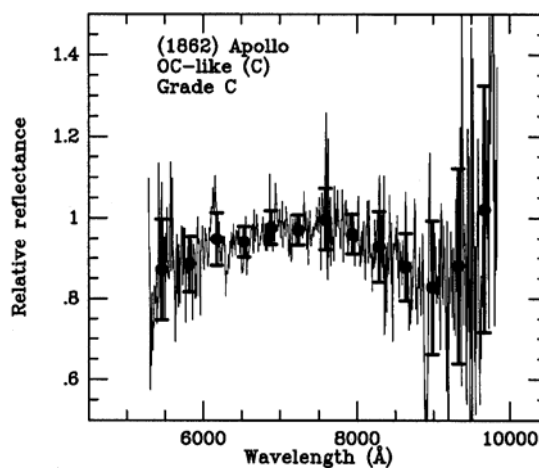
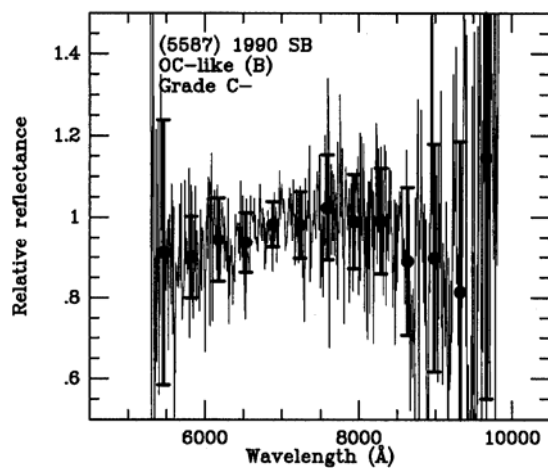
- Group A - deep band depth and shallow slope
- Group B - deep band depth and moderate slope
- Group C - moderate band depth and shallow slope
- Group D - moderate band depth and moderate slope

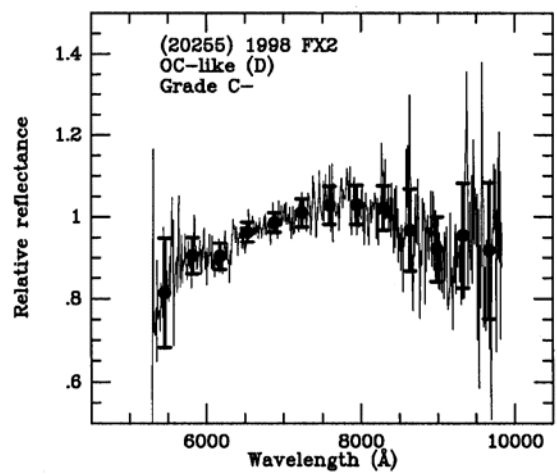
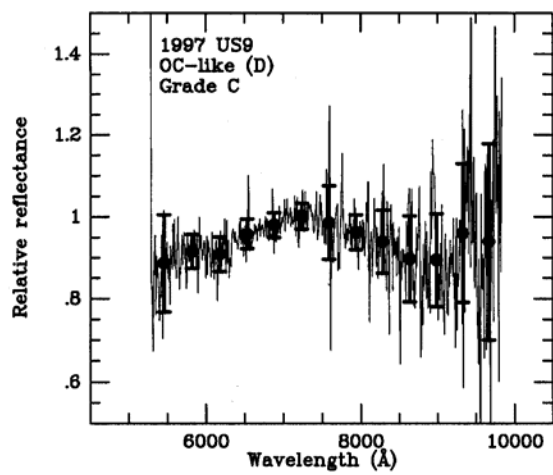
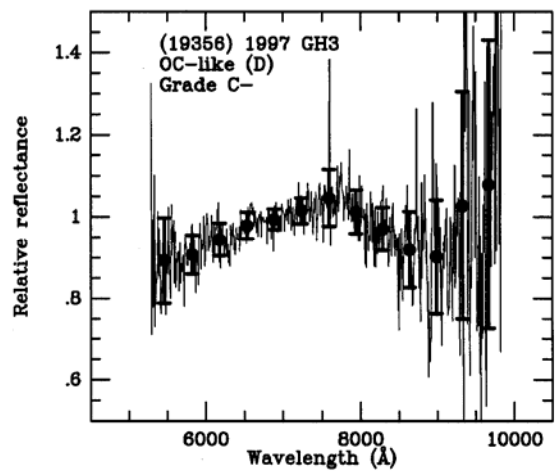
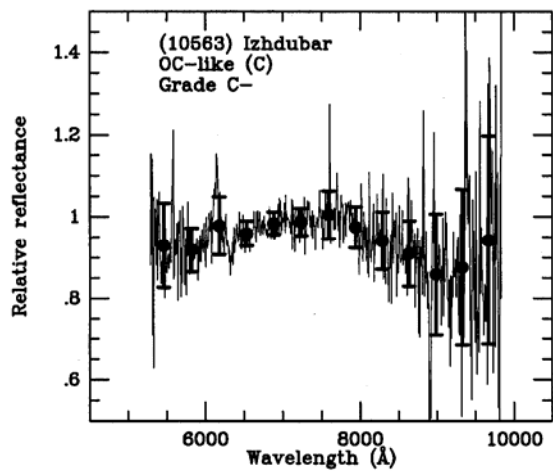
Pages 117-120 – 17 S-types and 2 BOC-likes (cf. Figure 3.5)

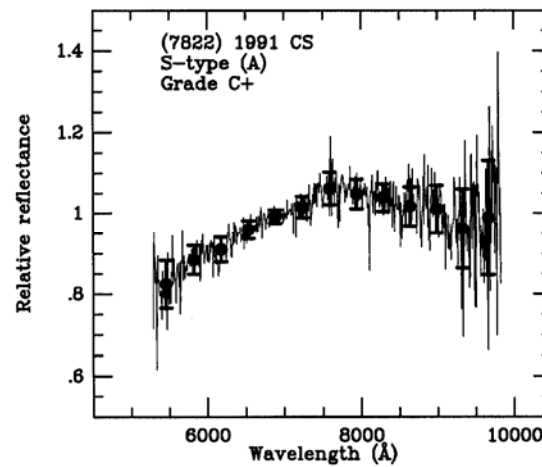
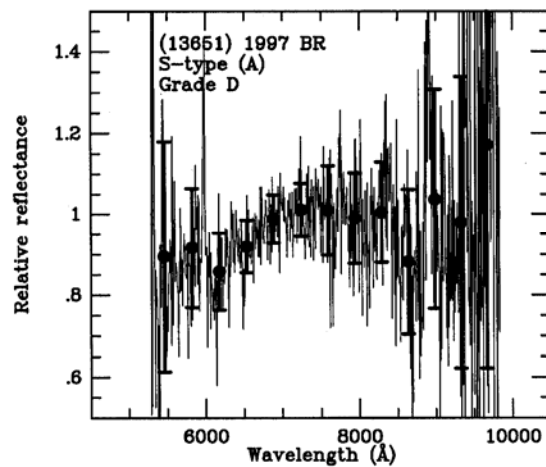
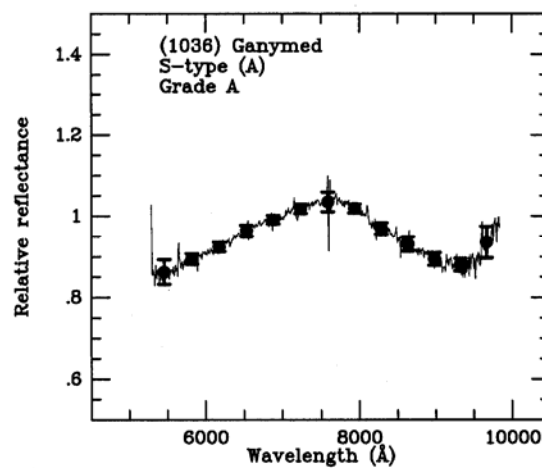
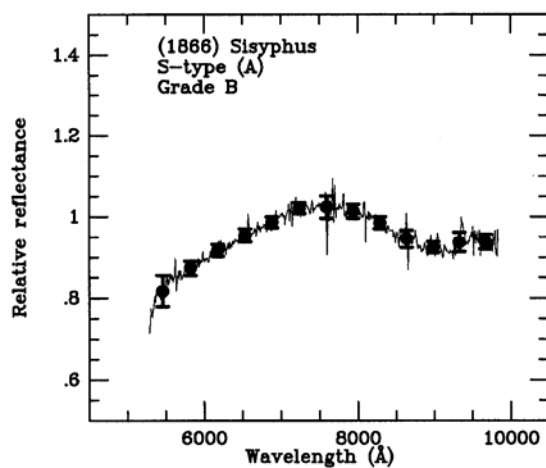
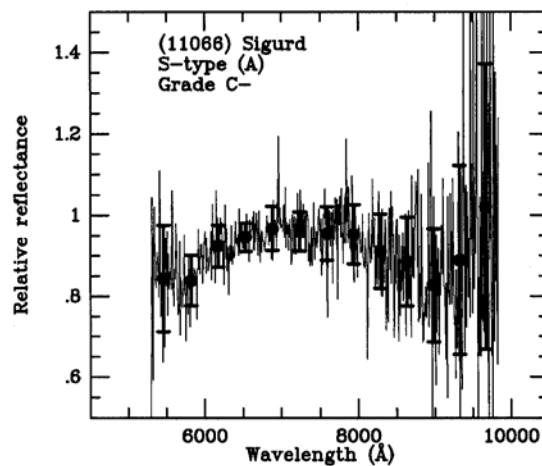
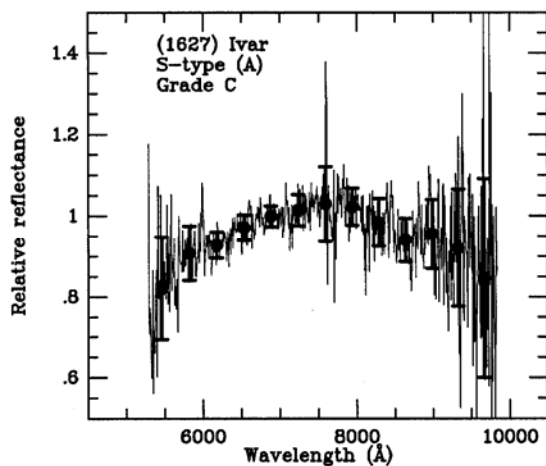
- Group A - moderate band depth and various slopes
- Group B - shallow band depth and shallow slope
- Group C - shallow band depth and moderate slope
- Group D - shallow band depth and steep slope

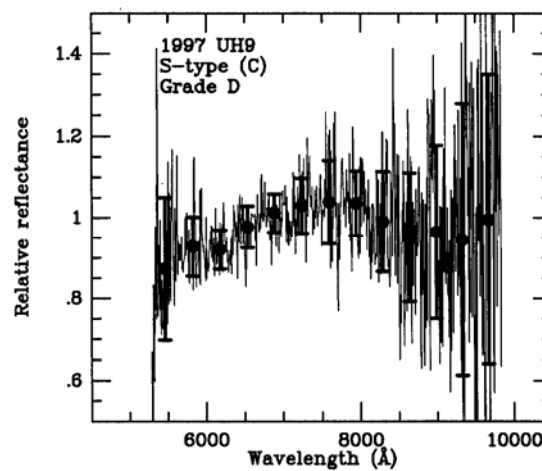
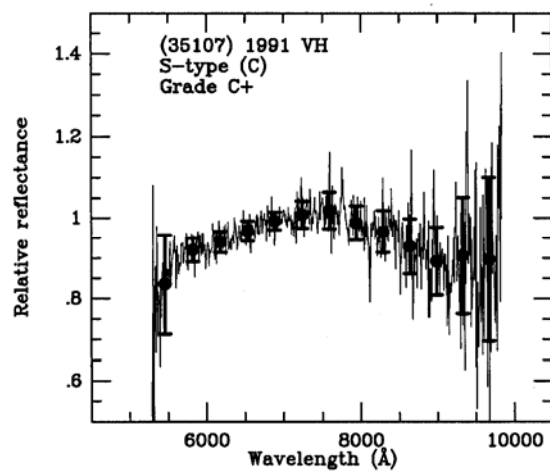
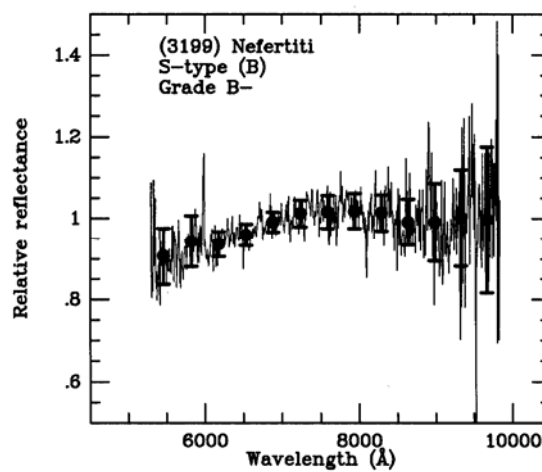
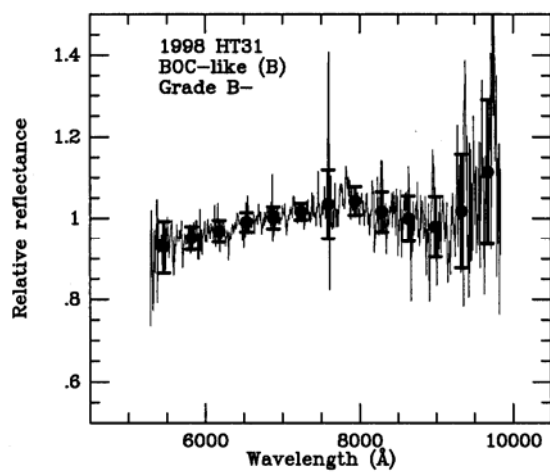
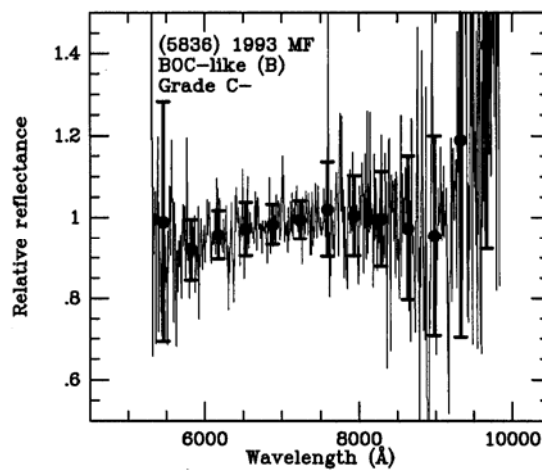
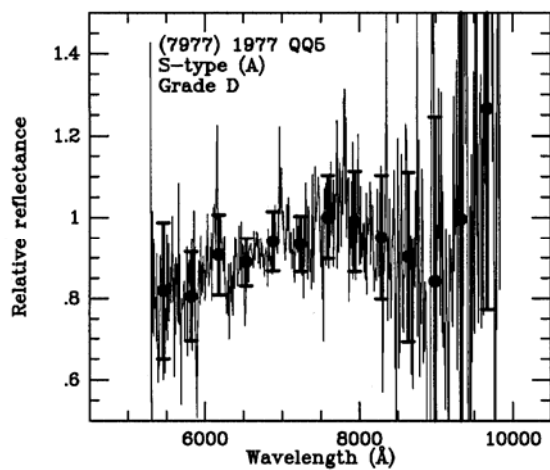
Page 121 – NEAs which do not exhibit a 1- μ m absorption (cf. Figure 3.6).

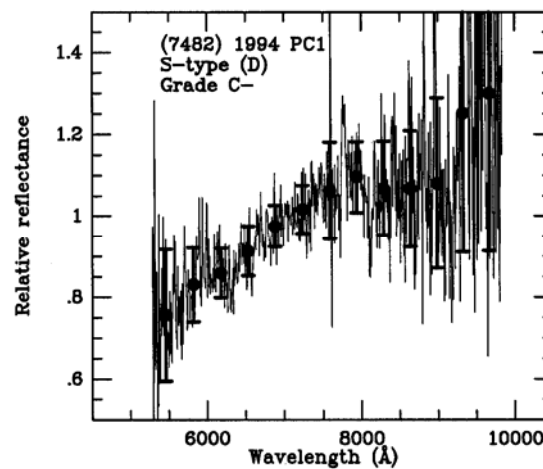
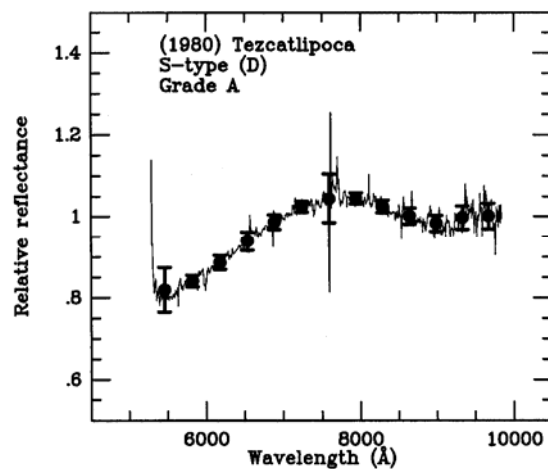
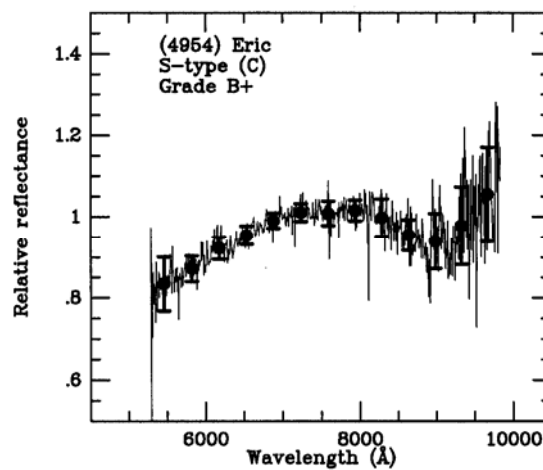
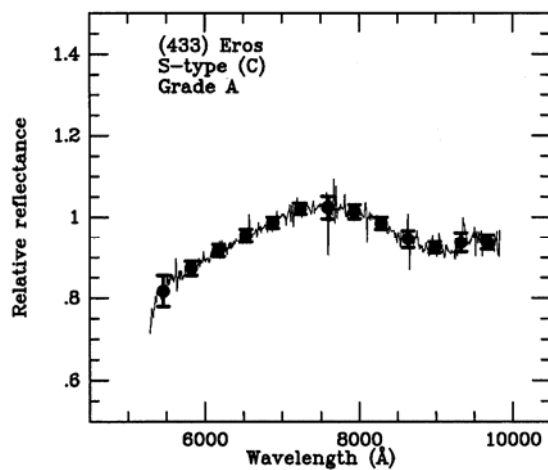
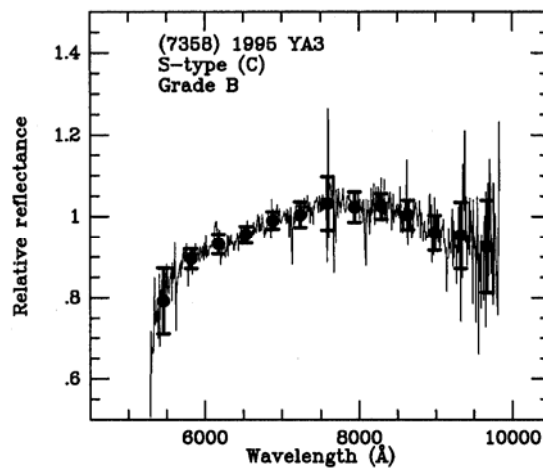
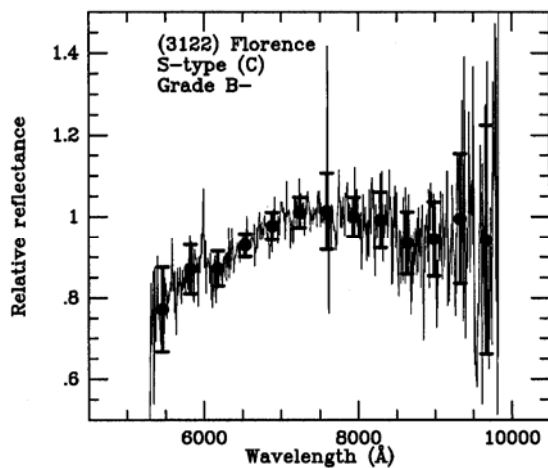


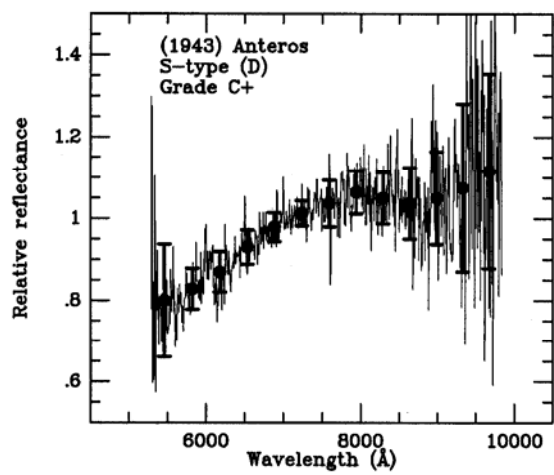


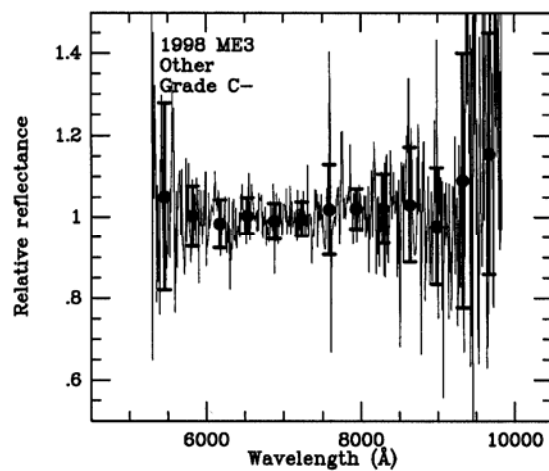
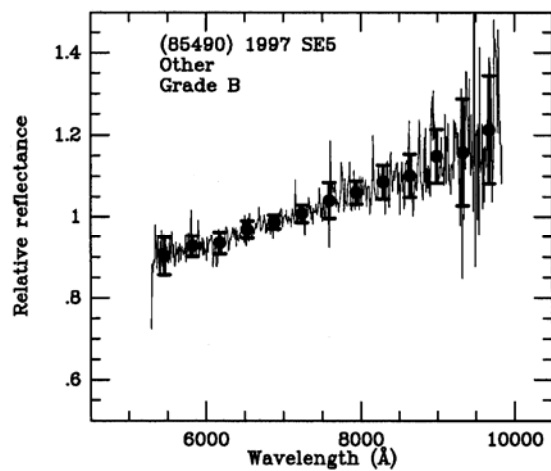
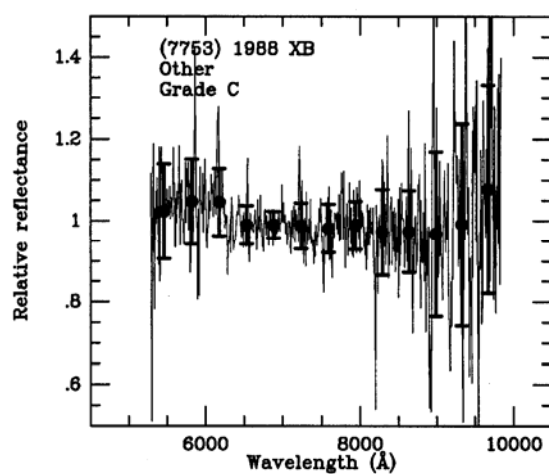
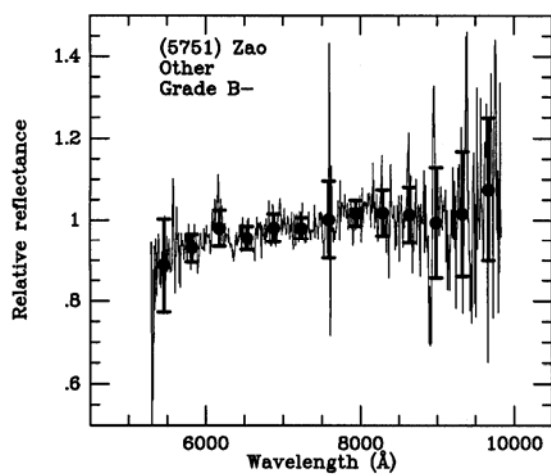
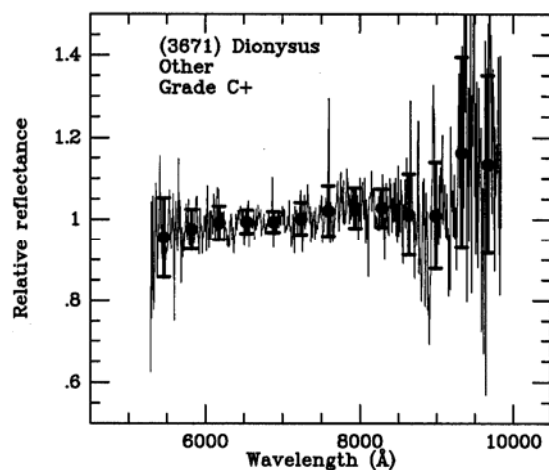
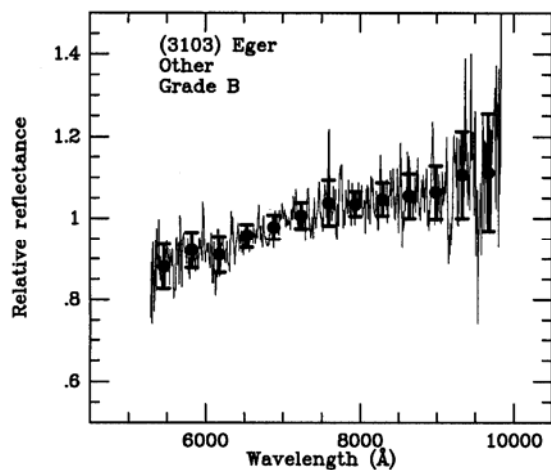












APPENDIX B – NOTES ON TAXONOMIC CLASSIFICATION

The first method of classifying asteroids according to their spectral characteristics was defined by Chapman et al. (1975). Since that time, a number of researchers have derived methods of classifying asteroids using clustering methods, the details of which are described in Bowell et al. (1978), Tholen and Barucci (1989), and Bus et al. (2002). The two most prominent classification schemes, the Tholen (Tholen, 1984) and Bus (Bus, 1999) taxonomies, have utilized Principal Component Analysis (PCA) to assign letter designations to objects having similar spectral characteristics. Principal Component Analysis is a method of reducing the complexity of a multi-parameter dataset. The dimensionality of the dataset is effectively reduced by a linear transformation of its parameters so that their maximum variance lies along the first principal component (PC1), the second largest variance lies along the second principal component (PC2), etc. Via this method, clusters of objects having similar spectral features ought to separate in Principal Component space.

As an exercise Principal Component Analysis was performed on our NEA data and those of Gaffey (1976) and Gaffey et al. (1993a) represented in Figure 3.2. Since there are only two parameters, this analysis was fairly straightforward. It should be noted, though, that in addition to our slope and band depth parameters, there actually is a third parameter, the presence or absence of a 1- μm absorption, which allows the identification of objects having an "Other" classification. For the purpose of this Principal Component Analysis, though, and since the main purpose of this exercise was

to illustrate how Principal Component Analysis could be performed on a dataset, objects which do not have a 1- μm absorption were not included in this brief analysis. The first step in applying Principal Component Analysis to our 2-parameter database was to fit our (Slope, Band Depth) data points. Both a Linear Least Squares (LLS) fit and chi-square fit to the data were performed. Finding no qualitative difference in the end result, the LLS-fit was used in this analysis. Next, the data points and the fit were translated so the fit intercepted the origin. Finally, the coordinate system was rotated so that one of the axes (PC1) coincided with the fit. Along this axis the variance had been maximized. Along the other, orthogonal axis, (PC2) the variance had been minimized. The results of this analysis are displayed in Figure B.1. By comparing this plot to Figure 3.2 it can be seen that they are qualitatively the same. The conclusion from performing a Principal Component Analysis on our NEA and Gaffey's data is that for our two-parameter dataset, no additional information is gained by doing such an analysis over the original analysis (cf. Chapter 3) which involved simply plotting band depth versus slope.

The Tholen taxonomy (Tholen, 1984) utilizes the Eight-Color Asteroid Survey (ECAS) dataset of asteroid observations along with Principal Component Analysis and "the minimal tree algorithm." Photometry of 405 asteroids through eight filters, with an effective wavelength range of $\sim 3000 \text{ \AA}$ to $\sim 11000 \text{ \AA}$, were used to define this taxonomy. The seven color indices resulting from these observations were the parameters used for the Principal Component Analysis. Following the transformation to Principal Component space, 68% of the variance was along PC1, 27% was along PC2, and the remaining 5% of the variance was along the other five Principal Component axes. Thus,

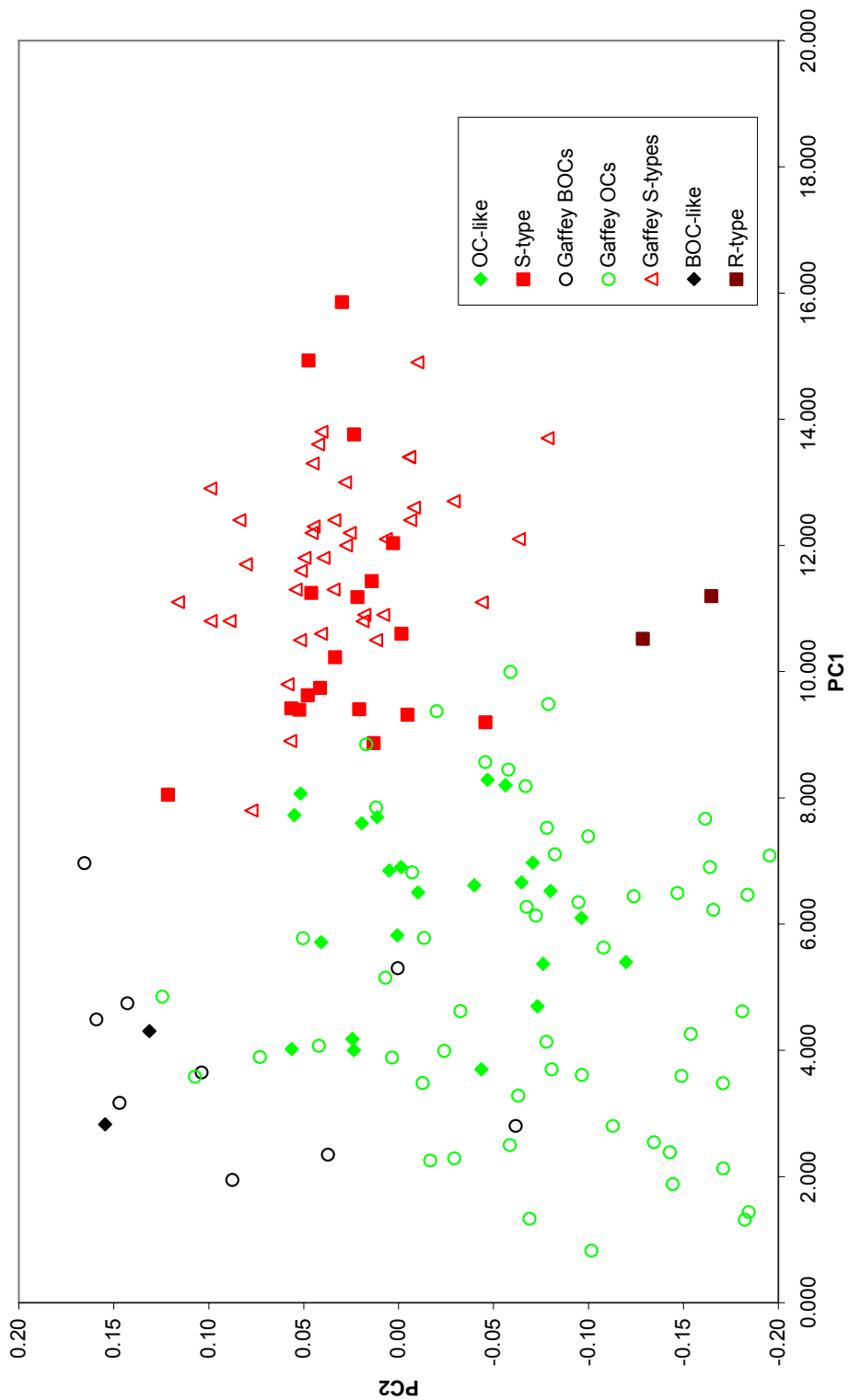


Figure B.1. Principal Component Analysis of our NEAs. Qualitatively, there is no difference between this plot and Figure 3.2.

most of the variance in this dataset was represented by the first two principal components with PC1 being best correlated with the ultraviolet absorption and PC2 being best correlated with the 1- μm absorption, the two most prominent features in asteroid spectra over this wavelength range. Next, clusters in Principal Component space were searched for using a minimal tree method. In this method, each asteroid is associated with up to two other asteroids, forming a "tree" with no closed loops. The "minimal tree" is the one which is of shortest length in Principal Component space. The longest "branches", or links between asteroids, are then cut to form clusters, associated with each of Tholen's taxonomic classes. There are 14 different classes in Tholen's taxonomy. The mean spectra for each are shown in Figure 5 of Tholen and Barucci (1989). It should be noted that the E, M and P classes are differentiated by albedo only. In the absence of supplementary albedo information, an asteroid exhibiting this type of spectrum would receive an X classification. A description of the spectral and albedo characteristics for each of these taxonomic classes is given in Table I of Tholen and Barucci (1989).

The Bus taxonomy (Bus, 1999) is based on CCD spectroscopic observations of 1447 asteroids over a wavelength range of 4400 \AA to 9200 \AA . This taxonomy attempts to be consistent with the Tholen taxonomy and make full use of the higher resolution spectroscopic data over this wavelength range. Though it uses Principal Component Analysis, as does the Tholen taxonomy, it departs from a purely algorithmic approach and allows for some human judgment to be used in determining an object's classification. Furthermore, some of the boundaries used to define the range of classifications in Principal Component space are set by the range of these parameters seen in known

asteroid families of presumably more or less homogeneous composition. Parameterization of the spectra used for the Bus taxonomy began by fitting the final spectrum for each object with a smoothing spline and producing 49 fitted points at 100 Å intervals along the spectrum. A least squares linear fit to these points was then computed, the slope of this fit being the first parameter (called "Slope") used to characterize these spectra. The fitted spectrum was then divided by this best fit line and the residual spectrum was parameterized using Principal Component Analysis. This resulted in three spectral parameters for each asteroid classified in the Bus Taxonomy; Slope, PC2' and PC3'. According to Bus and Binzel (2002a), PC2' is most sensitive to the depth of the 1- μm absorption while PC3' is more sensitive to a UV or 7000 Å absorption. There are 26 different classes in the Bus taxonomy. The mean spectra for each are shown in Figure 15 of Bus and Binzel (2002a). A description of the spectral characteristics for each of these taxonomic classes is given in Table II of Bus and Binzel (2002a).

In like manner to the work done to classify our data according to the Tholen taxonomy (ref. Chapter 3), an effort was made to classify our objects in a manner consistent with the Bus taxonomy. It was quickly decided, though, that the benefit in doing so would be limited (e.g., albedo estimates for each taxonomic class that can be used for size estimates do not exist for the Bus taxonomy as they do for the Tholen taxonomy.) Furthermore, some possible inconsistencies were found in their data and classification method:

1. The final processing of their spectra could be better explained (Bus and Binzel, 2002a). It is not clear how the error bars for their spectra were determined and, therefore, difficult to judge the true quality of their spectra. It is also not well-defined how they dealt with bad pixels in the final spectra which were flagged and removed. It appears that a significant amount of post-processing of their final spectra was done which should be better explained.

2. Their derived parameters, Slope, PC2' and PC3', are a poor match to our spectral parameters. While the spectral slope is measured only over a featureless region of our spectrum, from 5500 to 7000 Å, their Slope parameter is measured over their entire wavelength range, from 4400 to 9200 Å and includes the 1- μ m absorption region. This sometimes results in objects with very different spectra having very similar Slope values (e.g., (3200) Phaethon and (8566) 1996 EN in Appendix B of Binzel et al. (2004a)). Similarly, PC2' is not necessarily well correlated with a 1- μ m absorption (i.e., our band depth parameter.) As an example, two of their objects with nearly identical PC2' values, (3352) McAuliffe and 1998 VO33, have very different 1- μ m absorption features (ref. Appendix B of Binzel et al. (2004a)). Finally, it is not clear that PC3' can be very well-correlated with a UV absorption shortward of 5500 Å. From Figure 5 of Tholen and Barucci (1989) it can be seen that this absorption is not significant above approximately 4000 Å for most asteroids, at or below the lower limit of their wavelength range. Furthermore, their sensitivity below 5500 Å, as is the case for our own spectra, is questionable, especially when one considers the representative spectra in Figure 1 in Bus et al. (2002). It is apparent from this figure that their spectra of faint NEA targets must

be questionable in this region when the spectrum of even the brightest of all asteroids, (4) Vesta, shows degradation shortward of 5500 Å. This issue involving PC3' surfaces in Chapter 5 of this dissertation when Vesta-like (V-types) and achondrite-like spectra are addressed.

3. The Bus taxonomy includes 26 separate taxonomic classifications, perhaps more than can be supported by the data. The only significant clustering of their data in Principal Component space occurs for two groups of objects; those which exhibit a 1- μm absorption and those that do not (Bus and Binzel, 2002b). Otherwise, there is a continuum of spectral characteristics within each of these groups. It may be they are seeing more of an observational difference (i.e., phase reddening, space weathering, differing surface particle sizes, etc.) than a mineralogical difference in objects between groups. Furthermore, some members of the Bus X-class show a 1- μm absorption (ref. Figure 15 of Bus and Binzel (2002a), especially the plots for the mean spectra for the Xc and Xe classes). In Figure 5 of Tholen and Barucci (1989) no such absorption is seen for the EMP (i.e., X-class) spectrum, making the Bus taxonomy inconsistent with Tholen's. Some of the objects that might be considered to be S-types in my classification scheme and Tholen's taxonomy would likely fall within Bus's X-class. This problem is also addressed in Chapter 5 of this dissertation.

The Tholen and Bus taxonomy were created with internally consistent datasets, different from ours. Therefore, to strictly classify according to either of these taxonomies would not be possible. The primary difficulty is that the wavelength range is different between both our spectra and those used by Bus and our spectra and the

spectrophotometric measurements used by Tholen. Because of this, it is only possible to say a given object's spectrum in our dataset is "most consistent with" a certain classification within either of these taxonomies.

REFERENCES

- Alexeev, V. A. 2003. Meteorite ablation evaluated from data on the distribution of cosmogenic neon isotopes. *Solar System Research* **37**, 207–217.
- Bell, J. F., D. R. Davis, W. K. Hartmann and M. J. Gaffey 1989. Asteroids: The big picture. In *Asteroids II* (R. P. Binzel, T. Gehrels, and M. S. Matthews, Eds.), pp. 921-945. University of Arizona Press, Tucson.
- Binzel, R. P., S. J. Bus, T. H. Burbine and J. M. Sunshine 1996a. Spectral properties of near-Earth asteroids: Evidence for sources of ordinary chondrite meteorites. *Science* **273**, 946-948.
- Binzel, R. P., S. J. Bus, T. H. Burbine and J. M. Sunshine 1996b. A spectroscopic survey of Near-Earth Asteroids: evidence for an S-asteroid ordinary chondrite link. American Astronomical Society, DPS meeting #28.
- Binzel, R. P., A. W. Harris, S. J. Bus and T. H. Burbine 2001a. Spectral properties of near-Earth objects: Palomar and IRTF results for 48 objects including spacecraft targets (9969) Braille and (10302) 1989 ML. *Icarus* **151**, 139-149.
- Binzel, R. P., A. S. Rivkin, S. J. Bus, J. M. Sunshine and T. H. Burbine 2001b. MUSES-C target Asteroid (25143) 1998 SF36: a reddened ordinary chondrite. *Meteorit. Planet. Sci.* **36**, 1167–1172.
- Binzel, R. P., A. S. Rivkin, J. S. Stuart, A. W. Harris, S. J. Bus and T. H. Burbine 2004a. Observed spectral properties of near-Earth objects: results for population distribution, source regions, and space weathering processes. *Icarus* **170**, 259-294.
- Binzel, R. P., M. Birlan, S. J. Bus, A. W. Harris, A. S. Rivkin and S. Fornasier 2004b. Spectral observations for near-Earth objects including potential target 4660 Nereus: results from Meudon remote observations at the NASA Infrared Telescope Facility (IRTF). *Planet. Space Sci.* **52**, 291–296.
- Binzel, R. P., E. Perozzi, A. S. Rivkin, A. Rossi, A. W. Harris, S. J. Bus, G. Valsecchi and S. M. Slivan 2004c. Dynamical and compositional assessment of near-Earth object mission targets. *Meteorit. Planet. Sci.* **39**, 351–366.
- Bottke, W. F. 1995. The Collisional and Dynamical Evolution of Asteroids. Ph.D. dissertation, University of Arizona.

Bottke, W. F., M. C. Nolan, H. J. Melosh, A. M. Vickery, and R. Greenberg 1996. Origin of the Spacewatch small Earth-approaching asteroids. *Icarus* **122**, 406-427.

Bottke, W. F., D. C. Richardson and S. G. Love 1998. Production of Tunguska-sized bodies by Earth's tidal forces. *Icarus* **134**, 47-76.

Bottke, W. F., A. Morbidelli, R. Jedicke, J. Petit, H. F. Levison, P. Michel and T. S. Metcalfe 2002a. Debiased orbital and absolute magnitude distribution of the near-Earth objects. *Icarus* **156**, 399-433.

Bottke, W. F., D. Vokrouhlický, D. P. Rubincam and M. Broz 2002b. The effect of Yarkovsky thermal forces on the dynamical evolution of asteroids and meteoroids. In *Asteroids III* (W. F. Bottke, A. Cellino, P. Paolicchi, and R. P. Binzel, Eds.), pp. 395-408. University of Arizona Press, Tucson.

Bottke W. F., D. Nesvorný, R. E. Grimm, A. Morbidelli and D. P. O'Brien 2006. Iron meteorites as remnants of planetesimals formed in the terrestrial planet region. *Nature* **439**, 821-824.

Bowell E., C. R. Chapman, J. C. Gradie, D. Morrison and B. Zellner 1978. Taxonomy of asteroids. *Icarus* **35**, 313–335.

Bowell, E., 1992. (4015) 1979 VA = Comet Wilson–Harrington (1949 III). *IAU Circ.* 5585.

Buie, M. W. 1984. Lightcurve CCD spectrophotometry of Pluto. Ph.D. dissertation, University of Arizona.

Bus, S. J. 1999. Compositional structure in the asteroid belt: Results of a spectroscopic survey. Ph.D. dissertation, Massachusetts Institute of Technology.

Bus, S. J., F. Vilas and M. A. Barucci 2002. Visible-wavelength spectroscopy of asteroids. In *Asteroids III* (W. F. Bottke, A. Cellino, P. Paolicchi, and R. P. Binzel, Eds.), pp. 169–182. University of Arizona Press, Tucson.

Bus, S. J. and R. P. Binzel 2002a. Phase II of the Small Main-Belt Asteroid Spectroscopic Survey: A feature-based taxonomy. *Icarus* **158**, 146-177.

Bus, S. J. and R. P. Binzel 2002b. Phase II of the Small Main-Belt Asteroid Spectroscopic Survey: The observations. *Icarus* **158**, 106-145.

Chapman C. R., D. Morrison, and B. Zellner 1975. Surface properties of asteroids: A synthesis of polarimetry, radiometry, and spectrophotometry. *Icarus* **25**, 104–130.

- Chapman, C. R. 2004. Space weathering of asteroid surfaces. *Annu. Rev. Earth Planet. Sci.* **32**, 539-567.
- Clark, B. E., B. Hapke, C. Pieters and D. Britt 2002. Asteroid space weathering and regolith evolution. In *Asteroids III* (W. F. Bottke, A. Cellino, P. Paolicchi, and R. P. Binzel, Eds.), pp. 585-599. University of Arizona Press, Tucson.
- Cloutis, E. A., M. J. Gaffey, D. G. W. Smith, and R. St. J. Lambert 1990. Reflectance spectra of “featureless” materials and the surface mineralogies of M- and E-class asteroids. *J. Geophys. Res.* **95**, 281-293.
- Cunningham, L. E. 1950. Periodic Comet Wilson–Harrington (1949g). *IAU Circ.* 1250.
- Danby, J. M. A. 1988. *Fundamentals of Celestial Mechanics*, 2nd ed. Wilmann-Bell, Inc. Richmond, VA.
- Dandy, C. L., A. Fitzsimmons, and S. J. Collander-Brown 2003. Optical colors of 56 near-Earth objects: trends with size and orbit. *Icarus* **163**, 363-373.
- Fernández, J. A. and W. H. Ip 1991. Statistical and evolutionary aspects of cometary orbits. In *Comets in the Post-Halley Era* (R. L. Newburn, Jr., M. Neugebauer, and J. Rahe, Eds.), pp. 487-535. Kluwer Academic Publishers, Boston.
- Fevig, R. A., and U. Fink 2001. Compositional trends within the NEA population: Results from a spectroscopic survey of 54 objects. American Astronomical Society, DPS meeting #33.
- Fevig, R. A., and U. Fink 2003. Orbit and size dependent taxonomic trends within the NEA population. American Astronomical Society, DPS meeting #35.
- Fevig, R. A., and U. Fink 2006. Spectral observations of 19 weathered and 23 fresh NEAs and their correlations with orbital parameters. (accepted for publication in *Icarus*)
- Fink, U., B. A. Smith, D. C. Benner, J. R. Johnson, H. J. Reitsema and J. A. Westphal 1980. Detection of a CH₄ atmosphere on Pluto. *Icarus* **44**, 62-71.
- Fink, U., and M. A. DiSanti 1990. The production rate and spatial distribution of H₂O for comet P/Halley. *Astrophys. J.* **364**, 687-698.
- Fink, U., and M. D. Hicks 1996. A survey of 39 comets using CCD spectroscopy. *Astrophys. J.* **459**, 729-743.
- Fink, U., M. Hicks, J. Collins and W. Grundy 1996. Spectra of Near Earth Asteroids. American Astronomical Society, DPS meeting #28.

- Fink, U., M. D. Hicks, R. A. Fevig and J. Collins 1998. Spectroscopy of 46P/Wirtanen during its 1997 apparition. *Astron. and Astrophys.* **335**, L37-L45.
- Fink, U., M. D. Hicks and R. A. Fevig 1999. Production rates for the *Stardust* mission target: 81P/Wild 2. *Icarus* **141**, 331-340.
- Gaffey, M. J. 1976. Spectral reflectance characteristics of the meteorite classes. *J. Geophys. Res.* **81**, 905-920.
- Gaffey, M. J., J. F. Bell and D. P. Cruikshank 1989. Reflectance spectroscopy and asteroid surface mineralogy. In *Asteroids II* (R. P. Binzel, T. Gehrels, and M. S. Matthews, Eds.), pp. 98-127. University of Arizona Press, Tucson.
- Gaffey, M. J., K. L. Reed and M. S. Kelley 1992. Relationship of E-type Apollo asteroid 3103 (1982 BB) to the enstatite achondrite meteorites and the Hungaria asteroids. *Icarus* **100**, 95-109.
- Gaffey, M. J., J. F. Bell, R. H. Brown, T. H. Burbine, J. L. Piatek, K. L. Reed and D. A. Chaky 1993a. Mineralogical variations within the S-type asteroid class. *Icarus* **106**, 573-602.
- Gaffey, M. J., T. H. Burbine and R. P. Binzel 1993b. Asteroid spectroscopy - Progress and perspectives. *Meteoritics* **28**, 161-187.
- Gladman, B. J., F. Migliorini, A. Morbidelli, V. Zappala, P. Michel, A. Cellino, C. Froeschle, H. F. Levison, M. Bailey and M. Duncan 1997. Dynamical lifetimes of objects injected into asteroid belt resonances. *Science* **277**, 197-201.
- Gradie, J. C., C. R. Chapman and E. F. Tedesco 1989. Distribution of taxonomic classes and the compositional structure of the asteroid belt. In *Asteroids II* (R. P. Binzel, T. Gehrels, and M. S. Matthews, Eds.), pp. 316-335. University of Arizona Press, Tucson.
- Hammergren, M. 1999. The composition of Near-Earth Objects. Ph.D. dissertation, University of Washington.
- Hapke, B. 2001. Space weathering from Mercury to the asteroid belt. *J. Geophys. Res.* **106**, pp. 10039-10073.
- Harris, A. W. and J. S. V. Lagerros 2002. Asteroids in the thermal infrared. In *Asteroids III* (W. F. Bottke, A. Cellino, P. Paolicchi, and R. P. Binzel, Eds.), pp. 205-218. University of Arizona Press, Tucson.
- Helin, E. F. 1979. 1979 VA. *IAU Circ.* 3422.

- Hicks, M., W. Grundy, U. Fink, S. Mottola and G. Neukum 1995. Rotationally resolved spectra of 1620 Geographos. *Icarus* **113**, 456-459.
- Hicks, M. D., U. Fink and W. M. Grundy 1998. The unusual spectra of 15 near-Earth asteroids and extinct comet candidates. *Icarus* **133**, 69-78.
- Howell, E. S. 1995. Probing Asteroid Composition using Visible and Near-Infrared Spectroscopy. Ph.D. dissertation, University of Arizona.
- Keil, K. 1989. Enstatite meteorites and their parent bodies. *Meteoritics* **24**, 195-208.
- Kresák, L. 1979. Dynamical interrelations among comets and asteroids. In *Asteroids* (T. Gehrels, Ed.), pp. 289–309. Univ. of Arizona Press, Tucson.
- Larson, H. P. and U. Fink 1975. Infrared spectral observations of asteroid 4 Vesta. *Icarus* **26**, 420-427.
- Levison, H. F. and M. J. Duncan 1994. The long-term dynamical behavior of short-period comets. *Icarus* **108**, 18-36.
- Lipschutz, M. E., M. J. Gaffey and P. Pellas 1989. Meteoritic parent bodies: nature, number, size and relation to present-day asteroids. In *Asteroids II* (R. P. Binzel, T. Gehrels, and M. S. Matthews, Eds.), pp. 740-777. University of Arizona Press, Tucson.
- Luu, J. X. 1993. Spectral diversity among the nuclei of comets. *Icarus* **104**, 138-148.
- Marsden, B. G. 1992. (4015) 1979VA = Comet Wilson–Harrington (1949 III). *IAU Circ.* 5585.
- Marsden, B. G. 2005. Sungrazing comets. *Annu. Rev. Astron. Astrophys.* **43**, 75–102.
- Marti, K. and T. Graf 1992. Cosmic-ray exposure history of ordinary chondrites. *Annu. Rev. Earth Planet. Sci.* **20**, 221-243.
- McCord, T. B., J. B. Adams and T. V. Johnson 1970. Asteroid Vesta: Spectral reflectivity and compositional implications. *Science* **168**, 1445-1447.
- McFadden, L. A., M. J. Gaffey, and T. B. McCord 1985. Near-Earth asteroids: possible sources from reflectance spectroscopy. *Science* **229**, 160-163.
- McFadden, L., D. J. Tholen and G. J. Veeder 1989. Physical properties of Aten, Apollo and Amor asteroids. In *Asteroids II* (R. P. Binzel, T. Gehrels, and M. S. Matthews, Eds.), pp. 442-467. University of Arizona Press, Tucson.

Morbidelli, A., R. Jedicke, W. F. Bottke, P. Michel and E. F. Tedesco 2002. From magnitudes to diameters: The albedo distribution of near Earth objects and the Earth collision hazard. *Icarus* **158**, 329-342.

Morbidelli, A., W. F. Bottke, C. Froeschle and P. Michel 2002. Origin and evolution of Near-Earth Objects. In *Asteroids III* (W. F. Bottke, A. Cellino, P. Paolicchi, and R. P. Binzel, Eds.), pp. 409-422. University of Arizona Press, Tucson.

Nesvorny, D., R. Jedicke, R. J. Whiteley and Z. Ivezić 2005. Evidence for asteroid space weathering from the Sloan Digital Sky Survey. *Icarus* **173**, 132-152.

Pasek M. A. 2006. Phosphorus and sulfur cosmochemistry: implications for the origins of life. Ph.D. dissertation, University of Arizona.

Press, W. H., S. A. Teukolsky, W. T. Vetterling, and B. P. Flannery 2001. *Numerical Recipes in Fortran. The Art of Scientific Computing*. Cambridge University Press. Cambridge, UK.

Rabinowitz, D. L. 1998. Size and orbit dependent trends in the reflectance colors of Earth-approaching asteroids. *Icarus* **134**, 342-346.

Richardson, D. C., W. F. Bottke and S. G. Love 1998. Tidal distortion and disruption of Earth-crossing asteroids. *Icarus* **134**, 47-76.

Roach, F. E. and L. G. Stoddard 1938. A Photoelectric Light-Curve of Eros. *Astrophys. J.* **88**, 305-312.

Schuster, W. J. 1976. 13-color photometry of solar-type stars. *Rev. Mex. Astron. Astrofis.* **1**, 327-342.

Sears, D. W. G. and R. T. Dodd 1988. Overview and classification of meteorites. In *Meteorites and the Early Solar System* (J. F. Kerridge and M. S. Matthews, Eds.), pp. 3-31. University of Arizona Press, Tucson.

Soderblom, L. A., T. L. Becker, G. Bennett, D. C. Boice, D. T. Britt, R. H. Brown, B. J. Buratti, C. Isbell, B. Giese, T. Hare, M. D. Hicks, E. Howington-Kraus, R. L. Kirk, M. Lee, R. M. Nelson, J. Oberst, T. C. Owen, M. D. Rayman, B. R. Sandel, S. A. Stern, N. Thomas and R. V. Yelle 2002. Observations of Comet 19P/Borrelly by the Miniature Integrated Camera and Spectrometer Aboard Deep Space 1. *Science* **296**, 1087-1091.

Tholen, D. J. 1984. Asteroid taxonomy from cluster analysis of photometry. Ph.D. dissertation, University of Arizona.

- Tholen, D. J. and M. A. Barucci 1989. Asteroid taxonomy. In *Asteroids II* (R. P. Binzel, T. Gehrels, and M. S. Matthews, Eds.), pp. 298-315. University of Arizona Press, Tucson.
- Veeder G. J., E. F. Tedesco and D. L. Matson 1989. Asteroid results from the IRAS survey. In *Asteroids II* (R. P. Binzel, T. Gehrels, and M. S. Matthews, Eds.), pp. 282–289. Univ. of Arizona, Tucson.
- Vilas, F., and B. A. Smith 1985. Reflectance spectrophotometry ($\sim 0.5\text{-}1.0\ \mu\text{m}$) of outer-belt asteroids: implications for primitive, organic solar system material. *Icarus* **64**, 503-516.
- Watson, F. 1937. The Physical Nature of Eros. *Harvard Coll. Obs. Circ.* **419**, 1-14.
- Weissman, P. R., M. F. A'Hearn, L. A. McFadden and H. Rickman 1989. Evolution of comets into asteroids. In *Asteroids II* (R. P. Binzel, T. Gehrels, and M. S. Matthews, Eds.), pp. 880-920. University of Arizona Press, Tucson.
- Whiteley, R. J. 2001. A compositional and dynamical survey of the near-Earth asteroids. Ph.D. dissertation, University of Hawaii.
- Xu, S., R. P. Binzel, T. H. Burbine and S. J. Bus 1995. Small Main-Belt Asteroid Spectroscopic Survey: Initial Results. *Icarus* **115**, 1-35.